People's Democratic Republic of Algeria

Ministry of Higher Education and Scientific Research

SAAD DAHLEB University « Blida-1 »

Faculty of Sciences, Department of Physics
Specialty: Materials Physics

Doctoral Thesis in Physics
Submitted by:

ZERMANE Wafia

Development of Luminescent Materials Based on Zinc Oxide (ZnO) Doped with Rare-Earth Ions in the Form of Nanometric Powders and Thin Films

Board of Examiners:

Mr. Khelifi Rachid	Professor, Saad Dahleb University, Blida 1	President
Mr. Derbal Mourad,	Professor, Saad Dahleb University, Blida 1	Examiner
Mr. Mahroug Abdelhafid	Professor University, MB M'sila 1	Examiner
Mr. Hadjersi Toufik	Rech. Dir, CRTSE	Examiner
Mr. guerbous lakhdar	Rech. Dir, Nuclear Research Centre of Algiers	Supervisor
Mrs. Bekhti Widad	MCB Saad Dahleb University, Blida 1	Co-supervisor

Blida, November 2025

Dedication

Wholeheartedly, this thesis is dedicated to :

My irreplaceably precious late mother, languages fail drastically to describe what you mean to me …

In memory of my beloved father,who left us many years ago

My dear sisters, for their robust support …

My esteemed friends …

All my teachers …

Acknowledgements

First and foremost, I would like to express my profound gratitude to God, who granted me the strength, patience, and determination to accomplish this modest work.

I wish to sincerely thank Professor Lakhdar Guerbous and Mrs. Widad Bekhti, who guided and supervised me throughout the preparation of this doctoral thesis. Their generosity with their time, their valuable expertise, their encouragement, and above all, the trust they placed in me, were essential to the completion of this research.

This PhD thesis was conducted as a collaborative effort between the Department of Physics, University of Blida 1, and the Algiers Nuclear Research Center. I am deeply grateful to these institutions for providing me with the opportunity and resources to pursue this research.

I wish to express my profound gratitude to the distinguished members of the jury, Prof. Khelifi Rachid (President, Saad Dahleb University, Blida 1), Prof. Derbal Mourad (Examiner, Saad Dahleb University, Blida 1), Prof. Mahroug Abdelhafid (Examiner, MB University, M'sila 1), and Dr. Hadjersi Toufik (Examiner, Research Director, CRTSE), for their rigorous evaluation of this work and for their insightful comments and constructive criticism, which have significantly contributed to its refinement and overall improvement

Special thanks are extended to Dr. Larbah Youssef for his unconditional help, support, and pieces of advice whenever we needed him.My gratitude also goes to all the members of the Nuclear Research Centre in Algiers, especially Dr. Allaoua Boukerika and Dr RAHAL Badis, as well as to all those not mentioned here, many indeed whose presence and support gave me the determination to see this work through to the end.

I also warmly thank all those who, near or far, contributed to this achievement and provided their assistance and support my colleagues and my friends. Finally, I dedicate my heartfelt thanks to my family for their constant support and for sharing in the success of this work.

Thank you so much everyone!

Abstract

In this work, nanocrystalline ZnO: Eu^{3+} powders and thin films co doped with Li^{+} were successfully synthesized by the sol gel method. Co doping with Li^{+} was found to significantly influence the structural, morphological, and luminescent properties of ZnO: Eu^{3+} materials. X ray diffraction (XRD) and Raman spectroscopy confirmed the formation of a wurtzite hexagonal structure with crystallite sizes ranging between 27 and 31 nm. Morphological analysis by FE-SEM revealed that the introduction of Li^{+} and Eu^{3+} modifies the particle and grain shapes, evolving from quasi spherical, randomly packed morphologies to more block like structures. Photoluminescence (PL) studies demonstrated strong red emission arising from the $^{5}D_{0} \rightarrow {}^{7}F_{j}$ (J = 0–4) intra 4f transitions of Eu^{3+} ions under both charge transfer ($O^{2-} \rightarrow Eu^{3+}$) and $^{5}D_{2}$ excitations. The emission intensity was found to depend on the excitation wavelength, with an optimum at 7% Li^{+} under 465 nm excitation and at 10% under 258 nm excitation. In particular, under 258 nm excitation, Li^{+} concentrations of 5 and 10% enhanced red emission due to more efficient energy transfer from ZnO defect centres to Eu^{3+} ions, as further confirmed by the variation of the $^{5}D_{0}$ lifetime with Li content. Local field effect analysis indicated that 5 % Li^{+} yields the highest bulk radiative lifetime values (τ_B = 3.004 ms for the real cavity model and τ_B = 6.042 ms for the virtual cavity model). Finally, the combined structural and optical results demonstrate that Li^{+} co doped ZnO: Eu^{3+} powders and thin films are promising candidates for optoelectronic applications, particularly in display and lighting technologies.

الملخص

في هذا العمل، تم تحضير مساحيق وأغشية رقيقة نانوية من أكسيد الزنك المطعَّم بأيونات اليوروبيوم الثلاثية $ZnO:Eu^{3+}$ والمشترَك تطعيمه بأيونات الليثيوم Li^{+} بنجاح باستخدام طريقة المحلول–الهلام (السول–جل). وقد أظهرت النتائج أن التطعيم المشترك بأيونات الليثيوم يؤثر بصورة ملحوظة في الخصائص البنيوية، والشكلية، والخواص التألقية الضوئية لمواد $ZnO:Eu^{3+}$.

وأكّد كلٌّ من تحليل حيود الأشعة السينية والتحليل الطيفي للاهتزازات الشبكية (رامان) تكوّن بنية سداسية من نوع وورتزيت، مع أحجام بلورات تراوحت بين 27 و31 نانومتر.

وأظهرت دراسة الخصائص الشكلية باستخدام المجهر الإلكتروني الماسح عالي الدقة أن إدخال أيونات الليثيوم واليوروبيوم يؤدي إلى تغيّر في أشكال الجسيمات والحبيبات من بُنى شبه كروية وعشوائية الترتيب إلى بُنى أكثر تكتلًا وانتظامًا.

كما كشفت دراسات التألق الضوئي عن انبعاث أحمر قوي ناتج عن الانتقالات الإلكترونية داخلية المنشأ لأيونات اليوروبيوم الثلاثية من $^5D_0 \rightarrow {}^7F_j$ حيث$(J = 0–4)$، وذلك تحت كلٍّ من إثارة انتقال الشحنة من أيونات الأكسجين إلى أيونات اليوروبيوم، وإثارة المستوى الطاقي $^5D_2$.

وتبيّن أن شدة الانبعاث تعتمد على طول موجة الإثارة، إذ بلغت قيمتها العظمى عند تركيز 7% من الليثيوم تحت إثارة بطول موجي قدره 465 نانومتر، وعند تركيز 10% تحت إثارة بطول موجي قدره 258 نانومتر. وبوجه خاص، عند الإثارة بطول موجي 258 نانومتر، أدّت تراكيز الليثيوم الواقعة بين 5% و10% إلى تعزيز الانبعاث الأحمر، نتيجة زيادة كفاءة نقل الطاقة من مراكز العيوب في أكسيد الزنك إلى أيونات اليوروبيوم، وهو ما أكدته أيضًا التغيرات الملحوظة في عمر الحالة المثار $^5D_0$ مع تغير محتوى الليثيوم.

كما أظهر تحليل تأثير المجال المحلي أن تركيز 5% من الليثيوم أعطى أعلى قيم لعمر الإشعاع الحجمي، حيث بلغ 3.004 ملّي ثانية وفق نموذج التجويف الحقيقي، و6.042 ملّي ثانية وفق نموذج التجويف الافتراضي .وأخيرًا، تُبيّن النتائج البنيوية والضوئية المتكاملة أن مساحيق وأغشية أكسيد الزنك المطعَّمة باليوروبيوم والمشترَك تطعيمها بالليثيوم تُعد مرشحة واعدة لتطبيقات الأجهزة البصرية الإلكترونية، ولا سيما في تقنيات العرض والإضاءة.

Contents

Chapitre I

Chapitre II

Chapitre III

Chapitre IV

GENERAL INTRODUCTION

GENERAL INTRODUCTION

Light has always fascinated humanity and played a central role across world cultures. For this reason, luminescent materials have attracted increasing scientific interest due to their numerous potential applications in various fields such as medical imaging, optoelectronics, sensing, lighting, and display technologies. Current research in this domain is no longer solely focused on discovering the “ideal luminescent material,” but rather on identifying the specific properties best suited for targeted applications.

In this work, our research focuses on materials for photodetectors, particularly transparent conductive oxides (TCOs)[1] [2], doped with specific rare earth (RE) ions [3] [4]. These materials can absorb energy either through the host matrix or via the dopant ions, with energy transfer processes facilitating excitation. In most cases, luminescence emission originates from these deliberately introduced dopants—such as RE ions—present at relatively low concentrations. TCOs are materials that are transparent in the visible range and exhibit relatively low resistivities (~10^{-4} Ω·cm) [5] [6], making them particularly well-suited for optoelectronic applications such as electroluminescence [7].Among the various TCOs, zinc oxide (ZnO) doped with rare earth ions has attracted significant attention in the scientific community, as reflected by numerous publications and conferences dedicated to the topic. ZnO is an environmentally friendly, biocompatible semiconductor material[8],posing minimal risk to human health. It exhibits a direct band gap of approximately 3.37 eV at room temperature [9], making it highly promising for a wide range of electronic and optoelectronic applications. Furthermore, ZnO can be easily synthesized by various methods, including sol-gel [10], hydrothermal [11] , and chemical vapour deposition (CVD) [12], allowing flexibility in tailoring its properties for specific applications.

The objective of this thesis is to enhance the luminescent properties of ZnO through co-doping with a rare earth ion (Europium) and an alkali metal (Lithium). Europium

(Eu^{3+}) is considered one of the most effective activator ions for luminescent materials due to its well-defined electronic transitions within the 4f orbital shell and long excited-state lifetimes, which together result in intense red emission centred around 615 nm ($^5D_0 \rightarrow {}^7F_2$) [4]. These intra-4f transitions are parity-forbidden but become partially allowed when Eu^{3+} is incorporated into a non-centrosymmetric crystal field, such as the wurtzite structure of ZnO [13]. In this host matrix, ZnO's wide band gap (~3.37 eV) enables efficient absorption of ultraviolet (UV) radiation, which can then be non-radiatively transferred to the Eu^{3+} ions due to favourable energy level alignment. This energy transfer mechanism enhances visible light emission, particularly in the red spectral region, thereby significantly improving the photoluminescent response [14]. This enhancement is especially valuable for the development of ZnO-based powders and thin films for use as luminescent materials in photonic devices, light-emitting diodes, and bioimaging applications [15].

In parallel, lithium (Li^+) doping contributes to improved structural stability by stabilizing the wurtzite phase, reducing lattice strain and defects, and enhancing crystallinity. These changes improve charge carrier dynamics and the electrical conductivity of ZnO [16]. Thus, co-doping ZnO with Eu^{3+} and Li^+ significantly enhances its electrical, optical, and luminescent properties, making it a promising material for optoelectronic and sensing applications.

This thesis also investigates and compares the structural, morphological, optical, and spectroscopic properties of nanomaterials synthesized in both powder and thin-film forms. Thin films are deposited on glass substrates using the sol-gel dip-coating method at room temperature.

A wide range of characterization techniques is employed, including X-ray diffraction (XRD), Raman spectroscopy, scanning electron microscopy (SEM), UV-Visible

spectroscopy, and photoluminescence (PL) at room temperature. Based on this context, this thesis aims to answer the following research question: How does co-doping zinc oxide (ZnO) with europium (Eu^{3+}) and lithium (Li^{+}) influence its structural, optical, and luminescent properties.

The answer to this research question lies in the main objective of this thesis, which is to elaborate and characterize luminescent materials based on zinc oxide (ZnO) co-doped with europium (Eu^{3+}) and lithium (Li^{+}), in both powder and thin-film forms, to enhance their optical performance for potential use in optoelectronic applications.

The specific objectives are:

1. To synthesize ZnO-based materials doped with Eu^{3+} and co-doped with Eu^{3+}/Li^{+}, using the sol-gel method for powders and the dip-coating method for thin films.
2. To investigate the effect of Li^{+} concentration on the structural, optical, and luminescent properties of Eu^{3+}-doped ZnO nanoparticules
3. To compare the structural, morphological, and photoluminescent behavior of the materials in powder form, in order to understand how co-doping and morphology influence their performance.
4. To optimize key synthesis parameters, including dopant concentration, annealing temperature, and number of deposited layers, in order to enhance the crystallinity and emission efficiency of ZnO thin films co-doped with Eu^{3+} and Li^{+}.
5. To assess the suitability of these materials for use in photonic devices, based on their luminescence response and material stability.

This thesis is organized into four chapters:

Chapter 1 (General Overview of ZnO and Rare Earth Doping)

This chapter introduces the fundamental properties of zinc oxide (ZnO), its crystal structure, optical characteristics, and intrinsic defects. It also discusses the role of rare

earth elements-especially europium (Eu^{3+})-as luminescent activators, and the co-doping effect of lithium (Li^{+}) on structural and optical modifications. The rationale for using these dopants in both powder and thin-film forms is also presented, along with relevant applications in photonics and sensor technology.

Chapter 2 (Materials and Methods)

This chapter presents the synthesis approaches used to prepare ZnO:Eu and ZnO:Eu,Li materials, including the sol-gel method for powders and the dip-coating technique for thin films. It also details the experimental conditions, processing parameters, and characterization techniques (XRD, SEM, Raman spectroscopy, UV-Vis, and photoluminescence) employed to analyze structural, morphological, and optical properties.

Chapter 3 (Structural and Optical Characterization of ZnO:2%Eu, x% Li Powders)

In this chapter, the effects of Li^{+} concentration on the structure, morphology, and luminescence of ZnO: Eu^{3+} powders are systematically investigated. Crystallinity, grain size, and emission intensity are analyzed to determine optimal doping conditions.

Chapter 4 (Characterization of ZnO:Eu,Li Thin Films**)**

This chapter focuses on the study of thin films deposited on glass substrates via the dip-coating method. It examines the influence of various parameters such as the number of layers, annealing temperature, and dopant levels on the films' structural and photoluminescent performance.

This thesis concludes with a general summary that highlights the key findings and contributions of the work.

CHAPTER I

Fundamentals and Applications of ZnO, ZnO doped and co-doped with Eu and Li.

I.1. Introduction

Zinc oxide (ZnO) has emerged as a multifunctional material with broad interest in the fields of optoelectronics, sensing, and luminescence. Its wide direct band gap, high exciton binding energy, and versatile nanostructuring capability make it a promising candidate for numerous applications. This chapter presents a comprehensive overview of ZnO and its modification through doping with rare-earth ions (Eu^{3+}) and alkali (Li^{+}), both separately and in combination. Particular attention is given to how these dopants affect the structural, optical, and luminescent properties of ZnO in both powder and thin-film forms and their potential applications in various fields.

I.2. Zinc Oxide (ZnO): Fundamentals

I.2.1. Crystal Structures of ZnO

Zinc oxide, also known as zincite in its natural mineral form, often contains trace elements such as manganese (Mn), which can influence its colour. Naturally occurring zincite typically appears yellow to red due to these impurities. However, ZnO used in scientific research and technological applications is synthetically produced and appears as a pure white powder, free from such colour-causing dopants [1].

Zinc oxide crystallises in three main structures: cubic rocksalt, cubic zinc blended and hexagonal wurtzite, depending on synthesis conditions such as temperature and pressure. The wurtzite structure is the most stable under ambient conditions and is therefore the most commonly studied form in material science and optoelectronics [2].

- **Rocksalt (Cubic):** This structure (Figure 1) is metastable and forms under high pressure above 10 GPa [3], belonging to the Fm-3m space group. It features octahedral coordination, where both Zn^{2+} and O^{2-} ions are surrounded by six nearest neighbours. However, it lacks piezoelectric and spontaneous polarisation properties, making it unsuitable for certain optoelectronic and piezoelectric applications. Nevertheless, its high density and modified electronic structure may be of interest in high-pressure physics and studies on material stability [4].

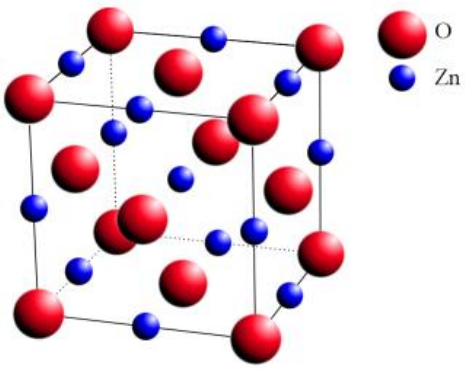

Figure I.1: Rocksalt structure of ZnO

- **Zinc Blende (Cubic):** The zinc blende structure of ZnO (Figure 2) is a metastable cubic phase that belongs to the F-43m space group and features a face-centred cubic (FCC) lattice [5]. This form is difficult to stabilise and typically appears only under specific conditions, such as epitaxial growth on cubic substrates, high-pressure synthesis, or the incorporation of certain impurities. Owing to its structural similarity with the wurtzite phase, the blende structure exhibits comparable physical properties; however, it lacks spontaneous polarisation and is rarely observed in bulk ZnO.

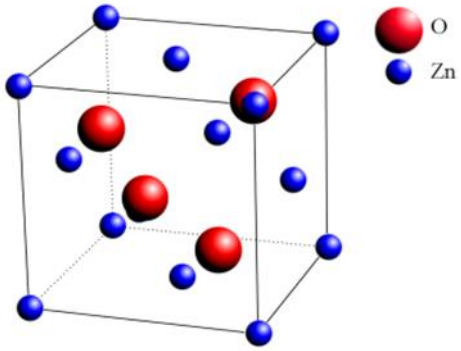

Figure I.2: Blende structure of ZnO

- **Wurtzite (Hexagonal):** Finally, the wurtzite structure (Figure 3) . This structure is the most thermodynamically stable under ambient conditions of room temperature and pressure, and it is the form of greatest interest in this study. This stability contributes significantly to ZnO's unique physical and

chemical properties. The wurtzite structure belongs to the hexagonal[1] space group $P6_3mc$ and is characterised by tetrahedral coordination between Zn^{2+} and O^{2-} ions. The typical lattice constants are a = 3.25 Å and c = 5.2 Å, yielding a c/a ratio close to the ideal value of 1.633 [6].

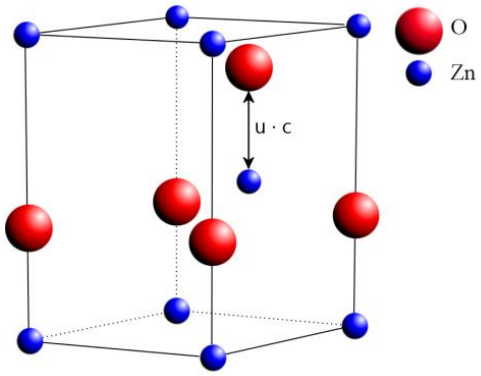

Figure I.3: wurtzite structure of ZnO

I.2.2. Electronic and Optical Properties

Zinc oxide (ZnO) is a II–VI binary semiconductor composed of zinc (Zn^{2+}) and oxygen (O^{2-}) ions arranged in a crystalline lattice. It exhibits a direct wide band gap of approximately 3.37 eV at room temperature [7], which is one of the key characteristics that distinguish ZnO from many other semiconductors. ZnO possesses a high exciton binding energy of about 60 meV [8], enabling stable excitonic emission even at ambient conditions, making it suitable for UV-emitting devices.

- **Band Structure:** The electronic band structure of ZnO originates from the atomic configurations of zinc and oxygen. Zinc has the electronic configuration **[Ar] $3d^{10}$ $4s^2$**, while oxygen is configured as **[He] $2s^2$ $2p^4$**. In ZnO, the 2p states of oxygen mainly constitute the valence band, and the 4s states of zinc form the conduction band. This configuration results in a direct band gap located at the Γ point of the Brillouin zone, which is essential for

[1] The structural arrangement in ZnO significantly influences its physical properties, including band gap, piezoelectric behaviour, and defect chemistry.

understanding ZnO's electro-optical behaviour. (Figure.4) [9] illustrates the calculated band structure[2] of wurtzite ZnO, obtained using density functional theory (DFT) with the generalised gradient approximation plus Hubbard U correction (GGA+U).

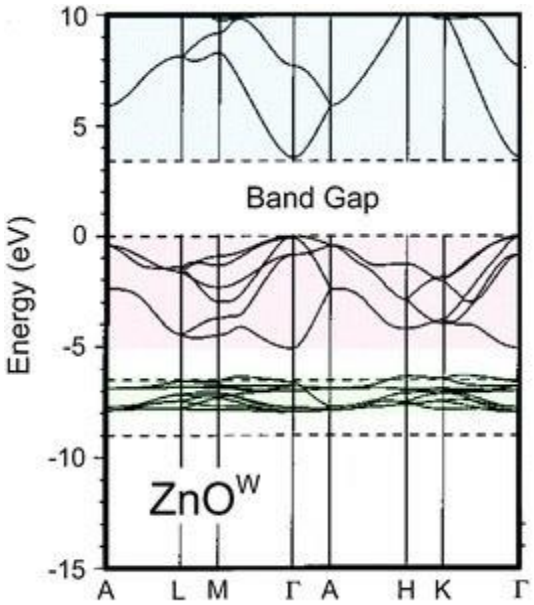

Figure I.4 : (GGA+U) Band structure of wurtzite ZnO) [10]

- **Intrinsic Defects:** Theoretically, stoichiometric ZnO should behave as an insulating material. However, in practice, it exhibits semiconducting properties because of intrinsic defects [11] such as oxygen vacancies (V_O), zinc interstitials (Zn_i), zinc vacancies (V_{Zn}), and oxygen interstitials (O_i) [12]. These point defects introduce electronic states within the band gap and strongly influence the electrical and optical properties of ZnO, particularly its photoluminescence (PL) behaviour. The ultraviolet emission, often referred to as near band edge (NBE) emission, arises from the recombination of free excitons or shallowly bound electron-hole pairs. In contrast, the visible emission, known as deep-level emission (DLE), is associated with defect states primarily related to oxygen vacancies and zinc interstitials and typically appears as green or yellow luminescence.

[2] The zero reference corresponds to the energy maximum of the valence band, which is precisely at point Γ

- **Electrical and Piezoelectric Properties:** ZnO is naturally n-type due to native defects such as zinc interstitials and oxygen vacancies. This unintentional doping results in relatively high electrical conductivity, typically in the range of 10^{-2} to 10^{0} S/cm for undoped ZnO films or bulk crystals [13]. In addition to its electrical behaviour, ZnO exhibits strong piezoelectric [14] and pyroelectric properties, which arise from its non-centrosymmetric wurtzite crystal structure and the resulting spontaneous polarisation along the c-axis. These piezoelectric characteristics enable ZnO to generate an electric potential in response to applied mechanical stress, making it a promising material for nanogenerators, pressure sensors, and actuators [15].

I.3.Doping of ZnO

I.3.1. General Principles of Doping in ZnO

The controlled introduction of dopants into ZnO is a widely applied strategy to adjust its electronic, optical, and structural characteristics for targeted technological applications [16][17]. It involves the deliberate incorporation of impurity atoms into the ZnO crystal lattice to alter its electronic structure, optical behaviour, and microstructural characteristics. In semiconductors, dopants can function as donors or acceptors, depending on their valence state relative to the host cation or anion [18]. ZnO is naturally n-type due to native defects; however, intentional doping can further enhance the free carrier concentration or introduce specific energy levels within the band gap. The effectiveness of doping is closely linked to the mechanism by which dopants are incorporated into the lattice, whether substitutionally, replacing a zinc or oxygen site or interstitially, occupying spaces between lattice sites [19]. Precise control over dopant type, concentration, and incorporation mode is therefore essential to achieve the desired functional properties.

There are several categories of dopants commonly used in ZnO, each selected to achieve specific functional modifications:

- **Group I elements (Li, Na, K):** These alkali metals have small ionic radii and can incorporate into the ZnO lattice either by substituting Zn^{2+} sites or by occupying interstitial positions [20]. When incorporated substitutionally, they

typically act as shallow acceptors, compensating the native n-type conductivity and potentially inducing p-type behaviour. Alternatively, interstitial incorporation also often results in donor characteristics which enhance n-type conductivity. Lithium, in particular [21], is widely studied for its dual role and its ability to improve crystallinity and reduce native defects.

- **Group III elements (Al, Ga, In):** These trivalent cations are well known as efficient n-type dopants [22]. They readily replace Zn^{2+} in the lattice, introducing an extra electron into the conduction band and enhancing n-type conductivity.
- **Transition metals (Mn, Co, Ni):** Incorporation of these elements into ZnO introduces partially filled d-orbitals [23], which create additional electronic states within the band gap. These localised states can significantly modify the material's optical absorption and emission properties, often enhancing or quenching specific luminescence bands. Beyond their impact on optical behaviour, transition metal dopants are commonly used to induce magnetic ordering in ZnO, enabling the development of dilute magnetic semiconductors (DMS).
- **Rare-earth ions (Eu, Tb, Er):** REs dopants are primarily employed to enhance luminescent properties of ZnO due to their sharp intra-4f electronic transitions, which produce characteristic emissions in the visible and near-infrared regions. For example, Eu^{3+} yields intense red emission around 615 nm, and Tb^{3+} provides green emission [24]. However, incorporating these ions is challenging owing to their large ionic radii and valence mismatch with Zn^{2+}[25], often requiring charge compensation mechanisms and careful control of synthesis conditions to ensure uniform distribution without phase segregation.

I.3.2. Integration of Rare-Earth Element (Eu^{3+}) into ZnO Lattice

Europium is chosen as a dopant for ZnO due to its unique combination of chemical stability. Eu^{3+} exhibits sharp and intense red emissions arising from intra (4f) electronic transitions, particularly the $5D_0 \rightarrow 7F_2$ transition near 610 nm. These emissions are characterised by narrow band widths and high colour purity. Furthermore, the trivalent oxidation state of europium is thermodynamically stable in the oxidising environments typically employed during ZnO synthesis, ensuring consistent incorporation and minimal risk of reduction to Eu^{2+}. The relatively large ionic

radius of Eu^{3+} compared to Zn^{2+} also introduces controlled lattice distortions, which can modulate defect concentrations and facilitate energy transfer processes from the ZnO host to the activator ions. Collectively, these attributes enable europium to enhance the optical performance of ZnO-based materials while maintaining good chemical and structural compatibility with the wurtzite lattice.

I.4. Fundamentals of Europium as a Dopant

Europium (symbol **Eu**, atomic number **63**) is a rare-earth element belonging to the lanthanide series of the periodic table. It was discovered in 1896 by the French chemist Eugène-Anatole Demarçay and named after the continent of Europe [26], and it is a soft, silvery metal. It tarnishes rapidly in air, forming an oxide layer. Among the lanthanides, europium has one of the lowest melting points and densities.

I.4.1.Basic Physicochemical Properties :

- Density : ~5.24 g/cm³
- Melting point: ~826 °C
- Boiling point: ~1529 °C
- Atomic weight: ~151.96 g/mol

I.4.2.Electronic Structure: The electronic configuration in the neutral state is :
[Xe] $4f^7$ $6s^2$

for its ability to exist in two oxidation states, Eu^{2+} and Eu^{3+}, each imparting distinct chemical and optical behaviours

Eu^{3+} (Trivalent): In the +3 oxidation state, the configuration is [Xe] $4f^6$, which yields red luminescence

Eu^{2+} (divalent) : In the +2 oxidation state, the configuration is [Xe] $4f^7$; yields blue luminescence

In ZnO and most oxide matrices, europium is predominantly trivalent (Eu^{3+}), because the synthesis atmosphere (oxygen-rich) stabilises this state. [27].

I.4.3. Optical Properties and Luminescence:

The luminescence of europium originates primarily from electronic transitions within the 4f shell. Because the 4f orbitals are shielded by the outer filled

5s and 5p subshells, they experience only weak perturbation from the crystal field of the host lattice. This shielding results in: Narrow and well-resolved emission lines, Emission wavelengths are largely independent of the chemical environment and High colour purity.

As we mentioned before, Europium can exist in both +2 and +3 oxidation states, each associated with distinct luminescent behaviour.

- **Luminescence of Trivalent Europium (Eu^{3+})**: The luminescence arises

mainly from transitions between the excited $5D_0$ level and the lower $7F_J$ manifold (where J = 0, 1, 2, 3, 4)

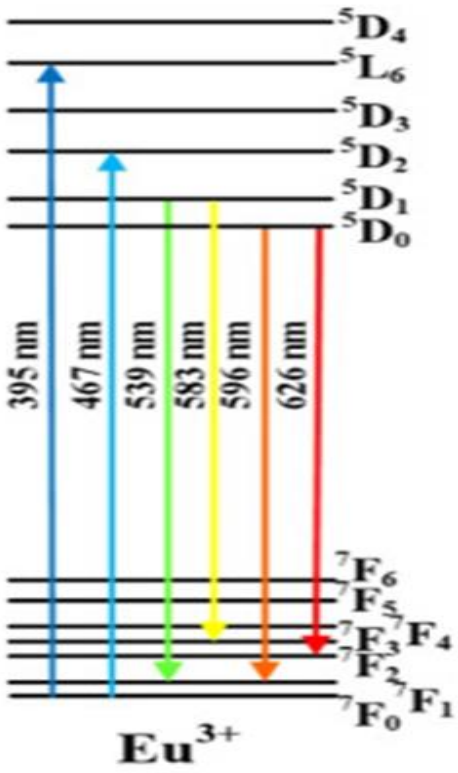

Figure I.5: Energy diagram of Eu^{3+} and main excitation and emission transitions

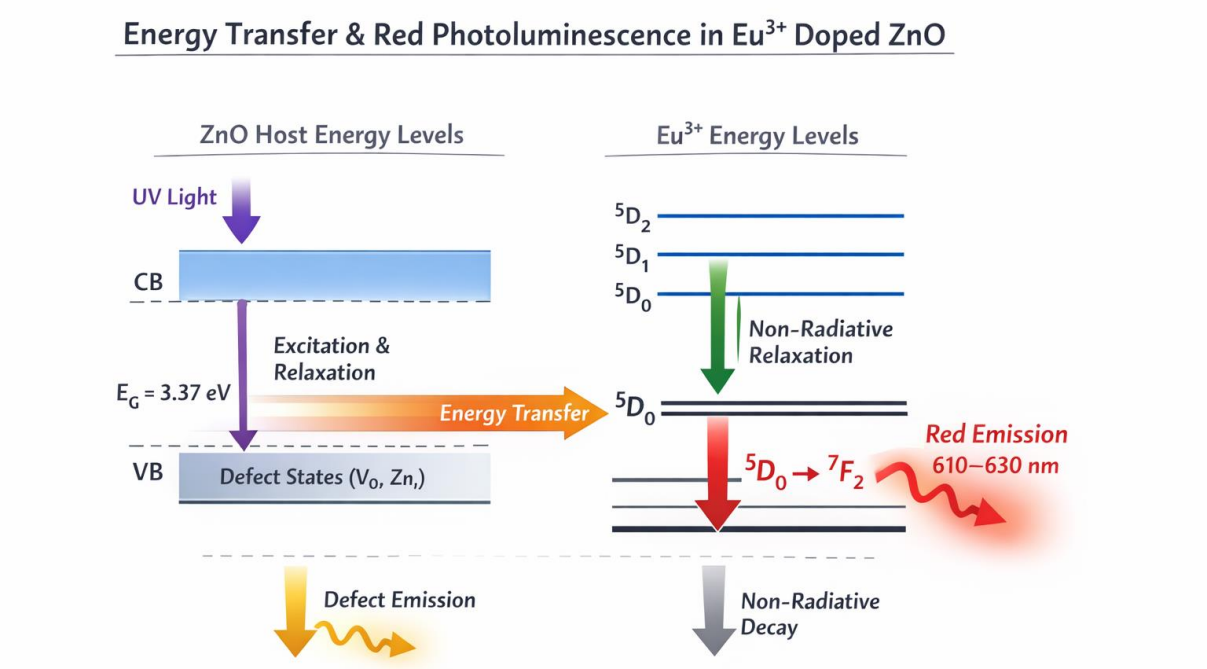

Figure I.6 : Schematic Representations of Energy Transfer Mechanisms and Red Photoluminescence in Eu^{3+} Doped ZnO

a. **Emission Transitions:** The most important transitions include:

- **$5D_0 \rightarrow 7F_0$ (~ 580 nm):** very weak, parity forbidden.
- **$5D_0 \rightarrow 7F_1$ (~ 590 nm):** Magnetic dipole transition, relatively insensitive to site symmetry.
- **$5D_0 \rightarrow 7F_2$ (~ 612 nm):** Electric dipole transition, Hypersensitive to site symmetry.
- **$5D_0 \rightarrow 7F_3$ (~ 650 nm):** Less intense.
- **$5D_0 \rightarrow 7F_4$ (~ 700 nm):** Weak.

Among these, the $5D_0 \rightarrow 7F_2$ transition dominates the emission spectrum, producing the intense red luminescence characteristic of Eu^{3+} activated. Because this transition is electric dipole in nature and hypersensitive, its intensity depends strongly on the local environment (site asymmetry) [28].

b. **Site Symmetry and Intensity Ratios:** The relative intensity of

Eu^{3+}emission lines are strongly influenced by the symmetry of the site occupied by the ion. In highly symmetric, inversion-symmetric environments, electric dipole transitions

are suppressed, and the emission is dominated by the magnetic dipole $^5D_0 \rightarrow {}^7F_1$ transition, which is only weakly sensitive to the local crystal field and remains relatively constant across different hosts. [29] In contrast, the $^5D_0 \rightarrow {}^7F_2$ transition, which is an electric dipole transition, is strictly forbidden in perfectly centrosymmetric sites but becomes much more intense when the Eu^{3+} ion occupies an asymmetric environment. This hypersensitive behaviour makes the intensity ratio between these transitions a valuable probe of local lattice distortion. The intensity ratio R is often defined as:

$$R = \frac{I(5D_0 \rightarrow 7F_2)}{I(5D_0 \rightarrow 7F_1)} \quad \text{..... I.1}$$

Where « I » denotes the integrated emission intensity of each transition. A high « R » value indicates a strongly asymmetric site, while a low value suggests a nearly centrosymmetric coordination around Eu^{3+}.

A « high R » value indicates a highly asymmetric site, while a « low R » value suggests that the Eu^{3+} ion occupies a nearly symmetric or centrosymmetric environment. This ratio serves as a spectroscopic probe of local structure, allowing researchers to:

- Identify lattice distortions.
- Monitor phase transitions in the host material.
- Evaluate the quality of the dopant incorporation.
- Study the effects of co-dopants or defects.*

c. **Excitation Mechanisms:** The luminescence of Eu^{3+} ions incorporated into ZnO arises through several distinct excitation pathways. In these processes, energy absorbed by the ZnO host is efficiently transferred to the europium ions, which then emit their characteristic red light. The main excitation processes are described below [30]:

- **Direct 4f–4f Absorption**: Eu^{3+} ions have well-defined 4f energy levels that can be excited by directly absorbing photons. These transitions within the 4f shell appear as weak absorption bands in the ultraviolet and visible regions. For example, the $^7F_0 \rightarrow 5L_6$ transition occurs near 394 nm. Because these transitions are parity forbidden, their probability is very low, so they have small

absorption cross-sections. This means that strong light sources or specific resonance conditions are needed to excite them effectively. While this direct excitation can be observed in spectroscopic studies, it usually plays a minor role in practical devices.

- **Charge Transfer Transitions**: In addition to 4f–4f transitions, Eu^{3+} ions can be excited via charge transfer transitions. In this process, an electron is promoted from the valence band or an oxygen ligand (O^{2-}) to the Eu^{3+} ion, temporarily forming a Eu^{2+}– O^{-} configuration. This charge transfer absorption occurs in the ultraviolet region, typically between 250 and 300 nm, and has a much higher probability than intra-4f transitions. After excitation, the system relaxes non-radiatively back to the 4f excited states of Eu^{3+}, which then emit their characteristic luminescence as they return to the ground state.
- **Energy Transfer from the Host Matrix:** In ZnO doped with Eu^{3+}, energy transfer from the host matrix is crucial for the excitation process. When ZnO absorbs ultraviolet (UV) light, it creates electron-hole pairs known as excitons. These excitons can either recombine radiatively within ZnO (producing near-band-edge or defect-related luminescence) or transfer their energy to Eu^{3+} ions via non-radiative processes. Once excited, the Eu^{3+} centres relax back to their ground state by emitting their characteristic red luminescence. This sensitised energy transfer pathway allows for efficient excitation under UV illumination and is one of the main reasons why ZnO is regarded as an effective host material for Eu^{3+} activators.
    - **Luminescence of Divalent Europium (Eu^{2+}) :** Eu^{2+} emission arises from allowed transitions between the 5d and 4f levels:

$$4f^7\,5d^2 \longrightarrow 4f^7$$

These transitions produce broad and intense emission bands, typically appearing in the blue or green regions, depending on the host material. In some materials, Eu^{2+} can be stabilised by using reducing synthesis conditions or hosts with suitable crystal fields.

I.5.Radiative and Non-Radiative Processes :

The luminescence of Eu^{3+} ions results from a balance between radiative and non-radiative transitions that occur after excitation.

I.5.1. Radiative Transition: Radiative transitions involve the emission of a photon as the Eu^{3+} ion decays from an excited state to a lower energy level within the 4f manifold. These processes produce the characteristic sharp emission lines of Eu^{3+}. The radiative lifetime of the $5D_0$ level typically ranges from 1 to 3 milliseconds in most oxide hosts, depending on the host matrix and the local site symmetry. For ZnO: Eu, values around 1–2 milliseconds are commonly reported in the literature [31]. These relatively long decay times are beneficial for applications requiring persistent luminescence.

I.5.2. Non-Radiative Transition: Non-radiative transition refers to processes in which the excited Eu^{3+} ion dissipates its energy to the lattice as vibrations (phonons) instead of emitting a photon. This reduces luminescence efficiency. One main pathway is multi-phonon relaxation, where the energy gap is bridged by emitting several phonons at once. This happens more easily if the gap is small or if the material has strong vibrations, like O–H bonds. For Eu^{3+}, these gaps are large, so this process is usually slow, helping maintain good emission. Another mechanism is energy transfer to defects or impurities, which can trap energy and quench luminescence, especially in materials with many defects. Finally, cross-relaxation can occur at high Eu^{3+} concentrations, where an excited ion transfers energy to a neighbour, reducing the number of ions that emit light.

I.5.3.The Relationship Between Radiative and Non-Radiative Transition: The total decay rate (K_{tot}) from the excited state is the sum of radiative (K_r) and non-radiative (K_{nr}) rates:

$$K_{tot} = K_r + K_{nr} \qquad \text{..... I.2}$$

The quantum efficiency (η) of luminescence is given by :

$$\eta = \frac{K_r}{K_{tot}} \qquad \text{..... I.3}$$

A high (k_r) and low (K_{nr}) favour efficient emission, and engineering the host material to have low phonon energies, minimal defects, and optimal site symmetry helps maximise luminescence efficiency.

I.6.Thermal Quenching Behaviour :

Thermal quenching refers to the reduction in luminescence intensity as temperature increases. For europium-doped materials, this effect occurs because heat activates non-radiative transitions. As the lattice temperature rises, the phonon population increases, and the probability that excited Eu^{3+} ions lose their energy through multi-phonon relaxation also grows. In ZnO: Eu, thermal quenching typically becomes significant above approximately 250 °C. This relatively high threshold is an advantage over many other phosphors[3].

I.7.Europium Doped Zinc Oxide (ZnO: Eu):

I.7.1. Europium Incorporation Mechanisms:

The ionic radius of Eu^{3+} (~0.95 Å in octahedral coordination) is significantly larger than Zn^{2+} (~0.74 Å in tetrahedral coordination). As a result, Eu incorporation into ZnO occurs via several mechanisms:

- **Interstitial incorporation**: Eu^{3+} occupies interstitial sites, which are less energetically favourable.
- **Substitutional doping:** Eu^{3+} replaces Zn^{2+} sites, introducing local lattice strain due to size mismatch and charge imbalance.
- **Segregation and secondary phase formation:** For higher doping levels, Eu_2O_3 or Eu-rich clusters may precipitate.

The way europium integrates into ZnO depends significantly on the dopant quantity (concentration), the technique used to prepare the material (nano-powders or thin films), and the thermal processing conditions (temperatures applied during synthesis).

Not: DFT calculations show substitutional incorporation is more stable at moderate doping.

I.7.2. Solubility Limits of Europium in ZnO :

The solubility limit of a dopant in a host lattice defines the maximum concentration of dopant ions that can be incorporated into the crystal structure without forming secondary phases or precipitates. In the case of ZnO: Eu, this limit is governed

[3] A phosphor is a substance that absorbs energy (like UV or X-rays) and re-emits it as visible light.

by several factors, including ionic size mismatch, charge compensation requirements, and thermodynamic stability.

Several studies have reported approximate solubility limits for Eu in ZnO:

- ~2%: Generally considered the practical limit for substitutional incorporation without significant secondary phase formation [32]
- 2–3%: Secondary phases such as cubic Eu_2O_3 or Eu-rich clusters become detectable in XRD and TEM.
- >5%: Substantial precipitation of Eu_2O_3, strong phase segregation, and degradation of structural and optical properties

Strategies to Improve Solubility: While the intrinsic solubility limit is

thermodynamically constrained, certain strategies can enhance effective Eu incorporation:

- **Co-doping**: Introducing other ions (like Li^+) to help balance charge and reduce lattice strain.
- **Low-temperature synthesis + rapid quenching:** Kinetic trapping of dopant ions in metastable states.
- **Thin film growth under non-equilibrium conditions:** Techniques like pulsed laser deposition (PLD) can increase local solubility.
- **Optimising annealing protocols:** Carefully controlled thermal treatments to minimise diffusion and segregation.

I.8. Judd-Ofet Analysis

The Judd–Ofelt model [33] was developed to calculate the probabilities of radiative transitions between the 4f energy levels of excited trivalent rare-earth ions embedded in a host material. For a specific ion in a given matrix, three intensity parameters Ω_2, Ω_4, and Ω_6 are extracted from the absorption spectrum. These parameters characterize the interaction between the rare-earth ion and the surrounding ligand field. They provide insight into the local structure around the ion and the degree of covalency in the rare-earth–ligand bond. As such, the rare-earth ion serves as a sensitive local structural probe. In framwork of this theory, the strength of each transition at a given wavelength is determined from the absorption spectra and is expressed in terms of the integrated absorption cross-section, as described by the following relation:

$$S_{JJ'}^{mes} = \frac{9n}{(n^2+2)^2}\left[\frac{3hc\varepsilon_0}{2\pi^2 e^2}\right]\frac{1}{\bar{\lambda}}(2J+1)\int \sigma_{abs}(\lambda)d\lambda \quad \text{..... I.4}$$

where n is the refractive index, h denotes Planck's constant,c is the speed of light in vacuum, e represents the electron charge, *J* is the orbital momentum of the ground state and $\int \sigma_{abs}(\lambda)d\lambda$ is the integral of the absorption cross section. The magnetic dipole part of the transition $M_{JJ'}^{DM}$ is calculated from the relationship:

$$S_{JJ'}^{DM}\left(\frac{h^2}{4\pi mc}\right)|\langle J\|L+2S\|J'\rangle|^2 \quad \text{..... I.5}$$

The electric dipole transition force $M_{JJ'}^{DE}$ is guven by the relationship:

$$\boldsymbol{S_{JJ'}^{DE_{mes}} = \frac{9n}{(n^2+2)^2}\left[\frac{3hc\varepsilon_0}{2\pi^2 e^2}\frac{1}{\bar{\lambda}}(2J+1)\sigma_{mes} - nS_{JJ'}^{DM}\right]} \quad \text{.... I.6}$$

Solving a system of equations with three unknowns using a least-squares approximation provides access to the parameters Ω_2, Ω_4, and Ω_6. These parameters are then compared to the experimental values obtained from the emission spectrum and to the calculated intensities of the electric dipole transitions.

I.9. Structural and Phase Behaviour of ZnO: Eu Materials in Diverse Configurations (nano-powders and thin films)

The structural and morphological properties of ZnO: Eu are typically examined using a combination of X-ray diffraction (XRD), Raman spectroscopy, scanning electron microscopy (SEM), EDS Mapping and transmission electron microscopy (TEM). These techniques help reveal how europium incorporation affects crystal structure, phase composition, and microstructure.

- **Crystallinity and Lattice Parameters**: ZnO retains its wurtzite hexagonal

structure upon Eu doping at low europium concentrations (<1–2% Eu), sometimes with a slight shift to lower diffraction angles due to lattice expansion. However, at higher doping levels (>2–3%), the structure becomes unstable, which may lead to the formation of secondary Eu-containing phases, such as Eu_2O_3, as well as peak broadening resulting from lattice strain. Raman spectroscopy complements XRD by detecting subtle disorder in the crystal lattice. Doping often results in an increased

background signal, indicating the presence of amorphous or defective regions, along with broadening and intensity changes of the E_2(high) and A_1(LO) modes of ZnO that reflect lattice distortion. Additionally, possible Eu–O vibrational modes may appear when secondary phases are present. The presence of these phases is generally undesirable because they can degrade the optical properties of ZnO: Eu and limit the uniformity of dopant distribution

- **Morphology:** Morphologically, Eu doping significantly influences grain growth

and surface texture. In nanoparticle systems, the introduction of europium often hinders the growth of large crystallites, resulting in smaller, more irregularly shaped grains and increased porosity. SEM and TEM images frequently reveal that the doped nano-powders and films display rougher surfaces and a more porous microstructure compared to undoped ZnO. For thin films, Eu incorporation can reduce the degree of preferred orientation (texture), often decreasing the c-axis alignment typically observed in undoped ZnO films deposited by sol-gel or sputtering methods.

I.10. Optical and Luminescent Properties :

I.10.1. Optical Absorption Properties (Bandgap): The optical band gap of ZnO: Eu

It is generally studied using UV–Vis diffuse reflectance spectroscopy or transmission measurements. ZnO: Eu exhibits optical absorption characteristics that arise from both the ZnO host lattice and the incorporated Eu^{3+} ions. ZnO itself is a wide bandgap semiconductor with a direct band gap of approximately 3.3 eV (around 375 nm), which leads to strong absorption in the near ultraviolet region. In addition, Eu^{3+} ions introduce narrow intra-4f absorption bands in the UV and visible ranges. These 4f-4f transitions are parity forbidden and therefore have low absorption cross sections. A prominent example is the $^7F_0 \rightarrow {}^5L_6$ transition, which appears near 394 nm [34]. Despite their weak intensity, these lines serve as spectroscopic fingerprints of Eu^{3+}. At low doping concentrations (<1 to 2%), the band gap typically shows only minor variations compared to undoped ZnO, generally ranging from 3.25 to 3.3 eV (around ~375 to 387 nm)

I.10.2. Photoluminescence: When Eu^{3+} ions are incorporated into the ZnO lattice,

Several changes in luminescent behaviour occur compared to undoped ZnO. They change how the material emits light. Pure ZnO typically shows broad UV or blue emission around 380 nm [35]. After europium is added, this emission is partly suppressed because energy is transferred from the ZnO host to the Eu^{3+} ions. As a result, ZnO: Eu exhibits strong, sharp red luminescence, mainly from the $5D_0 \rightarrow 7F_2$ transition near 612 nm. The local environment around Eu^{3+} in ZnO is often distorted, which further enhances the red emission intensity. However, at higher doping levels, defects and clustering can form, which may reduce luminescence efficiency.

I.10.3. Electrical and Dielectric Properties :

The incorporation of Eu^{3+} ions into the ZnO lattice influences not only the structural and optical characteristics of the material but also plays a crucial role in altering its electrical and dielectric properties. Doping with Eu^{3+} can introduce localised energy levels within the bandgap, which may act as trapping or recombination centres for charge carriers. As a result, the electrical conductivity of ZnO: Eu can either increase or decrease depending on the doping concentration, defect states, and synthesis conditions. From a dielectric perspective, Eu^{3+} ions affect the polarisation behaviour of the material. The substitution of Zn^{2+} ions by Eu^{3+} ions leads to charge imbalance, which is often compensated by the formation of oxygen vacancies or interstitials. These defects contribute to space charge polarisation, especially at grain boundaries, enhancing the dielectric constant at lower frequencies. Moreover, the dielectric loss is typically influenced by the hopping mechanism of localised charge carriers between defect sites. The frequency dependence of the dielectric constant and loss tangent reflects the presence of interfacial polarisation and the relaxation behaviour induced by the dopant. Such modifications are critical for tailoring ZnO-based materials for applications in electronic devices, capacitors, and sensors.

I.11. Lithium Doped Zinc Oxide (ZnO :Li) :

Doping ZnO with lithium (Li) is a widely used strategy to tailor its electrical, optical, and structural properties. Lithium, being a small and monovalent alkali ion (Li^+), can interact with the ZnO lattice in multiple ways. The impact of Li doping on ZnO depends strongly on the concentration of lithium, the preparation method, and the temperature of synthesis or annealing. The primary motivations for Li doping are to improve conductivity, control defect structures, and potentially achieve p-type ZnO.

I.11.1. Structural Considerations :

Li^+ ions can enter the ZnO lattice in two possible ways:

- **Substitutional sites (Li^+ replaces Zn^{2+})**: In this case, a Li^+ ion replaces a Zn^{2+} ion in the wurtzite ZnO structure. Since Li^+ carries only a single positive charge, this substitution introduces an acceptor level to maintain charge neutrality—potentially enabling *p-type conductivity*.
- **Interstitial sites (Li^+ occupies space between atoms)**: Li^+ can also reside in interstitial positions within the ZnO lattice, which tends to act as a *donor*, contributing extra electrons and promoting *n-type conductivity*.

XRD studies generally show that low-concentration Li doping does not significantly distort the ZnO crystal structure. However, a slight shift in diffraction peaks may indicate lattice contraction or expansion due to ionic radius mismatch. At higher concentrations, Li incorporation may lead to secondary phases such as Li_2O or LiZnO, especially if the solubility limit is exceeded.

I.11.2. Electrical Properties :

The electrical conductivity of ZnO:Li is highly dependent on the site occupation of Li^+ and the defect chemistry of the host material.

- **Low doping levels** often increase conductivity due to the generation of free carriers (especially if Li occupies interstitial sites).
- **High doping levels** may lead to defect clustering, which can reduce carrier mobility by increasing scattering or recombination events.
- **Ambipolar behavior**: ZnO:Li may show n-type, p-type, or mixed conduction depending on synthesis conditions. However, stable p-type ZnO remains challenging due to compensation by intrinsic defects (like oxygen vacancies).

The resistivity of ZnO can be tuned over several orders of magnitude by adjusting the Li content, making it suitable for applications where precise control of electrical properties is required.

I.11.3. Dielectric Properties :

Lithium doping significantly affects the dielectric behavior of ZnO:

- **Dielectric Constant** : Typically increases with Li doping, particularly at low frequencies, due to enhanced space charge polarization at grain boundaries.
- **Dielectric Loss** : Also increases with Li content, especially at higher doping levels, due to defect-induced relaxation processes.
- **Frequency Dependence**: At higher frequencies, the dielectric constant usually decreases, reflecting the inability of dipolar entities to follow rapid changes in the electric field.

These behaviors are consistent with Maxwell–Wagner polarization and hopping conduction models, commonly observed in doped oxide semiconductors.

I.11.4. Mechanisms of Charge Transport :

- **Hopping conduction**: Especially at low temperatures and in polycrystalline samples, Li doping facilitates hopping of charge carriers between localized states.
- **Defect-related conduction**: Li doping may introduce acceptor or donor states that affect carrier trapping, recombination, and activation energy.
- **Grain boundary effects**: Charge accumulation at grain boundaries (due to dopant segregation or oxygen vacancies) strongly influences electrical and dielectric properties.

I.12.ZnO Co-Doped with Europium and Lithium (ZnO:Eu,Li)

Co-doping ZnO with both Eu^{3+} and Li^{+} has emerged as a powerful strategy to synergistically enhance the optical, electrical, and structural properties of ZnO-based materials. The simultaneous incorporation of a Eu^{3+} and an Li^{+} allows fine control over crystallinity, defect chemistry, and charge transport mechanisms. These effects contribute to improved photoluminescence and conductivity, making ZnO:Eu,Li suitable for diverse applications.

I.12.1. Structural Considerations :

The co-doping of ZnO with Eu^{3+} and Li^{+} ions results in complex interactions within the wurtzite ZnO lattice:

- **Eu^{3+} Substitution:** Replaces Zn^{2+}, creating local lattice distortions due to size mismatch (Eu^{3+} ≈ 0.95 Å > Zn^{2+} ≈ 0.74 Å), and introduces trivalent states that act as luminescent centers.
- **Li^{+} Substitution/Interstitials:** Li^{+} can either substitute Zn^{2+} or occupy interstitial sites. Substitution leads to acceptor behavior, while interstitials contribute donor levels.

Co-doping improves the crystallinity and grain orientation of ZnO thin films by reducing internal stress and promoting better packing. XRD typically shows enhanced peak intensity and narrowing of FWHM, indicating improved crystalline quality.

I.12.2. Electrical Properties

The electrical behavior of ZnO:Eu,Li is significantly modified due to the combined effects of both dopants:

- **Carrier Concentration:** Li^{+} increases carrier density when occupying interstitial positions. This facilitates improved electrical conductivity compared to ZnO:Eu alone.
- **Defect Compensation:** Li^{+} helps neutralize defect states induced by Eu^{3+} doping, such as oxygen vacancies or zinc interstitials, which often act as non-radiative recombination centers.
- **Reduced Resistivity:** Co-doping generally leads to lower resistivity due to improved carrier mobility and reduced trapping.

These improvements are valuable for designing devices requirin

I.12.3. Optical and Luminescent Properties :

ZnO:Eu,Li shows enhanced luminescence compared to ZnO:Eu due to improved excitation transfer and defect passivation:

- **Red Emission from Eu^{3+}:** The characteristic emissions of Eu^{3+} ions, particularly the $^5D_0 \rightarrow {}^7F_2$ transition at ~612 nm, are more intense in the presence of Li^+ due to enhanced local symmetry and reduced quenching centers.
- **Energy Transfer Enhancement:** Li^+ incorporation may improve charge transfer from the ZnO host to the Eu^{3+} ions, enhancing radiative recombination.
- **Defect State Modulation:** Li^+ modifies native defects like oxygen vacancies and zinc interstitials, which are critical in tuning the visible emission (green and blue bands) of ZnO.

The photoluminescence spectrum of ZnO:Eu,Li typically exhibits a strong UV emission from ZnO band-edge, red emission from Eu^{3+}, and a suppressed broad visible band compared to ZnO:Eu, indicating fewer defects.

I.12.4. Dielectric Properties :

- **Dielectric Constant:** Increased due to enhanced space-charge polarization introduced by defect dipoles and Li-related states.
- **Dielectric Loss:** Lower than in singly doped systems due to better crystallinity and reduced leakage pathways.
- **Frequency Response:** Shows relaxation behavior typical of defect-mediated polarization and Maxwell–Wagner-type interfacial effects.

These features make ZnO:Eu,Li promising for microwave and RF devices as well as high-k dielectric applications.

I.13. Application of ZnO and Its Doped Derivatives

Zinc oxide (ZnO) is a multifunctional semiconductor with a wide bandgap (3.37 eV) and high exciton binding energy (60 meV). Through doping with elements such as lithium (Li^+) and europium (Eu^{3+}), its properties can be significantly modified, enabling its use in a wide variety of applications. Below is a summary of the key applications of pure and doped ZnO materials.

I.13.1. Pure ZnO

Properties:

- Wide bandgap semiconductor
- Intrinsic n-type conductivity
- Strong UV absorption
- High thermal and chemical stability
- Piezoelectric and pyroelectric properties

Applications:

- UV Photodetectors: Sensitive to UV radiation with fast response time
- Gas Sensors: Detection of gases like H_2, NO_2, CO due to surface sensitivity
- Piezoelectric Devices: Pressure and strain sensors, energy harvesting
- Sunscreens and Cosmetics**:** UV-blocking agents
- Transparent Conductive Oxides (TCOs)**:** In solar cells and flat-panel displays
- Varistors**:** For surge protection in electronic circuits

➢ **ZnO Doped with Lithium (ZnO:Li)**

Modified Properties:

- Enhanced or tunable electrical conductivity (n- or p-type depending on Li site)
- Improved grain size and crystallinity
- Modified dielectric properties
- Better defect control and lower leakage current

Applications:

- Transparent Conductive Films**:** Especially where low resistivity is required
- Thin-Film Transistors (TFTs)**:** In displays, with stable and low-voltage operation
- Gas Sensors: Enhanced sensitivity due to surface modification by Li

- High-k Dielectric Layers: In capacitors and RF devices
- Resistive Switching Devices: For memory (ReRAM) applications

I.13.2. ZnO Doped with Europium (ZnO:Eu)

Modified Properties:

- Introduction of Eu^{3+} energy levels within ZnO bandgap
- Strong red luminescence due to Eu^{3+} (especially $^5D_0 \rightarrow {}^7F_2$ transition)
- Optical activation by UV excitation
- Moderate impact on conductivity

Applications:

- Red-Emitting Phosphors: For white light LEDs and display backlights
- Optical Temperature Sensors: Due to temperature-dependent luminescence
- Bioimaging and Fluorescent Labels: Biocompatible Eu^{3+} based emission
- Security Inks and Anti-Counterfeit Tags**:** Using characteristic sharp emissions
- UV-Excited Luminescent Devices: Enhanced performance due to host–dopant interaction

I.13.3. ZnO Co-Doped with Europium and Lithium (ZnO:Eu,Li)

Synergistic Effects:

- Stronger red emission from Eu^{3+} due to defect passivation by Li^+
- Improved crystallinity and grain alignment
- Enhanced conductivity due to Li-induced carriers
- Better dielectric and luminescent stability

Applications:

- High-Efficiency Red Phosphors: For solid-state lighting (white LEDs)
- Optoelectronic Devices: Transparent and emissive layers in OLEDs and solar cells
- Smart Sensors: Combined electrical and optical response (e.g., dual-mode gas/UV sensors)
- Photodetectors: Enhanced sensitivity to visible and UV light
- Multifunctional Thin Films: In advanced displays, photonics, and nanoelectronics
- Bio-Probes and Nanomedicine: For simultaneous imaging and sensing applications.

CHAPTER II

Preparation and Characterisation of ZnO in Powder and Thin Film Forms via the Sol-Gel Method

CHAPTER II

II.1. Introduction

Our work focuses on the synthesis of nanostructured ZnO in both powder and thin film forms, co-doped with rare earth (Eu^{3+}) and alkali metal (Li^{+}) ions. These dopants are introduced to enhance the structural, optical, and electrical properties of ZnO for potential applications in optoelectronics and radiation detection.

A wide range of synthesis routes have been reported in the literature for producing doped ZnO materials, including solid-state reactions (1), hydrothermal synthesis (2), co-precipitation (3), combustion methods (4), spray pyrolysis (5), chimie douce or "soft chemistry" methods (6), dip-coating (7), and spin-coating techniques (8).

As mentioned in the general introduction to this thesis, among the various synthesis methods, the sol-gel technique, a prominent example of *chimie douce*, is particularly advantageous due to its ability to produce high-purity, nanometric materials with controlled morphology. Moreover, it enables the synthesis of various forms, such as powders, thin films, fibres, and even bulk materials, at relatively low temperatures and costs. In our work, dip-coating, a widely used technique compatible with sol-gel processing, was employed for the deposition of thin films, offering good control over film thickness and uniformity.

This chapter presents the synthesis process adopted in our study, based on the sol-gel method, for preparing both pure and doped ZnO samples in powder and thin film forms. It also provides a comprehensive overview of the characterisation techniques employed to investigate their structural, morphological, optical, and electrical properties.

II.2. The Sol-Gel Method:

II.2.1. General Principles :

The sol-gel method, short for “solution-gelation,” is a flexible wet chemical technique that transforms a colloidal solution (sol) into a solid network (gel). This process allows for the synthesis of inorganic materials at relatively low temperatures, often near ambient conditions (9). It generally involves four main stages:

- **Hydrolysis:** Precursors such as metal alkoxides or metal salts undergo hydrolysis in the presence of water and a stabilising agent (e.g., ethanol or monoethanolamine).

- **Condensation:** Hydrolysed species condense to form a three-dimensional oxide network.
- **Gelation:** The sol gradually transforms into a gel-like structure through polymerisation.
- **Drying and Annealing:** The gel is dried and thermally treated to remove organic residues and crystallise the metal oxide.

The sol-gel process offers several advantages: low-temperature processing, excellent chemical homogeneity, and the ability to tailor the morphology and composition of the final material.

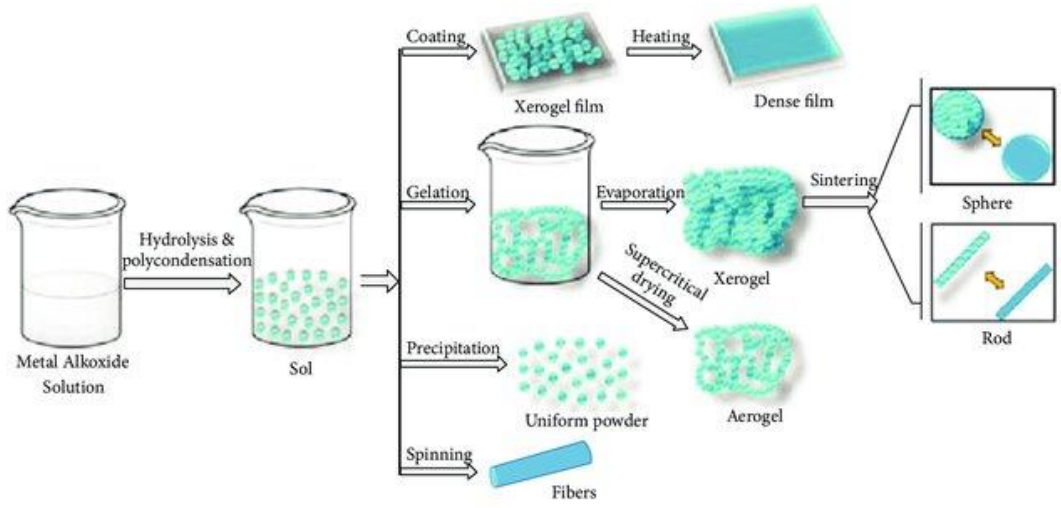

Figure II.1: Schematic Diagram of the Sol-Gel Process and Material Formation Pathways

II.2.2. Factors Affecting the Sol-Gel Process

The sol-gel method is affected by several interdependent parameters that play a crucial role in defining the quality and properties of the final material (10). Proper control of these parameters is vital to ensure reproducibility, uniformity, and the structural, optical, or electrical characteristics of the synthesised materials. The main factors influencing the sol-gel process are discussed in the following section.

- **Precursor Selection:** The choice of precursor is vital in sol-gel chemistry. Metal alkoxides are highly reactive, allowing for rapid hydrolysis and condensation, but they are very sensitive to moisture and require stringent handling conditions.

On the other hand, metal salts such as acetates or nitrates are more stable, easier to manage, and frequently used in the production of doped ZnO materials.

- **Solvent and Stabiliser:** Solvents like ethanol and methanol are commonly employed due to their volatility, miscibility, and ability to support homogeneous mixing. Monoethanolamine (MEA) acts as both a complexing and stabilising agent; it regulates the hydrolysis rate, prevents uncontrolled precipitation, and promotes sol stability, particularly in systems with dopants.
- **pH and Catalyst:** The pH of the reaction medium plays a critical role in controlling the kinetics of hydrolysis and condensation during the sol-gel process, thereby influencing the structure of the resulting gel network. Under acidic conditions, the condensation rate is reduced, promoting the formation of linear polymeric chains and open network structures. Conversely, basic conditions accelerate condensation reactions, favouring the development of spherical colloidal particles and denser, particulate gels. To precisely adjust the reaction environment, acidic or basic catalysts such as nitric acid or ammonia are commonly employed, enabling control over the sol-gel transition and final material morphology.
- **Temperature:** Synthesis temperature influences the kinetics of hydrolysis and condensation. Post-gelation ageing allows for further polymerisation, enhancing network strength.

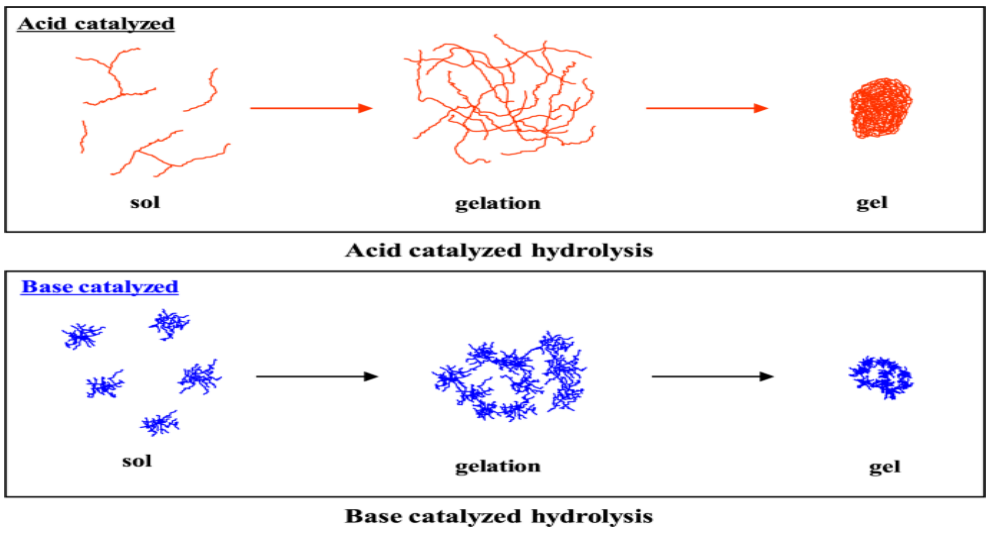

Figure II.2: Structural Evolution of Gels Under Acidic and Basic Catalysis

- **Drying and Calcination:** Drying conditions (air drying, freeze drying, supercritical drying) determine porosity and microstructure. Calcination is required to remove organics and crystallise the ZnO matrix. The typical calcination temperature is 450–550 °C.

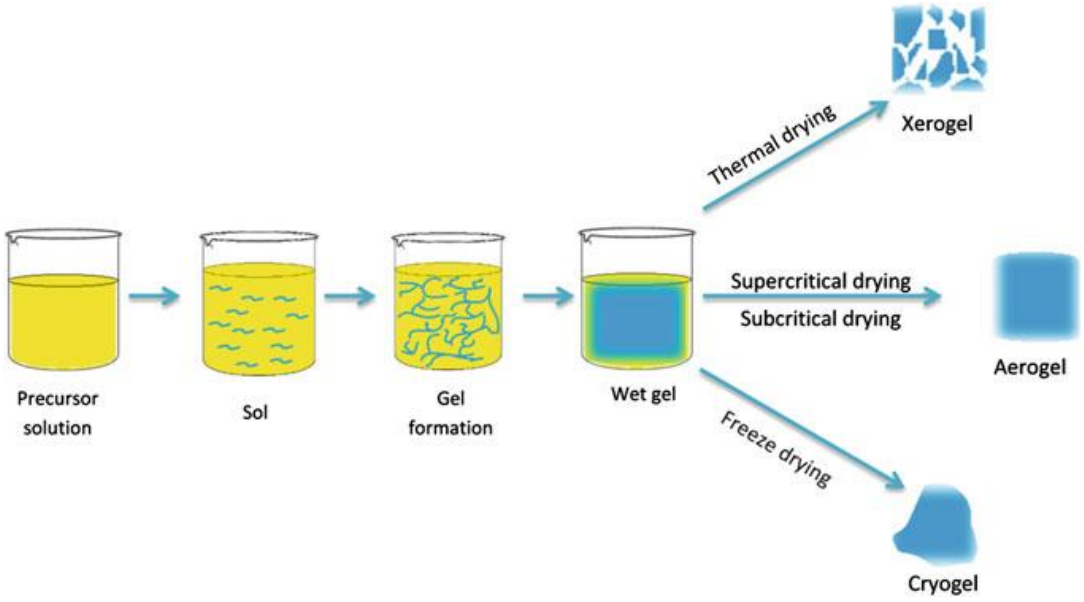

Figure II.3: Sol-Gel Process and Drying Techniques

II.3. Synthesis of ZnO-Based Powders :

The pure ZnO, Li-doped ZnO, and (Eu; Li) co-doped ZnO nanoparticles were synthesised via a sol-gel method using Zinc acetate dihydrate ($Zn(CH_3COO)_2 \cdot 2H_2O$), Europium nitrate pentahydrate ($Eu(NO_3)_3 \cdot 5H_2O$) and Lithium acetate ($LiCH_3COO$) as precursors. The precursor salts were dissolved in 50 mL of deionised water under magnetic stirring for 30 minutes at room temperature. The doping levels were adjusted according to the nominal Zn/Eu/Li molar ratios:

- Pure ZnO: 100% Zn
- Li-doped ZnO: $Zn_{1-x}Li_xO$ (x = 0.07)
- Eu/Li co-doped ZnO: $Zn_{0,98-x}Eu_{0,02}.Li_xO$ (x = 0, 0.02, 0.05, 0.07, 0.10, 0.15)

All chemicals were of analytical grade and used without further purification.

Acid-Assisted Dissolution and Stabilisation: A small amount of nitric acid (HNO_3) was added to each solution to promote complete dissolution and form a clear, homogeneous sol. Polyéthylène Glycol 400 (Peg_{400}) was used as a stabiliser to control the hydrolysis and condensation reactions during sol formation.

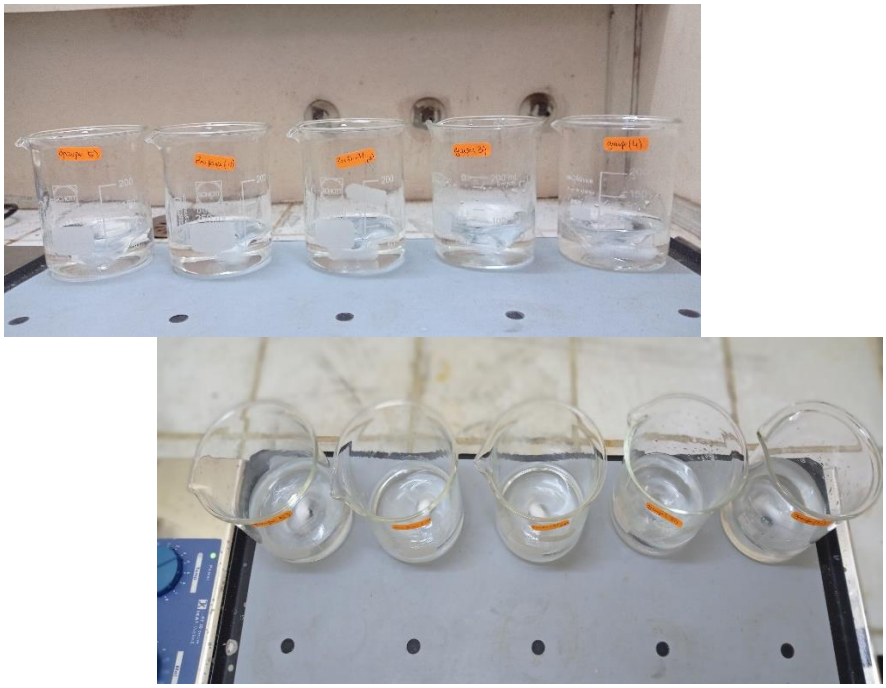

Figure II.4: Solution Preparation of ZnO Based Samples Prior to Gelation

Ageing and pH Adjustment: The sols were aged for 1 hour at room temperature. After ageing, the pH was adjusted to 12 by dropwise addition of ammonia (NH_3).

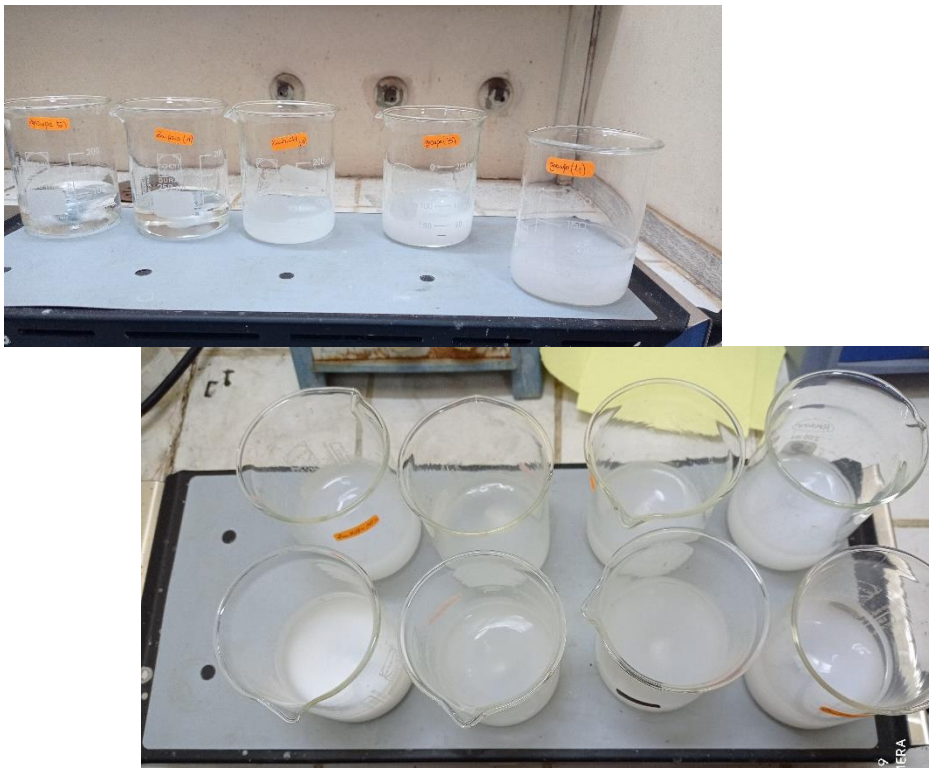

Figure II.5: Pre-gelation Appearance of ZnO-Based Solutions at pH 12

Drying and Calcination: The aged sols were dried in air at 120 °C for 10 hours to form xerogels, which were then ground into fine powders. Final calcination was performed at 550 °C for 1 hour in air to obtain crystalline ZnO-based nanopowders.

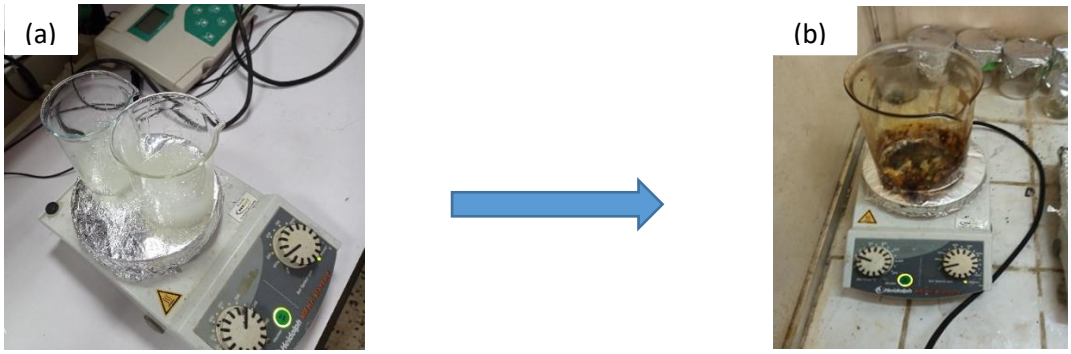

Figure II.6 (a and b): Homogenization and ageing of precursor solutions on a magnetic stirrer with heating

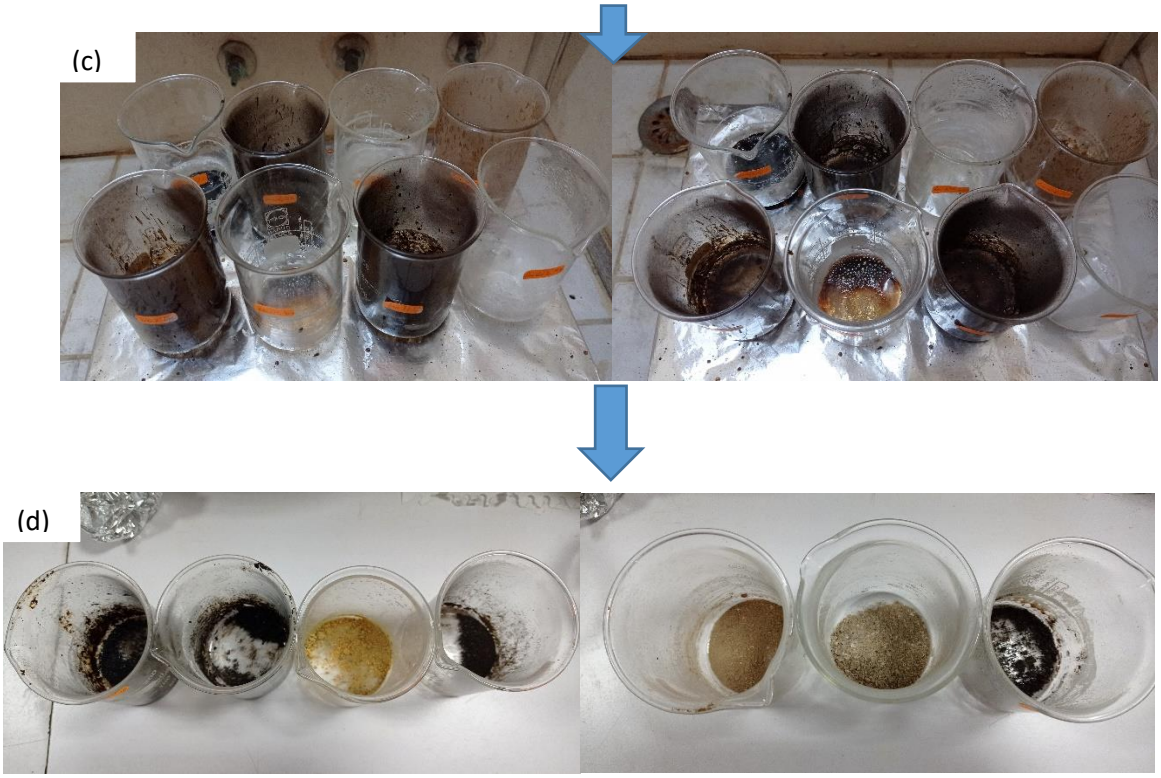

Figure II .6(c and d): Thermal treatment of xerogels: initial calcination stage at elevated temperature

Figure II.6.e : Samples Before and After Calcination: Calcination of Xerogels at 550 °C (Colour Change)

Figure II.6 (a,b,c,d,e): Sequential Drying and Calcination Stages in the Sol-Gel Process

II.3.1. Overview of Sol-Gel-Based Thin Film Deposition Methods :

In the sol-gel process, thin films can be deposited using various techniques that translate the liquid sol into a solid layer on a substrate. Each method has its advantages depending on the desired thickness, homogeneity, surface quality, and application (11) . The most commonly used deposition techniques in sol-gel chemistry include:

- **Dip-Coating Process**: Dip-coating is a simple and cost-effective technique for applying thin, uniform films to substrates. The process involves dipping a substrate into a liquid sol and then withdrawing it at a controlled speed, which determines the film thickness. As the solvent evaporates, a solid layer forms, which is typically heat-treated to enhance its properties. This technique offers excellent uniformity and is ideal for flat surfaces, though it is less suitable for complex shapes. Dip-coating is widely used in optics, sensors, and protective coatings. Figure 7 shows the mechanism of the dip-coating process.

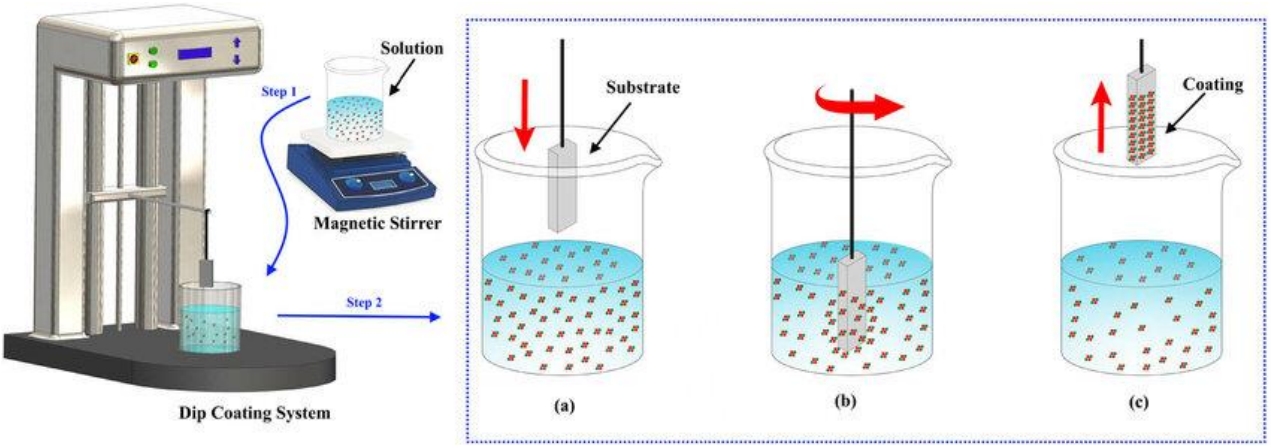

Figure II.7 (12)**: The mechanism of the dip-coating method:**

(a) Dripping, (b) wet layer formation, and (c) evaporation of the solvent.

- **Spin-Coating Process**: Spin-coating is a technique used to create thin, uniform films by depositing a small amount of sol onto the centre of a flat substrate, which is then rapidly spun. The centrifugal force spreads the liquid evenly across the surface, and the solvent quickly evaporates, leaving behind a thin film. This method offers excellent control over film thickness and uniformity. It is ideal for producing very thin layers, particularly in microelectronics and optics, but is limited to small, flat substrates.

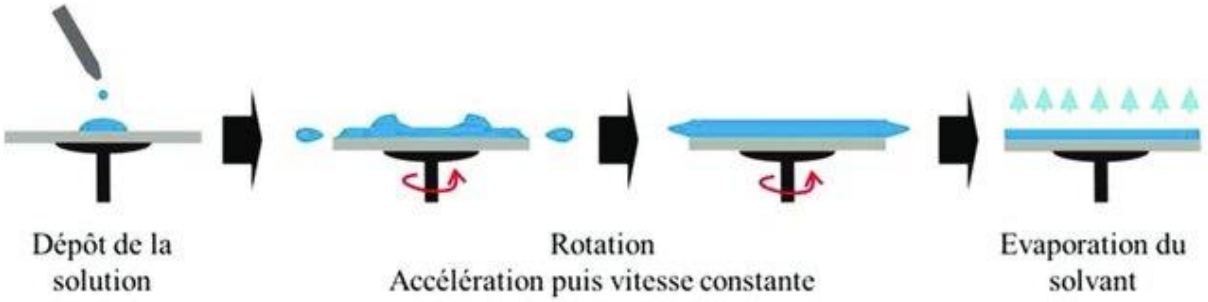

Figure II.8: Spin-Coating Process Diagram

- **Spray-coating (**spray-pyrolysis**):** Spray-coating is a technique where a sol is atomised into fine droplets and sprayed onto a heated substrate. As the droplets contact the surface, the solvent evaporates and forms a solid film. This method is suitable for coating large areas and complex 3D shapes, making it useful in applications like solar cells and sensors. However, controlling film thickness and smoothness requires careful adjustment of parameters such as spray rate, nozzle type, and substrate temperature.

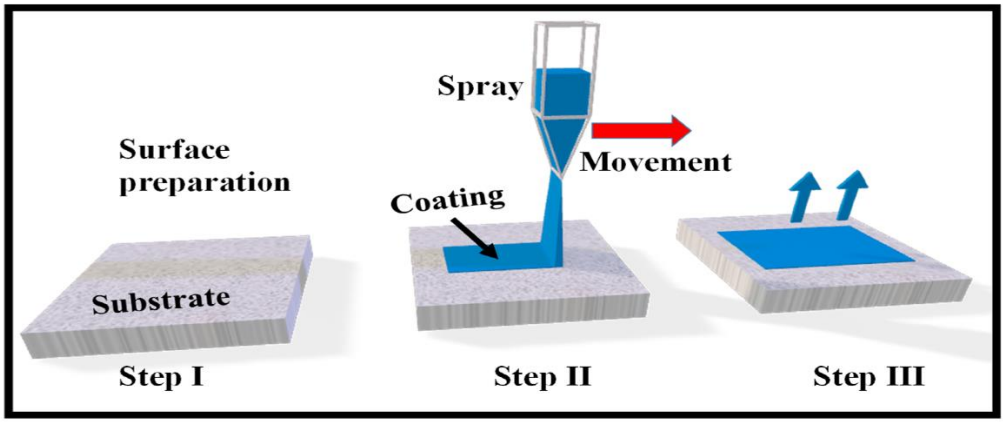

Figure II.9: Spray-coating Process Diagram

II.4. Deposition of Our ZnO-Based Samples by the Dip-Coating Method

In our study, ZnO thin films co-doped with europium (Eu^{3+}) and lithium (Li^{+}) were synthesised using the sol-gel process followed by dip-coating deposition. The dip-coating technique was selected due to its simplicity, low cost, and ability to produce homogeneous, uniform thin films with controlled thickness. The precursor solution was prepared from commercially available chemicals, and glass substrates were used for film deposition.

II.4.1. Chemical Precursors :

- **Zinc source :** Zinc acetate dihydrate ($Zn(CH_3COO)_2 \cdot 2H_2O$)
- **Europium source:** Europium (III) nitrate pentahydrate ($Eu(NO_3)_3 \cdot 5H_2O$)
- **Lithium source:** Lithium acetate (CH_3COOLi, ≥99%)
- **Solvent:** Absolute ethanol (C_2H_6O)
- **Stabilising (complexing agent):** Monoethanolamine (MEA)

II.4.2. Preparation of the Sol-Gel Solution:

The sol was prepared by dissolving zinc acetate dihydrate in absolute ethanol, using monoethanolamine (MEA) as a complexing and stabilising agent. For the doped and co-doped samples, europium nitrate and lithium acetate were added in the appropriate molar ratios. The solution was stirred magnetically at a temperature of 50–60 °C for 1 to 2 hours until a clear and homogeneous sol was obtained. It was then aged for 24 hours at room temperature to ensure complete complexation and sol stability before use. To ensure reproducibility, the same molar concentration and mole amount were used for all prepared solutions.

II.4.3. Influence of Substrate Nature and Cleaning Procedure for Thin Film Deposition:

The choice and preparation of substrates are crucial for producing high-quality thin films. The selection depends on the intended application: some require insulating substrates such as glass, while others require conductive substrates like silicon. Importantly, a thin film of the same material and thickness can exhibit significantly

different physical properties depending on the nature of the substrate on which it is deposited.

In this study, we used one type of substrate, glass. Proper cleaning of this substrate is essential, as even the slightest impurity can lead to contamination, poor adhesion, or delamination of the deposited layers. Therefore, all traces of grease, dust, or other residues must be thoroughly removed. Additionally, the surface condition of the substrates must be carefully inspected to ensure they are free of scratches, cracks, or flatness defects, all of which can interfere with uniform film growth and affect reproducibility.

The substrate cleaning procedure was performed as follows:

- **Cutting:** The substrates were cut to the desired dimensions using a diamond-tipped pen.
- **Brushing and Initial Rinse:** The substrates were gently brushed and rinsed with tap water to remove loose particles and surface dust.
- **Soapy Bath:** The substrates were immersed in a warm soapy solution to remove general surface contaminants.
- **Rinsing:** After the soapy bath, they were thoroughly rinsed with distilled water.
- **Ultrasonic Cleaning:** The substrates were placed in an ultrasonic bath containing ethanol and acetone to eliminate grease, organic residues, and tightly adhered impurities.
- **Final Rinse:** A final rinse with distilled water was performed to remove any remaining solvent residues.
- **Drying:** The cleaned substrates were dried using a stream of nitrogen gas.

After drying, the substrates were wrapped in aluminium foil and stored in a clean environment to protect them from dust and airborne contaminants.

II.4.4. Thin Film Deposition by Dip-Coating: Process Conditions and Optimisation:

Thin film deposition was carried out using the dip-coating method under optimised conditions to achieve a uniform and reproducible layer. The process started with setting a dip start position of 15 mm, followed by immersing and withdrawing the cleaned substrates at controlled speeds of 2000 µm/s and 3000 µm/s, respectively, over a total

travel distance of 135 mm. Each dip lasted about 7 seconds, and the number of layers applied ranged from 5 to 30, depending on the required film thickness.

After each dip, the films were pre-dried at 100 °C for 2 minutes to promote solvent evaporation and minimise interlayer mixing. Once the required number of layers was achieved, the coated samples were subjected to a final annealing step at 500 °C for 1 hour in air. This thermal treatment was essential for enhancing the crystallinity of the ZnO-based films and eliminating residual organic components from the sol-gel precursors.

II.5. Powder and Thin Film Characterisation Techniques :

To assess the performance of europium and lithium in both ZnO powders and thin films, it is crucial to examine their structural, morphological, optical, and other relevant properties. For this purpose, several characterisation techniques were utilised, including X-ray diffraction (XRD), scanning electron microscopy (SEM), Raman spectroscopy, and photoluminescence spectroscopy.

II.5.1. X-ray Diffraction (XRD) :

X-ray diffraction is a powerful, non-destructive analytical technique used to identify crystalline phases and elemental compositions of materials. It also allows for estimation of lattice parameters, crystallite sizes, crystal quality, and residual stresses by comparing diffraction patterns with standard databases such as the Joint Committee on Powder Diffraction Standards (JCPDS).

X-rays are electromagnetic waves with wavelengths ranging from 0.5 to 50 Å, comparable to atomic spacing in crystals. When X-rays pass through a crystal lattice, they are diffracted according to Bragg's law:

$$2d_{hkl}sin\theta = \lambda \qquad \text{..... II.1}$$

Where d_{hkl} is the atomic plane spacing, θ the diffraction angle, and λ the X-ray wavelength.

The diffracted radiation is detected by a counter tube that scans the angular range of reflections, with intensities recorded digitally. The crystallite size D is estimated from the full width at half maximum (FWHM) of the most intense peak using Scherrer's formula:

$$D = \frac{0{,}9\lambda}{\beta\cos\theta} \qquad \text{..... II.2}$$

Where β is the FWHM in radians and θ the Bragg angle.

Figure 10 shows the XRD pattern used to identify the crystalline structure of the prepared ZnO samples and demonstrates the basic principle of X-ray diffraction.

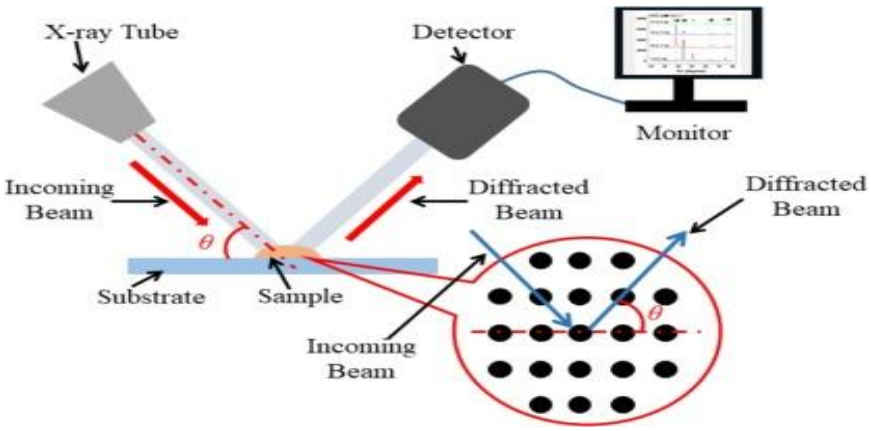

Figure II.10: X-ray diffraction

The dislocation density δ\deltaδ can be calculated from:

$$\delta = \frac{1}{D^2} \qquad \text{..... II.3}$$

Additionally, the X-ray diffraction data can also be used to determine the dimensions of the unit cell using this relation :

$$d_{hkl} = \left(\frac{4}{3}\,\frac{h^2+hk+K^2}{a^2} + \frac{l^2}{c^2}\right)^{-\frac{1}{2}} \quad \text{..... II.4}$$

II.5.2. Scanning Electron Microscopy (SEM) and Energy Dispersive X-ray Spectroscopy (EDX) :

Scanning Electron Microscopy (SEM) is a powerful tool used to examine the surface morphology and microstructure of thin films and powders at high resolution. In this study, SEM analysis was employed to investigate the surface texture, particle size, grain distribution, and film uniformity of the synthesised ZnO-based materials. This technique provides crucial insight into the growth mechanism, homogeneity, and structural integrity of the deposited layers.

To complement the morphological analysis, Energy Dispersive X-ray Spectroscopy (EDX), which is typically coupled with SEM, was used to perform qualitative and semi-quantitative elemental analysis. EDX allows the identification of the chemical elements present in the samples and confirms the successful incorporation of dopants such as europium (Eu^{3+}) and lithium (Li^{+}) into the ZnO matrix. By analysing the EDX spectra, we ensured the elemental purity and composition consistency of the sol-gel-derived materials. Together, SEM and EDX provide a comprehensive understanding of both the physical and chemical characteristics of the synthesised samples.

Figure II.11: Image of the ESEM-XL30-FEG Scanning Electron Microscope Used at CRNA[1]

II.5.3. Raman Spectroscopy :

[1] Nuclear Research Center of Algiers.

Raman spectroscopy is a powerful, non-destructive technique used to investigate the vibrational, rotational, and other low-frequency modes in a material. It is based on the inelastic scattering of monochromatic light, usually from a laser source. When incident photons interact with the molecular vibrations or phonons of a material, a small fraction of the scattered light shifts in energy. This energy shift provides a fingerprint of the material's molecular structure and crystal quality.

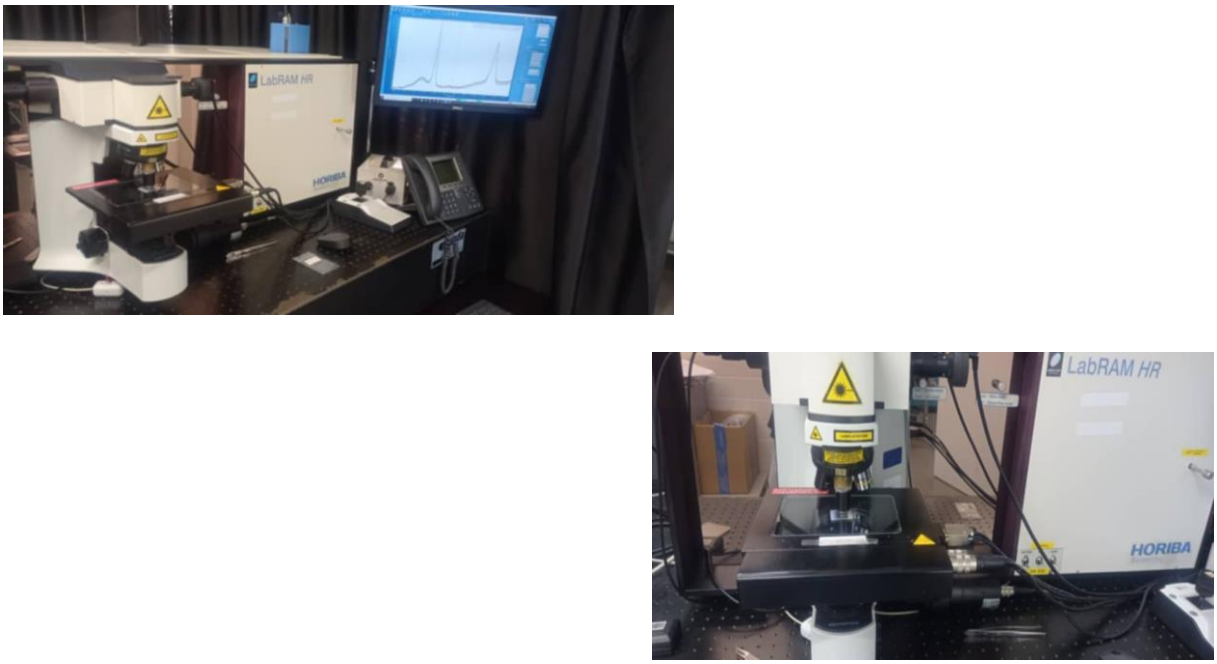

Figure II.12: Image of the Raman Spectroscopy Used

In the context of ZnO-based materials, Raman spectroscopy is particularly useful for assessing crystal structure, lattice dynamics, and the presence of defects or dopant-induced changes. Pure wurtzite ZnO exhibits characteristic Raman active modes, such as the E_2(high) mode around 437 cm^{-1}, which is associated with the oxygen sublattice and is highly sensitive to crystallinity and stress in the lattice. The presence of additional peaks or broadening of these modes may indicate structural disorder, grain boundary effects, or doping effects.

Doping with rare earth (e.g., Eu^{3+}) or alkali metals (e.g., Li^{+}) can lead to shifts in peak positions or the appearance of new modes due to lattice distortions, local vibrations, or defect-related phonon modes. Thus, Raman analysis helps confirm the successful incorporation of dopants and gives insight into the quality and homogeneity of the thin films or powders.

II.5.4. Photoluminescence Spectroscopy (PL)

Photoluminescence (PL) spectroscopy is a powerful, non-destructive optical technique widely used to investigate the electronic and structural properties of semiconductors and insulating materials. The phenomenon of luminescence involves two main stages: (1) excitation of the electronic system of the material, and (2) de-excitation, during which light is emitted. Depending on the lifetime of the excited states, two principal types of luminescence are distinguished: fluorescence, which occurs almost instantaneously after excitation (within ~10^{-8} s), and phosphorescence, which occurs with a delay ranging from milliseconds to several seconds or even longer**.**

In a typical PL experiment, a sample is irradiated with a monochromatic light source, often a laser with a photon energy greater than the material's bandgap. This causes electrons in the valence band to absorb the energy and transition to the conduction band. These excited electrons then relax back to the valence band through radiative or non-radiative processes. In the non-radiative mechanism, energy is dissipated to the lattice via phonons (acoustic vibrations), whereas in the radiative process, the electron recombines with a hole, emitting a photon with energy typically close to the bandgap.

Figure II.13: Image of the PL Used at CRNA

PL emission thus provides a direct probe of the electronic structure of the material. Its non-contact and non-destructive nature makes it particularly attractive for characterising thin films, nanostructures, and doped semiconductors. The excitation energy and intensity can be precisely controlled to explore different transitions and localised regions within a sample.

Photoluminescence spectroscopy offers insight into several key material properties:

- Bandgap Determination: The most prominent PL peak in semiconductors often corresponds to the band-to-band recombination of electrons and holes, allowing for precise determination of the optical bandgap, especially useful in evaluating new semiconductor compositions.
- Impurity and Defect Levels: PL spectra can reveal radiative transitions involving defect states or impurity levels within the bandgap. The energies and intensities of these emissions provide information about the type and concentration of these imperfections.
- Recombination Mechanisms:The balance between radiative and non-radiative recombination is reflected in the PL intensity and its temperature or power dependence. Understanding these mechanisms helps elucidate the dynamics of charge carriers in the material.
- Material Quality Assessment:High-quality materials typically exhibit strong, sharp PL peaks associated with radiative recombination. In contrast, materials with high defect densities show quenched or broadened emissions due to enhanced non-radiative processes. Thus, PL serves as an indirect measure of crystal quality and purity.

Overall, photoluminescence spectroscopy is an indispensable tool for both fundamental research and quality control in materials science, especially in the development of optoelectronic and luminescent devices.

CHAPITRE III
Structural and Optical Investigations of ZnO: Eu^{3+} Nanoparticles Co-Doped with Lithium Ions

III.1. Introduction (Objective of the Study)

The objective of this study is to investigate the structural and optical properties of ZnO nanoparticles doped with europium (Eu^{3+}) and co-doped with lithium (Li^{+}) ions, this work. Particular emphasis is placed on understanding how Li^{+} co-doping influences the incorporation of Eu^{3+} into the ZnO crystal lattice, and how it affects the key material characteristics (crystallinity, morphology, and photoluminescent behaviour) of the resulting materials.

To this end, A series of ZnO-based powders was synthesised with a fixed Eu^{3+} concentration and varying amounts of Li^{+} (2%, 5%, 7%, 10%, and 15%). Comprehensive characterisation was carried out using X-ray diffraction (XRD) to examine crystal structure and crystallite size, Raman spectroscopy to probe phonon modes and detect structural disorder, scanning electron microscopy (SEM) for morphological analysis, energy-dispersive X-ray spectroscopy (EDX) for compositional verification, and photoluminescence (PL) spectroscopy to evaluate the optical emission characteristics.

This work aims to optimise the synthesis conditions and determine the optimal Li^{+} concentration that enhances red emission from Eu^{3+} ions, thereby improving the luminescent performance of ZnO-based materials for potential use in optoelectronic and photonic applications.

III.2. Results and discussion

III.2.1. Structural analysis by X-Ray Diffraction (XRD)

X-ray diffraction (XRD) analysis was employed to investigate the crystalline structure, crystallite size, lattice strain, and microstructural features of the synthesised ZnO-based powders doped with Eu^{3+} and co-doped with Li^{+}. The measurements were performed using a PANalytical X'Pert PRO diffractometer (Philips) equipped with Cu Kα radiation (λ = 1.54059 Å), operated at 45 kV and 40 mA. The diffraction patterns were recorded over a 2θ range of 20° to 80°, and the resulting data were analysed using X'Pert HighScore Plus software in conjunction with commercial databases for peak identification and full width at half maximum (FWHM) calculations.

Figure 1 presents the XRD patterns obtained from HighScore Plus analysis for pure ZnO and ZnO samples co-doped with 2% Eu^{3+} and varying Li^{+} contents.

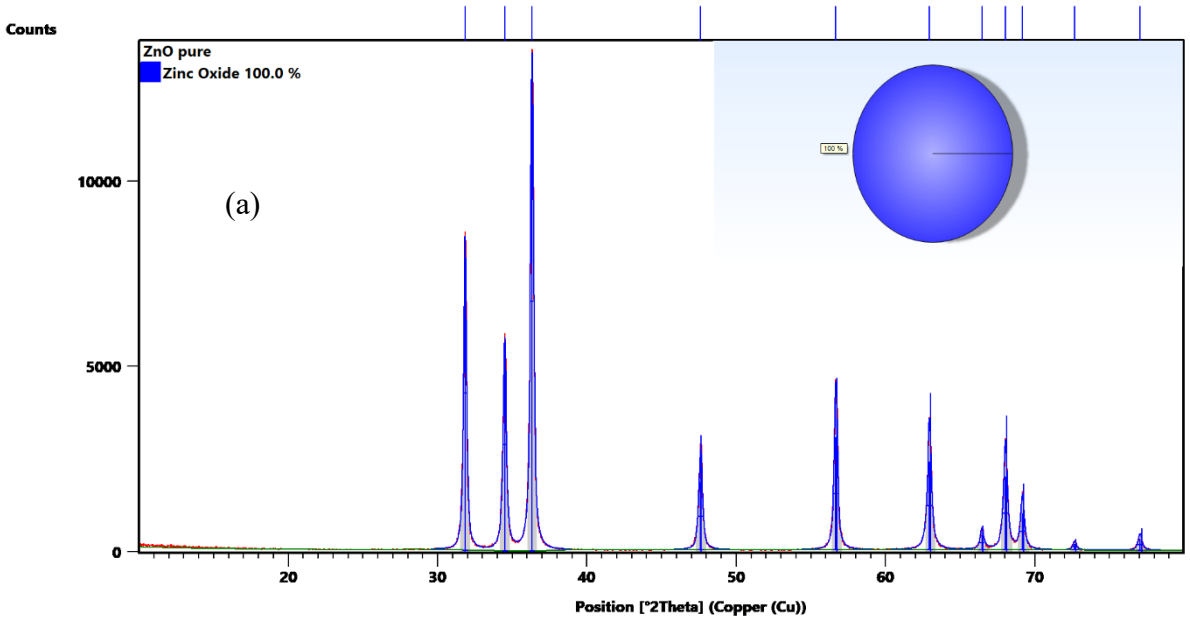
Counts
ZnO pure
Zinc Oxide 100.0 %
100 %
(a)
10000
5000
0
20
30
40
50
60
70
Position [°2Theta] (Copper (Cu))

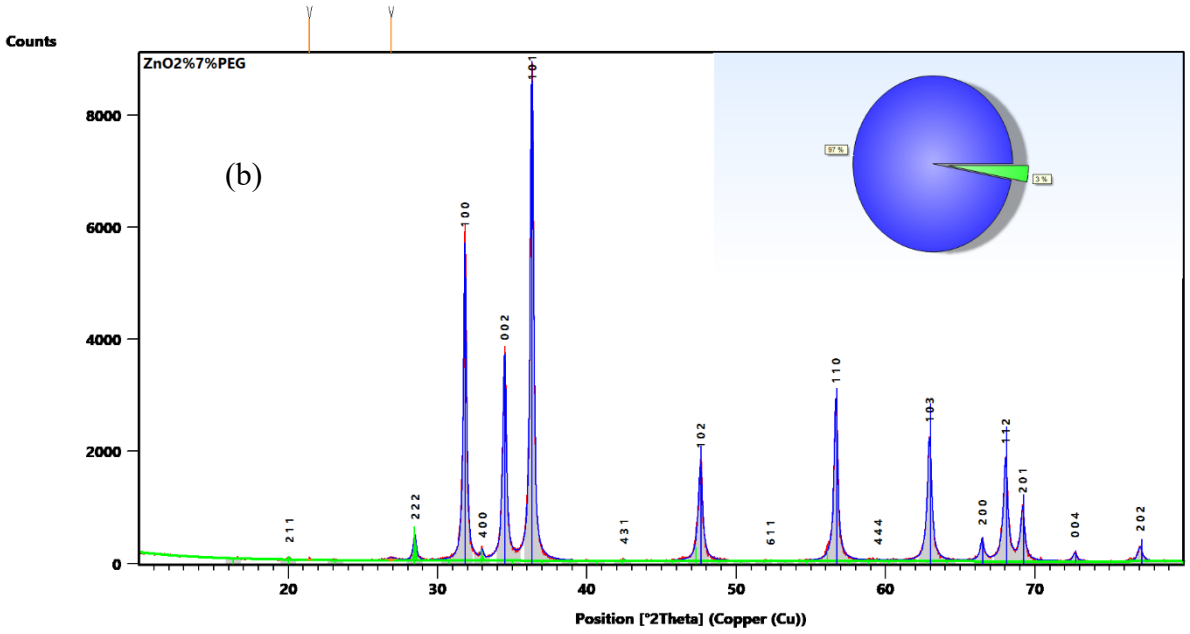
Counts
ZnO2%7%PEG
97 %
3 %
(b)
8000
6000
4000
2000
0
211
222
100
400
002
101
431
102
611
110
444
103
200
112
201
004
202
20
30
40
50
60
70
Position [°2Theta] (Copper (Cu))

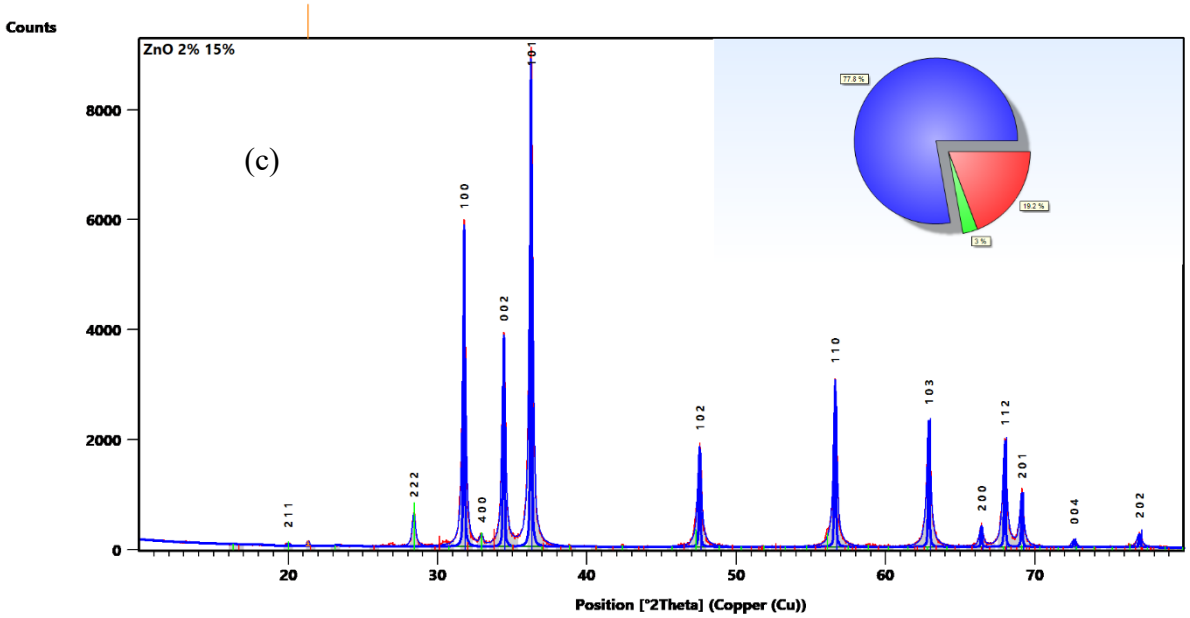

Figure III.1: Example of Refinement processing of X-ray diffraction patterns of pure and (Eu- and Li) co-doped ZnO nanoparticules by Philips HighScore Plus

All diffraction patterns of pure ZnO and ZnO co-doped with 2% Eu^{3+} and varying concentrations of x% Li^{+} (x = 2, 5, 7, 10, and 15%) are shown in Figure 2. These patterns exhibit the characteristic peaks of the hexagonal wurtzite structure of ZnO (space group: $P6_3mc$), with prominent peaks indexed to the (100), (002), (101), (102), (110), (103), (112), and (201) planes. These peaks correspond well with the standard JCPDS card No. 98-002-9272. The results confirm that the (101) plane is the preferred orientation across all samples, regardless of the Eu and Li doping levels.

A very weak diffraction peak observed at $2\theta \approx 28.47°$ is attributed to unreacted or segregated Eu_2O_3 (JCPDS card No. 98-063-1468). This peak is detected in all samples, except for the ZnO samples co-doped with 2% Eu^{3+} and 2% Li^{+}. This observation suggests that the solubility limit of Eu^{3+} in the ZnO lattice is exceeded at high co-doping levels. Such behaviour is consistent with previous reports, which have shown that rare-earth ions tend to segregate and form secondary oxide phases when their concentration surpasses the substitutional incorporation capacity of the host lattice (1,2).

Furthermore, all XRD patterns display sharp and narrow diffraction peaks, reflecting the high crystallinity and phase purity of the synthesized powders. These observations

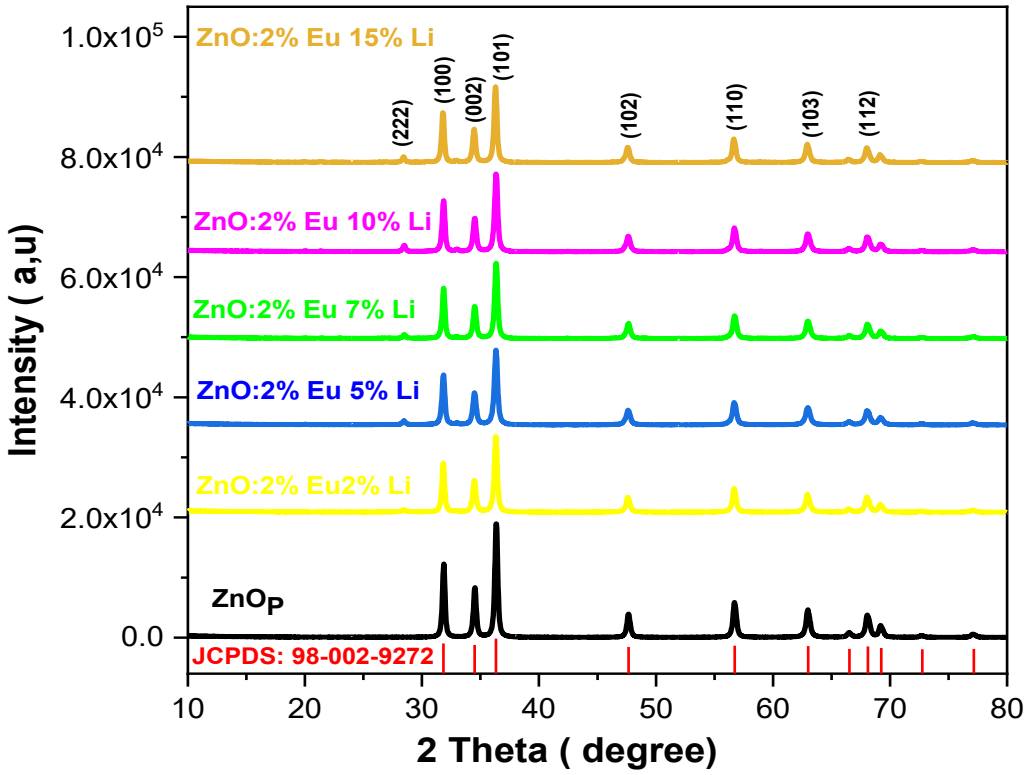

Figure III.2: XRD patterns of undoped ZnO and ZnO: 2% Eu^{3+}, x % Li^{+} (x = 0, 5, 7, 10, and 15 %)

also support the successful incorporation of dopants into the ZnO lattice without significant formation of secondary phases.

The magnified XRD patterns in Figure III.3 show, shift in the (101) diffraction peak position as a function of Li^{+} concentration. Co-doping ZnO with 2 % Eu^{3+} and Li^{+} initially shift the peak toward lower diffraction angle (2θ) values compared to pure ZnO, which increases the lattice parameters and a consequent lattice expansion. This expansion can be attributed to the substitution of Zn^{2+} ions (0.74 Å) by larger Eu^{3+} ions (0.95 Å) and the incorporation of Li^{+} into interstitial sites, both of which tend to stretch the ZnO lattice. With increasing Li^{+} content from 2 to 10 %, the diffraction peak progressively shifts toward higher angles, reflecting a reduction in lattice parameters and suggesting lattice shrinkage.

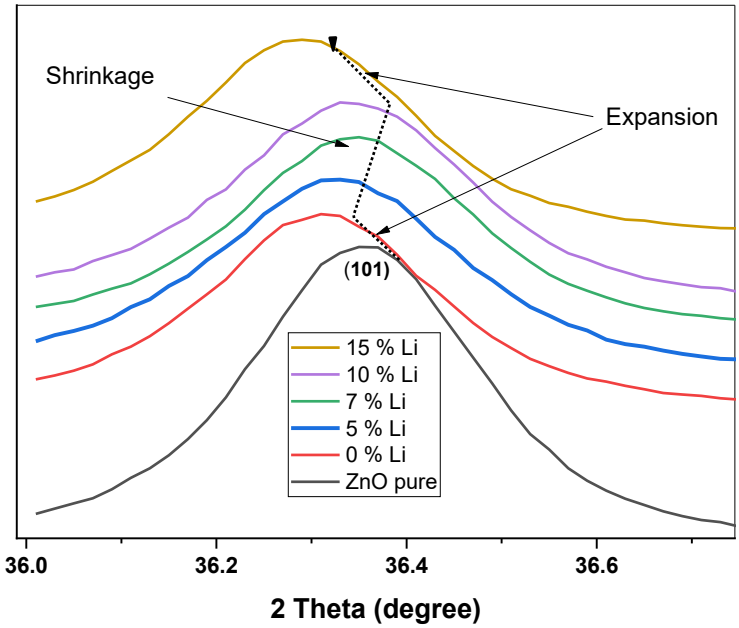

Figure III.3: Shift of the (101) Diffraction Peak in ZnO:2%Eu^{3+} Powders as a function of Li^{+} Concentration (x= 0,5,7,10 and 15%)

This contraction is consistent with Li^{+} ions (0.73 Å) replacing Zn^{2+} ions at substitutional sites, which shortens the Zn–O bond lengths. Similar behaviour has been reported by Shi et al (3)**.** in Li^{+}, Ce^{3+} co-doped ZnO phosphors synthesised via the sol–gel method. At Li^{+} concentrations beyond 10% (e.g., 15%), the peak shifts back toward lower angles, indicating a second expansion phase. This reversal can be explained by excess Li^{+} ions occupying interstitial positions and/or introducing point defects such as oxygen vacancies and zinc interstitials, which distort the lattice outward.

The reduced peak (101) intensity with Li^{+} co-doping of the peak (101), as shown in Figure 4, indicates the important stress and strain applied to the ZnO (NCs), arising from the large mismatch between the ionic radius of Eu^{3+} (0.95 Å) and that of Zn^{2+} (0.74 Å).

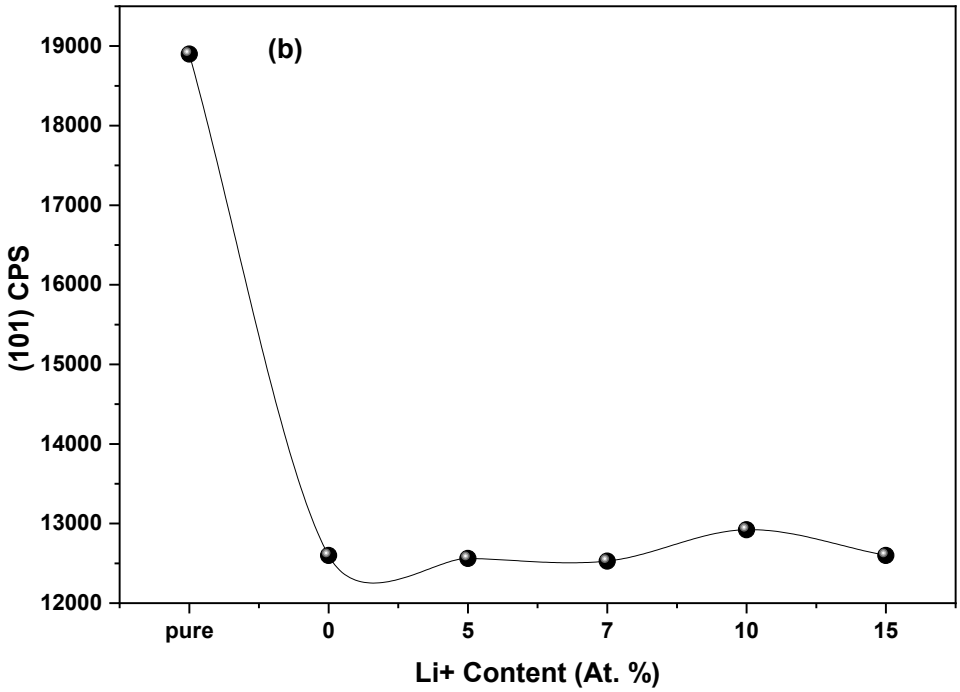

Figure III.4: variation of the intensity of peak (101) for pure ZnO and Li^+ co-doped ZnO: Eu^{3+} nanoparticles with different concentrations of Li^+

Furthermore, it is noted that a further increase in Li^+ concentration does not produce a notable change in peak intensity and thereby the stain, due to the ionic radius of Li^+ (0.73 Å) being very close to that of Zn^{2+}, due to the difference in ionic radii between Eu^{3+} (0.95 Å), Zn^{2+} (0.74 Å), and Li^+ (0.73 Å) ions, the incorporation of these ions into the ZnO lattice results in differences in lattice parameters, as illustrated in the table.1**.** below

These variations are reflected in the calculated values of the unit cell volume was calculated using the hexagonal crystal structure formula:

$$V = \frac{\sqrt{3}}{2} a^2 c \qquad \text{.....III.1}$$

While the Atomic packing fraction (APF) was determined using the expression:

$$APF = \frac{2\pi a}{3\sqrt{3}c} \qquad \text{..... III.2}$$

Moreover, the Zn–O bond length (L) (4), defined by the α parameter for the bond parallel to the c-axis, is determined by the following relationship, which also depends on the lattice constants :

$$\alpha = \frac{a^2}{3c^2} + 0.25 \quad \text{..... III.3}$$

And

$$L = \sqrt{\frac{a^2}{3} + c^2 \times \left(\left(\frac{1}{2} - \alpha\right)\right)^2} \quad \text{..... III.4}$$

Where 'a' and 'c' are lattice parameters.

Table III.1: Structural parameters variation of undoped and (2 % Eu^{3+}, x% Li^{+}) co-doped ZnO powders

Samples		a (A°)	c (A°)	c/a	V(A°3)	APF	L (A°)
Pure ZnO		3.3246	5.2008	1.5643	47.47	0,77296	2.0086
ZnO :2%Eu x%Li	0%Li	3.2480	5.2033	1.6020	47.54	0.75478	1.9766
	5%Li	3.2474	5.2018	1.6018	47.51	0.75486	1.9762
	7%Li	3.2464	5.2007	1.6019	47.47	0.75479	1.9756
	10%Li	3.2469	5.2009	1.6018	47.48	0.75488	1.9759
	15%Li	3.2489	5.2040	1.6017	47.57	0.75489	1.9771

Changes in a and c directly influence both the unit cell volume and the Zn–O bond length, highlighting the structural modifications induced by doping.

While Table 1 summarizes the variations in lattice parameters (a and c), unit cell volume (V) and Zn–O bond length (L) as a function of doping composition, it is equally important to evaluate the corresponding microstructural and mechanical properties.

To this end, Table 2 compiles the average nanoparticle size determined using the Scherrer method approximation:

$$D_{SCH} = \frac{0.9\lambda}{\beta \cos \theta_{(hkl)}} \quad \text{III.5}$$

Where "*D*" is the crystallite size,"λ" is the wavelength of X-rays used (1.54059 A),"β" is the full width at half maximum of a peak (in radians) and "θ" s the diffraction angle corresponding to the (hkl) plane.

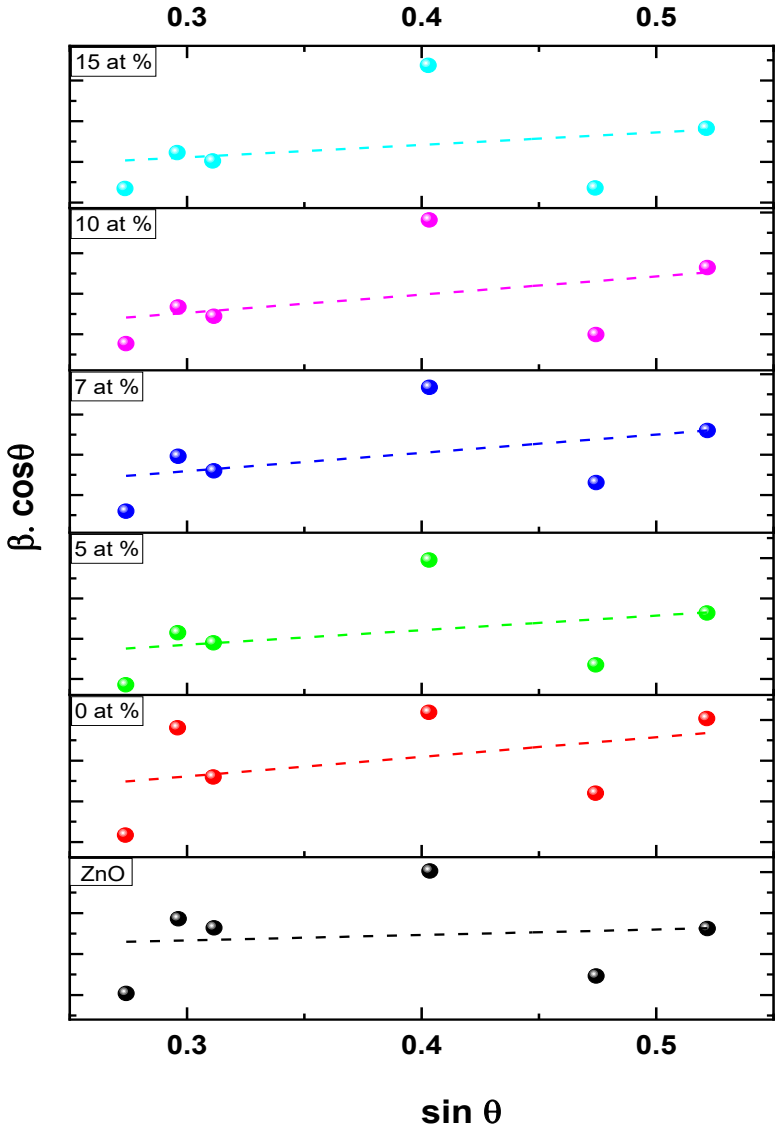

Figure III.5: Linear fit obtained using Williamson-Hall (W-H) analysis of undoped and (Eu^{3+}, Li^{+}) -co-doped ZnO nanoparticles.

The value of "β" is corrected for instrumental broadening and can be calculated using the following equation:

$$\beta = [(\beta_{hkl})^2_{Measured} - (\beta_{hkl})^2_{Instrumental}]^{1/2} \qquad \textbf{III.6}$$

$$\beta_{hkl})_{Measured} = \ Measured\ via\ spectral\ analysis$$

$$(\beta_{hkl})_{Instrumental} = for\ Cu: 0.0027$$

Considering that crystal imperfections also induce lattice strain, the crystallite size was further estimated using the Williamson–Hall (W–H) method, which relates peak broadening to both size and strain effects according to:

$$\beta \frac{\cos\theta}{\lambda} = \frac{1}{D_{W-H}} + \varepsilon \sin(\frac{\theta}{\lambda}) \qquad \textbf{III.7}$$

Here, the strain "*ε*" is calculated from the slope of the linear plot of βcosθ against sinθ and the effective crystallite size "$D_{W\text{-}H}$" is determined from the intercept on the βcosθ axe, as show in Figure. 4.

The dislocation density "δ", representing the total length of dislocation lines per unit volume of the material, can be estimated using the relation (5):

$$\delta = \frac{1}{D^2} \qquad \textbf{III.8}$$

where "*D*" is the crystallite size. Additionally, according to the Uniform Stress Deformation Model (USDM) (6), which assumes uniform stress across all crystallographic directions, there exists a linear proportionality between stress "σ" and strain "ε" expressed as:

$$\sigma = \varepsilon Y_{hkl} \qquad \textbf{III.9}$$

where "*σ* " is the stress in the crystal, "*ε* " is the strain, and Y_{hkl} is Young's modulus (or elasticity modulus) corresponding to the (hkl) plane. For a hexagonal crystal, Y_{hkl} can be calculated using the following equation (7):

$$Y_{hkl} = \frac{\left[h^2 + \frac{(h+2k)^2 + \left(\frac{al}{c}\right)^2}{3}\right]^2}{S_{11}\left(h^2 + \frac{(h+2k)^2}{3}\right)^2 + S_{33}\left(\frac{al}{c}\right)^4 + (2S_{13} + S_{44})\left(h^2 + \frac{(h+2k)^2}{3}\right)\left(\frac{al}{c}\right)^2} \qquad \textbf{III.10}$$

Where *'a'* and *'c'* are lattice parameters; S_{11}, S_{13}, S_{33} and S_{44} are the elastic compliances of ZnO with values 7.8589 $\times 10^{-12}$, -2.2069 $\times 10^{-12}$, 6.9409 $\times 10^{-12}$ and 23.579 $\times 10^{-12}$ $m^2.N^{-1}$, respectively (8).

Also, for systems that obey Hooke's law, the energy per unit volume stored in the lattice due to strain can be estimated by the relation (9):

$$U = \frac{1}{2}\sigma\varepsilon = \frac{1}{2}Y_{hkl}\,\varepsilon^2 \qquad \text{III.11}$$

Thereby offering a comprehensive view of how doping influences both the crystalline quality and the mechanical stability of the ZnO-based materials.

Table III.2: Microstructural and Mechanical Properties of ZnO-based Materials Derived from XRD Analysis

Sample	D_{SCH} (nm)	W-H		Dislocation $\times10^{-4}$ δ (nm)$^{-2}$	Young $\times10^{11}$ (Pa)	U $\times10^{4}$ (J/m^3)	σ $\times10^{7}$ (Pa)
		D_{SCH} (nm)	$\varepsilon \times10^{-4}$ (%)				
ZnO pure	31	33	0.83	9.18274	1.18858	0.40941	0.98652
ZnO :Eu (0%Li)	31	35	4.2	8.16327	1.18857	10.48319	4.99199
ZnO :Eu (5%Li)	27	31	5.15	10.4058	1.18858	15.76206	6.12119
ZnO :Eu (7%Li)	30	35	5.45	8.16327	1.18857	17.65175	6.47771
ZnO :Eu (10%Li)	30	36	6.05	7.71605	1.18857	21.75232	7.19085
ZnO :Eu (15%Li)	31	34	3.35	8.65052	1.18858	6.66942	3.98174

The structural and microstructural properties of ZnO and ZnO co-doped with Eu^{3+} and varying concentrations of Li^+ are summarised in Tables 1 and 2. The lattice parameters a and c exhibit slight variations with doping; a ranges approximately from 3.32 Å in pure ZnO to 3.24 Å in the ZnO: Eu(x%Li) samples, while c varies from 5.2008 Å to 5.2040 Å. The unit cell volume V remains relatively stable around 47.47–47.57 Å^3, indicating that the incorporation of Eu^{3+} and Li^+ ions does not significantly distort the overall lattice volume.

The c/a ratio, which approaches the ideal hexagonal value of 1.633, shows minor fluctuations with co-doping, suggesting a trend toward increased crystal symmetry as Li^+ concentration rises. This supports the idea that dopants substitute Zn sites in the wurtzite lattice.

The Zn–O bond length (L) also shows slight variation, with undoped ZnO having a higher bond length (~2.0086 Å) compared to co-doped samples (~1.9762–1.9771 Å), consistent with literature values and indicating subtle lattice relaxation due to doping.

The average nanoparticle size estimated by the Debye–Scherrer method decreases from 31 nm for pure ZnO to a minimum of 27 nm at 5% Li doping, then fluctuates slightly with higher Li content. Using the Williamson–Hall method, crystallite sizes are larger, ranging from 31 to 36 nm, while the strain (ε) increases with Li co-doping, reflecting the lattice distortions caused by the simultaneous incorporation of Li^{+} and Eu^{3+} ions and synthesis conditions. As illustrated in Figure 6, which plots the variation of crystallite size (D) and lattice strain (ε) for the (101) plane against different Li concentrations, the reduction in crystallite size at moderate Li levels is accompanied by a noticeable increase in strain. This trend confirms that Li incorporation induces local lattice distortions and slightly disrupts crystal growth, particularly at intermediate doping levels.

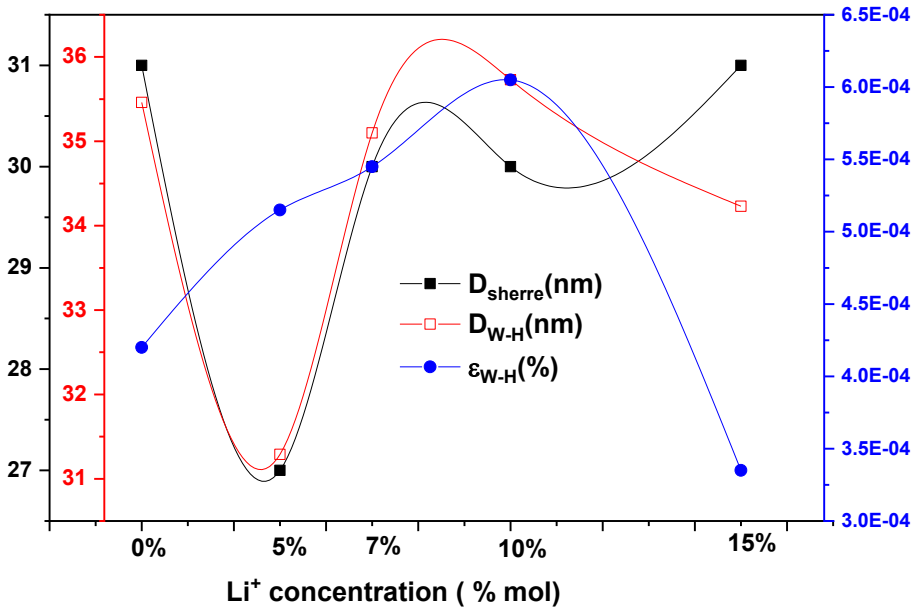

Figure III.6: The variation of crystallite size and lattice strain (D and ε) of the plane (101) with the different Li concentrations

The dislocation density (δ), calculated as the inverse square of the crystallite size, shows minor variations, reflecting the degree of crystalline defects and dislocations in the samples.

Notably, the Young's modulus (Y) remains nearly constant across all samples (~1.18858 × 10^{11} Pa), indicating that doping doesn't significantly affect the elastic properties of the ZnO lattice. However, the strain energy density (U) increases significantly with Li content, reaching a maximum at 10% Li, before decreasing at 15% Li, which suggests that lattice strain and defect density initially rise with doping but reduce slightly at higher concentrations. Similarly, internal stress (σ) shows an increasing trend up to 10% Li doping, indicating enhanced mechanical stress within the crystal lattice due to dopant incorporation

Overall, the data suggest that co-doping ZnO with Eu^{3+} and Li^{+} ions affects both the structural symmetry and microstructural quality, optimising crystallite size and strain while influencing mechanical stability. These changes are crucial for tailoring the material's optical and electronic properties for potential applications.

III.2.2. Morphological and Elemental Analysis (SEM and EDX)

Field-emission scanning electron microscopy (FE-SEM) combined with energy-dispersive X-ray spectroscopy (EDS) was employed to examine the morphology and particle size of the samples annealed for 1 h at 550 °C. The elemental composition of each sample was determined using the EDS system attached to the SEM, and spectra were acquired for all compositions.

Figure 7 presents a comparison of the morphologies of pure ZnO and ZnO: Eu^{3+} powders co-doped with x% Li (x = 0, 5, 7, and 10), highlighting the effects of Li incorporation on particle shape, size, and agglomeration.

- **General Observations**

SEM images show that undoped ZnO powders consist of quasi-spherical nanoparticles that are irregularly packed and form loose agglomerates. The average particle diameter determined from SEM images is ~30 nm, in reasonable agreement with crystallite sizes estimated from XRD. Upon doping with Eu^{3+} and co-doping with Li^{+}, the particle morphology and packing change: particles become more irregular and tend to adopt a block-like and interparticle contacts increase. Overall particle size remains

of the same order, but the degree of agglomeration and apparent grain boundaries vary with Li content.

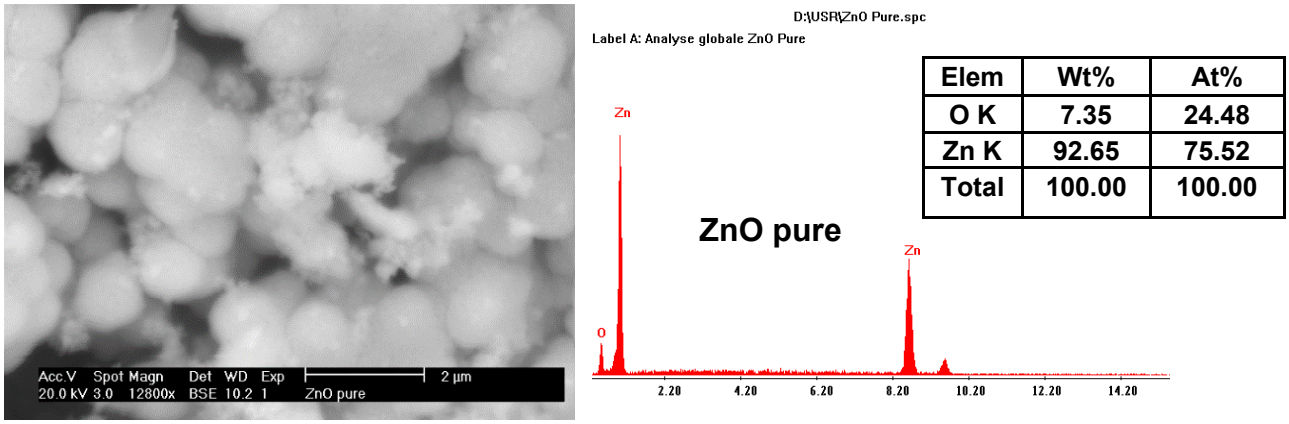

Elem	Wt%	At%
O K	7.35	24.48
Zn K	92.65	75.52
Total	100.00	100.00

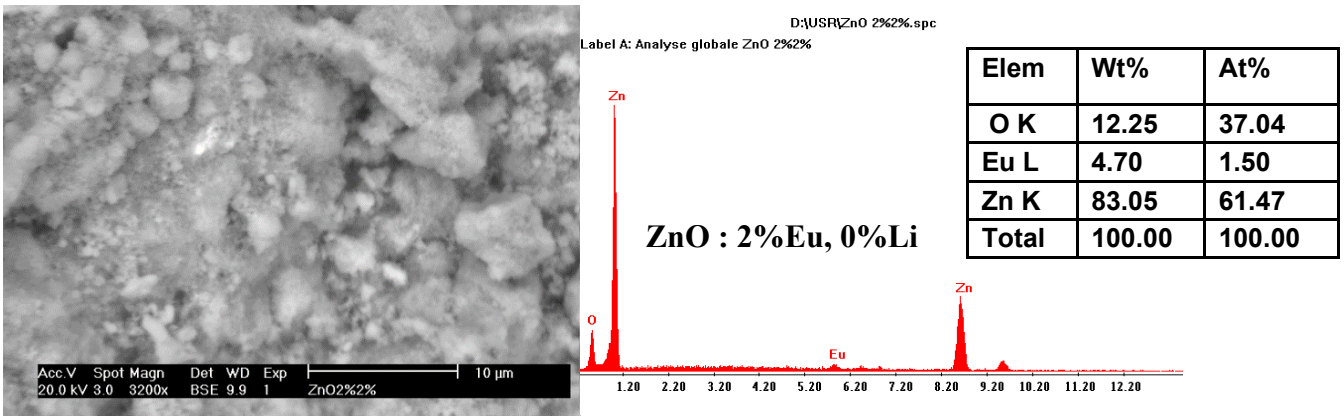

Elem	Wt%	At%
O K	12.25	37.04
Eu L	4.70	1.50
Zn K	83.05	61.47
Total	100.00	100.00

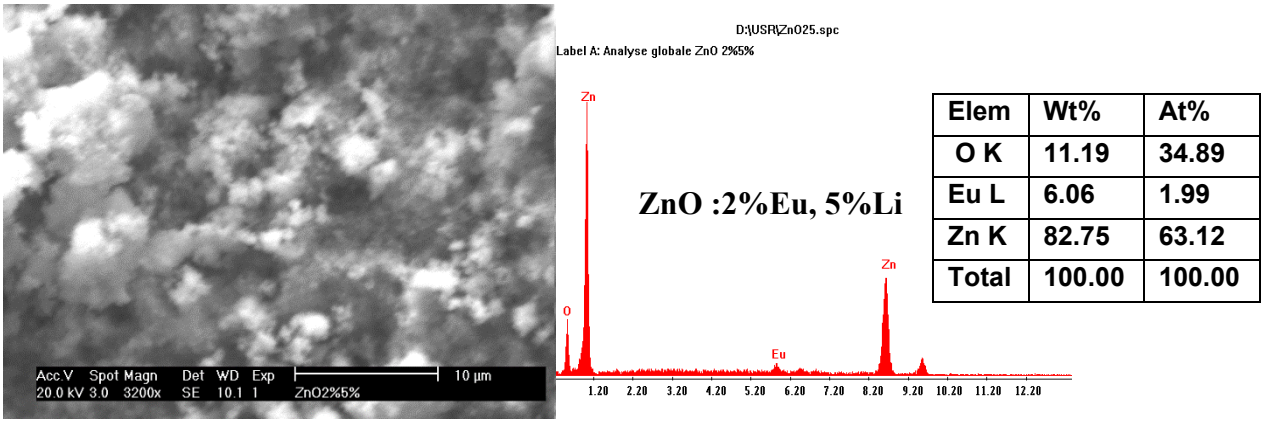

Elem	Wt%	At%
O K	11.19	34.89
Eu L	6.06	1.99
Zn K	82.75	63.12
Total	100.00	100.00

Figure III.7a: SEM images, Backscattered electron image, and EDS chemical analysis

- **Effect of Eu^{3+} and Li^{+} Co-Doping on ZnO**

A systematic change in morphology is observed with increasing Li concentration. At low Li content (ZnO:2%Eu 5%Li), only modest differences are seen compared to the undoped Li sample (ZnO:2%Eu 0%Li); particles remain predominantly spherical but exhibit slightly greater aggregation. At intermediate Li levels (7–10%), the particles become more compact and better sintered, indicating enhanced crystallinity and increased surface diffusion during annealing. At the highest Li concentration examined (15%), the morphology displays more pronounced block-like features and occasional larger agglomerates, suggesting local structural rearrangements or the onset of secondary phase segregation.

These SEM observations are consistent with the XRD results: samples with sharper, narrower diffraction peaks generally show more compact and well-defined particles in SEM images. The mean particle diameters obtained from SEM remain close to those estimated from the XRD Scherrer analysis (≈27–36 nm), with the smallest mean size typically occurring at 5% Li consistent with both the Williamson–Hall and Scherrer calculations. Furthermore, EDS spectra confirm the presence of Zn and O in all samples, verifying the successful formation of ZnO.

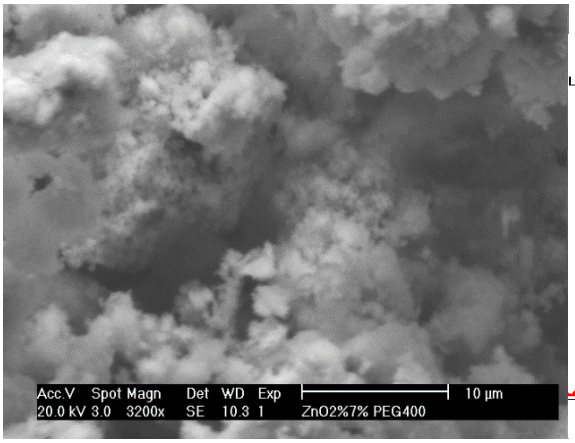

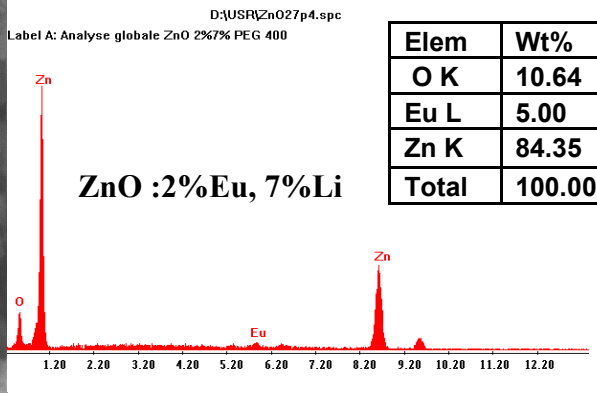

Elem	Wt%	At%
O K	10.64	33.45
Eu L	5.00	1.66
Zn K	84.35	64.89
Total	100.00	100.00

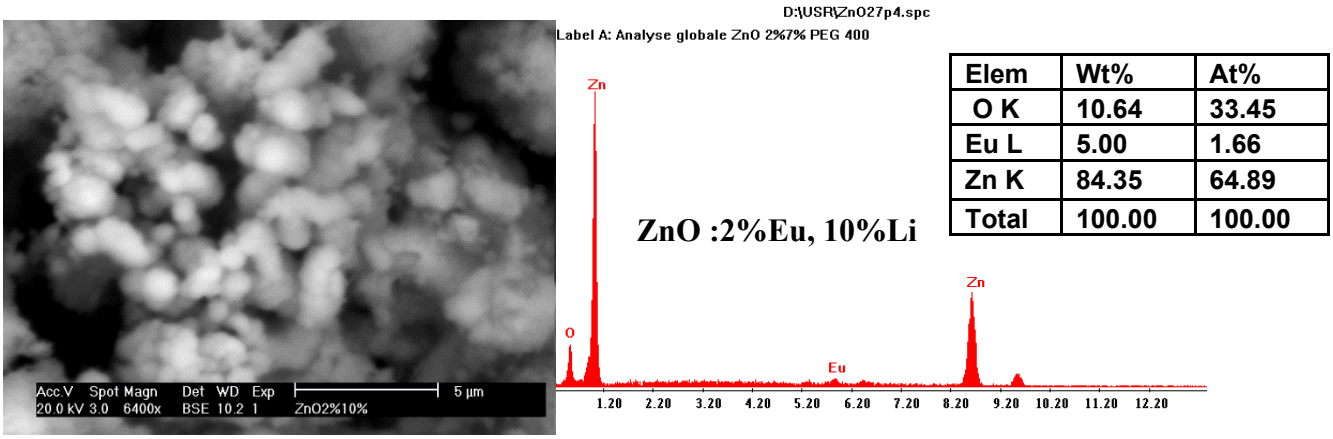

Elem	Wt%	At%
O K	10.64	33.45
Eu L	5.00	1.66
Zn K	84.35	64.89
Total	100.00	100.00

Figure III.7b: SEM images, Backscattered electron image, and EDS chemical analysis of ZnO:2%Eu 7%Li and ZnO:2%Eu 10%Li

Elemental Analysis to (Zn, O, Eu) further confirms these findings. They reveal a relatively homogeneous distribution of Eu at the microscale for most samples, with no large Eu-rich clusters visible at the SEM resolution, supporting the conclusion that Eu is predominantly incorporated into the ZnO matrix rather than forming macroscopic Eu_2O_3 inclusions. The only exception is the sample with the highest Li content, which exhibits a very weak Eu_2O_3 XRD peak.

- **Constraints in Detecting Li in ZnO: Eu, Li Samples via EDS**

Lithium (Li) is not reliably detected by conventional SEM-EDS because of its very low atomic number and correspondingly weak X-ray emission (and overlap with light element background). Therefore, the absence of a clear Li signal in EDS spectra doesn't imply that Li is not incorporated; it is a limitation of the technique. Confirmation of Li incorporation must therefore rely on indirect evidence (changes in lattice parameters from XRD, shifts in Raman modes, systematic changes in PL, and DFT results).

III.2.3. Raman Spectroscopy Analysis

Raman spectroscopy is an essential and versatile diagnostic tool for studying crystallisation, structural disorders, and defects in micro- and nanostructures. Unlike conventional techniques such as X-ray diffraction, which may fail to detect very small structural fluctuations, or transmission electron microscopy (TEM), which requires meticulous sample preparation and specific environments, Raman scattering provides

a non-destructive alternative. Its sensitivity to lattice vibrations makes it particularly effective for probing structural configurations at the nanoscale, where changes such as particle size reduction can systematically alter the Raman profile. In this work, Raman scattering experiments were performed at room temperature using 325 nm and 515 nm laser lines as excitation sources. Figure 8 shows the Raman spectrum of pure ZnO nanoparticles (a) λ = 325 nm (UV) and (b) λ = 514.7 nm (green, visible)

The Raman spectrum of pure ZnO, shown in figure 8a, excited with a 325 nm laser, exhibits two prominent peaks at approximately 573.53 cm^{-1} and 1148.68 cm^{-1}, corresponding to the first-order longitudinal optical phonon mode $A_1(LO)$ and its second-order overtone $2A_1(LO)$, respectively. The sharpness and intensity of these peaks, along with the absence of additional peaks associated with structural defects or impurities, provide clear evidence of the wurtzite crystal structure of ZnO and confirm the high crystallinity and purity of the sample.

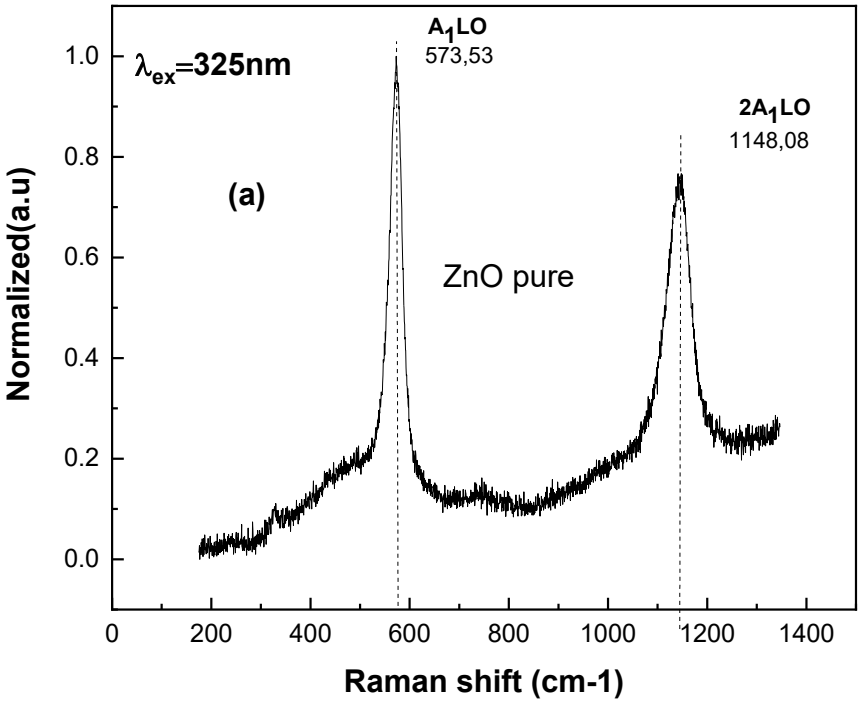

Figure III.8a: Raman spectra of pure ZnO: (a) λ = 325 nm

The Raman spectrum of ZnO nanoparticles recorded with a 514.7 nm laser (Figure 1b) provides detailed information about the ZnO material's long-range order and phonon defect interactions. Visible excitation penetrates deeper into the sample but exhibits less resonance enhancement compared to UV, making it less sensitive to electronic transitions while still allowing observation of lattice vibrations.

The characteristic phonon modes of hexagonal wurtzite ZnO (space group $P6_3mc$) are observed at 98.63, 385.87, 440.59, 580.45, and 595.51 cm^{-1}, corresponding to the E_2(low), A_1(TO), E_2(high), A_1(LO), and E_1(LO) modes, respectively, while a second-order phonon mode appears at ~175 cm^{-1}, assigned to $2E_2$(low). Multi-phonon scattering modes are also detected at 330.85, 508.74, 662, and 1153.15 cm^{-1}, corresponding to E_2(high)–E_2(low), E_1(TO)+E_2(low), 2[E_2(high)–E_2(low)], and A_1(TO)+E_1(TO)+E_2(high), respectively. Although the intensities of these peaks are generally weaker and defect-related modes are less pronounced than under UV excitation, this wavelength is particularly useful for assessing the effects of dopants (Eu^{3+}, Li^+) on lattice vibrations without strong resonance influence.

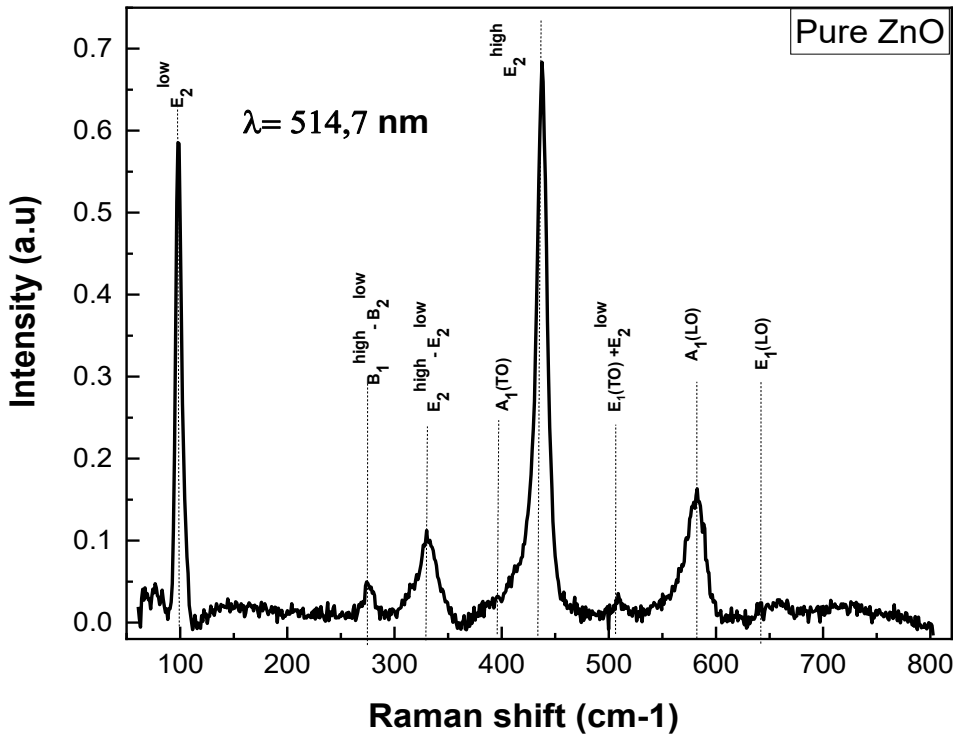

Figure III.8b: Raman spectra of pure ZnO: (b) λ = 514.7 nm

These spectral features are consistent with the well established Raman fingerprint of high quality wurtzite ZnO, where six optical modes at the **Γ** point of the Brillouin zone (A_1 + $2B_1$ + E_1 + $2E_2$) are predicted by group theory (10), with A_1 and E_1 as polar modes split into longitudinal optical (LO) and transverse optical (TO) components, and E_2 modes as non-polar vibrations associated with the oxygen and zinc sublattices.

Co-doping with Li^+ and Eu^{3+} further modifies the Raman spectra as shown in Figure 9 (a and b). Li^+ ions, with a smaller ionic radius, occupy interstitial or substitutional sites, compensating lattice strain introduced by Eu^{3+} and affecting phonon dynamics. The E_2(high) mode shows slight broadening and minor shifts, and LO-related modes increase in intensity, reflecting enhanced defect interactions. These changes indicate that co-doping alters the local environment of ZnO, potentially influencing both structural and optical properties, such as defect-mediated luminescence and carrier dynamics.

Overall, Raman spectroscopy demonstrates that doping with Eu^{3+} and co-doping with Li^+ introduces controlled lattice distortions and defect states while preserving the wurtzite structure of ZnO.

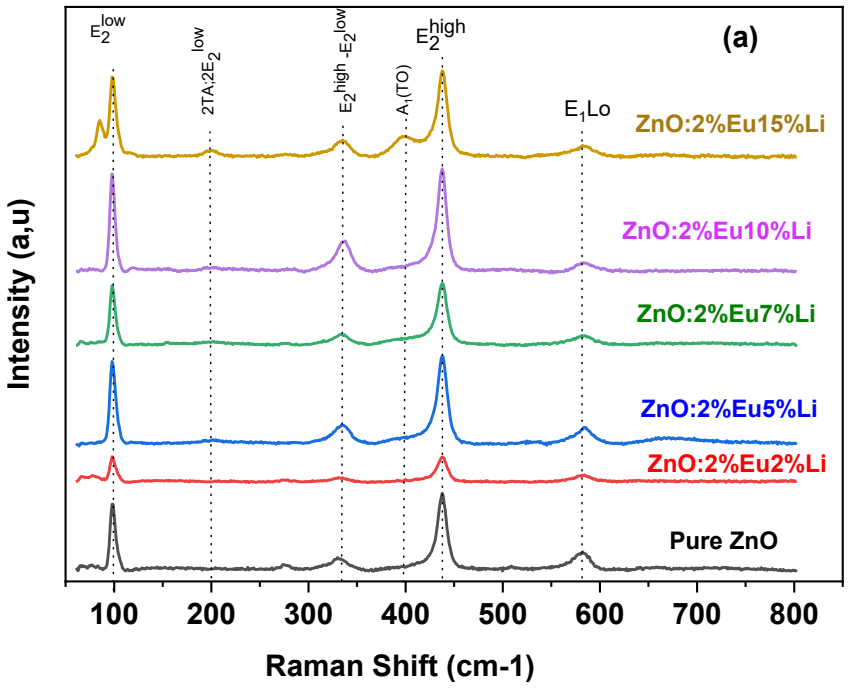

Figure III.9a: Raman spectra of undoped and Eu3+, Li + co-doped ZnO nanoparticles

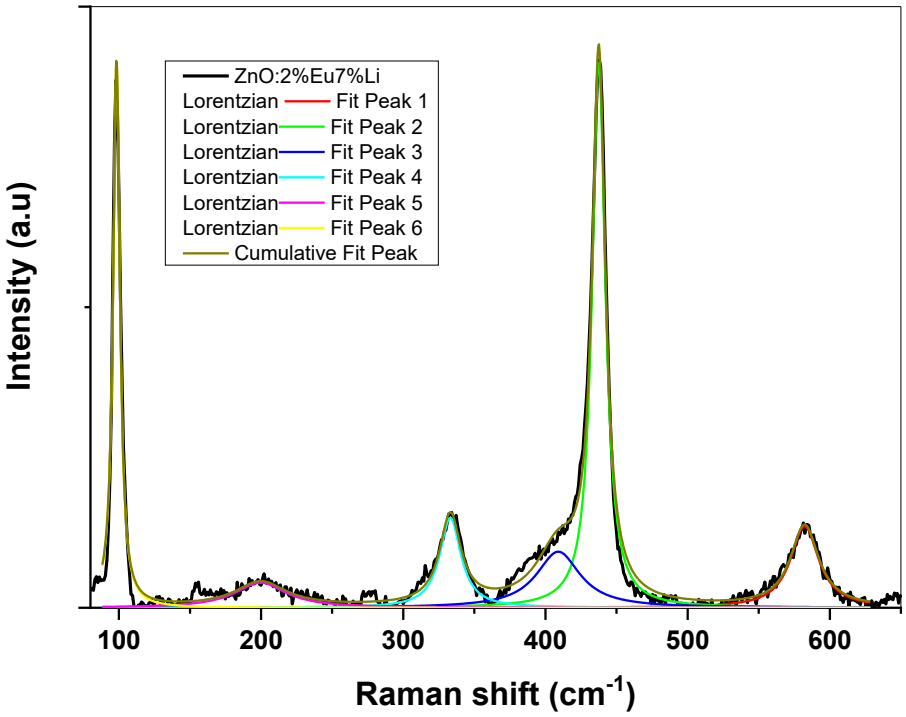

Figure III.9b: deconvolution of Raman spectra on the sum of Lorentzian functions

III.2.4. Photoluminescence Study

III.2.4.1. Steady photoluminescence spectroscopy (PL) study:

Photoluminescence (PL) spectroscopy was employed to investigate the optical properties of pure ZnO and ZnO nanoparticles co-doped with Eu^{3+} and Li^{+} ions. The measurements were performed using a monochromatized Xenon lamp as the excitation source, and the PL emission spectra were recorded at room temperature using excitation wavelengths of 258 nm and 465 nm.

The PL excitation spectrum of ZnO: 2 % Eu^{3+}, 7% Li^{+} for a fixed wavelength at 610 nm ($^5D_0 \rightarrow {}^7F_2$ transition) are displayed in figure10

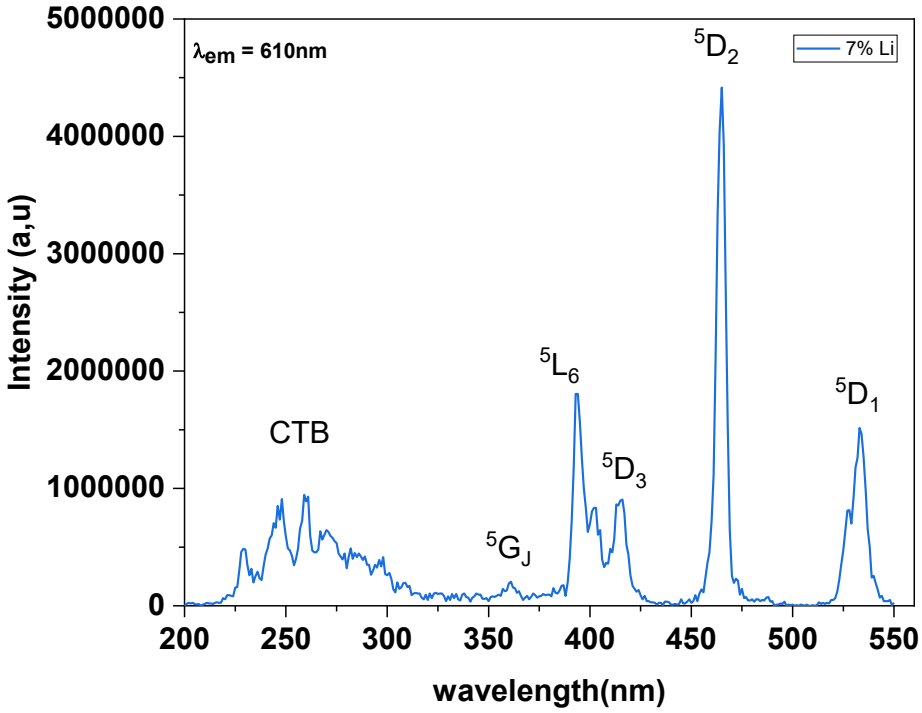

Figure III.10: Room temperature PL excitation spectra of ZnO: 2%Eu^{3+} 7% Li^{+} for 610 nm emission

All samples exhibit the same sharp peaks, between 350 nm and 550 mm, corresponding to the excitation of Eu^{3+} ions in ZnO indicated in the figure. Furthermore, it can be seen clearly that the excitation spectrum shows a broad band situated around 258 nm. This band is assigned to the charge transfer (CT) process from O^{2-} -2p state to Eu^{3+}- 4f state. The same band has been reported by several authors; Pal et al. in Eu^{3+} doped zinc oxide nanorods prepared by precipitation method (11). Stojadinovi´c et al (12) in ZnO: Eu^{3+} synthesized by the PEO with the addition of Eu_2O_3 to the basic electrolyte. Hasabeldaim et al (10) have reported CT band in spin-coated ZnO films doped Eu^{3+} at 288 nm, contrariwise same author (13) reported this band at 250 nm in ZnO: Eu^{3+} was synthesized via the combustion method.

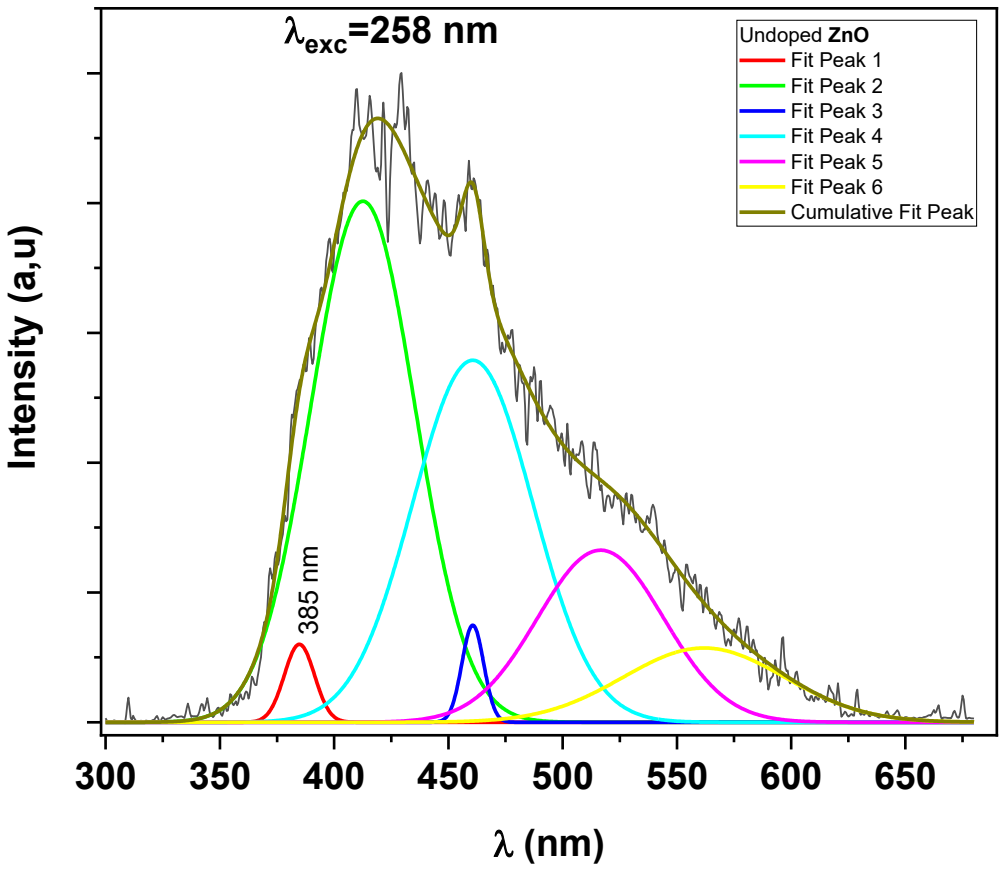

Figure III.11: Deconvolution of the room temperature emission spectrum of pure ZnO nanoparticles excited at 258 nm.

In addition, unknown origin narrow peaks convoluted with the charge transfer band were observed and further investigations should be performed to highlight their origin. Also, from the excitation spectrum one can see that all samples present the maximum excitation efficiency at $^5D_2$ energy level. The room temperature photoluminescence emission spectrum of pure ZnO powder, measured under 258 nm wavelength, was displayed in figure11.

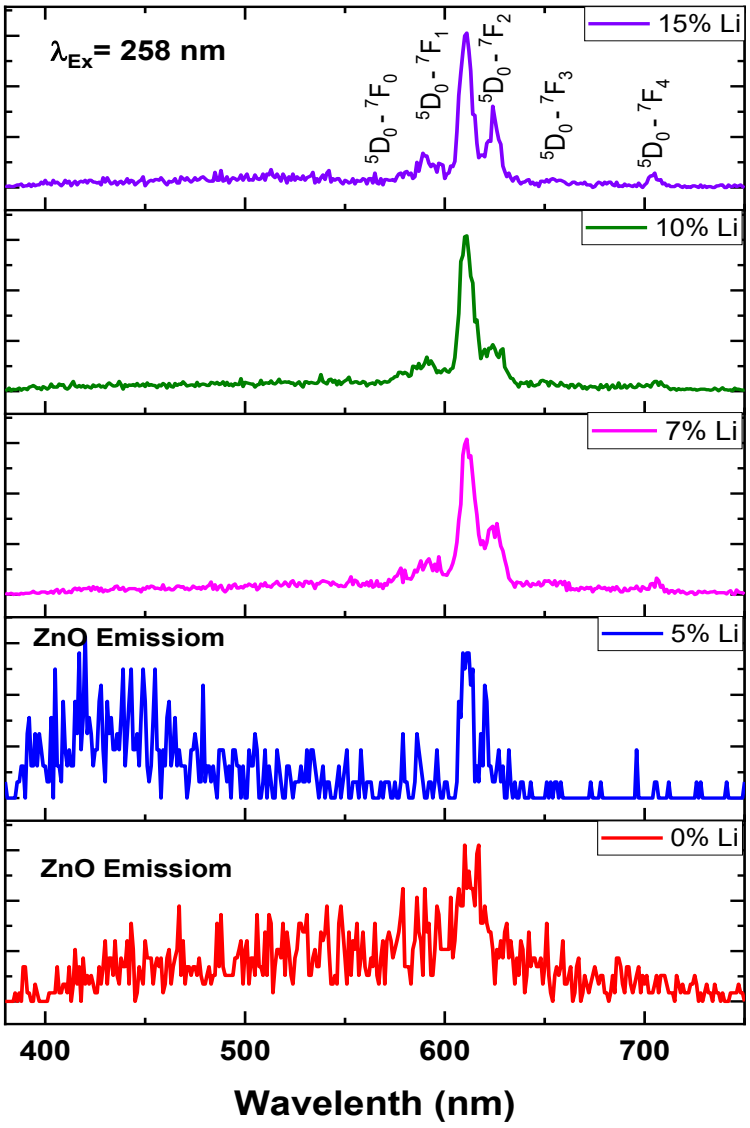

Figure III.12a: Room temperature emission spectra of ZnO: 2% Eu, x%Li (x= 0, 5, 7, 10 and 15 %) under 258 nm excitation wavelength

The broad visible emission spectrum of ZnO was well adjusted to six Gaussian functions indicating the presence of superposition of multiple emission positions(14). Generally, as it is known until now, pure ZnO exhibits emission in two regions. The first in UV, associated with a minor ultraviolet emission at 385 nm is related to excitonic recombination of the ZnO transition and visible emission associated with defects. In most cases, pure ZnO has six kinds of defects, namely: Oxygen vacancies (V_O), Oxygen interstitials (O_i), Oxygen antisites (Zn_O), zinc vacancies (V_{zn}), zinc interstitials

(Zn_i), zinc antisites (O_{zn}) (15), (16) The emission spectrum (figure11) of undoped ZnO presents the same features as reported in the literature. It is important to note that the positions of these defects depend on the synthesis method.

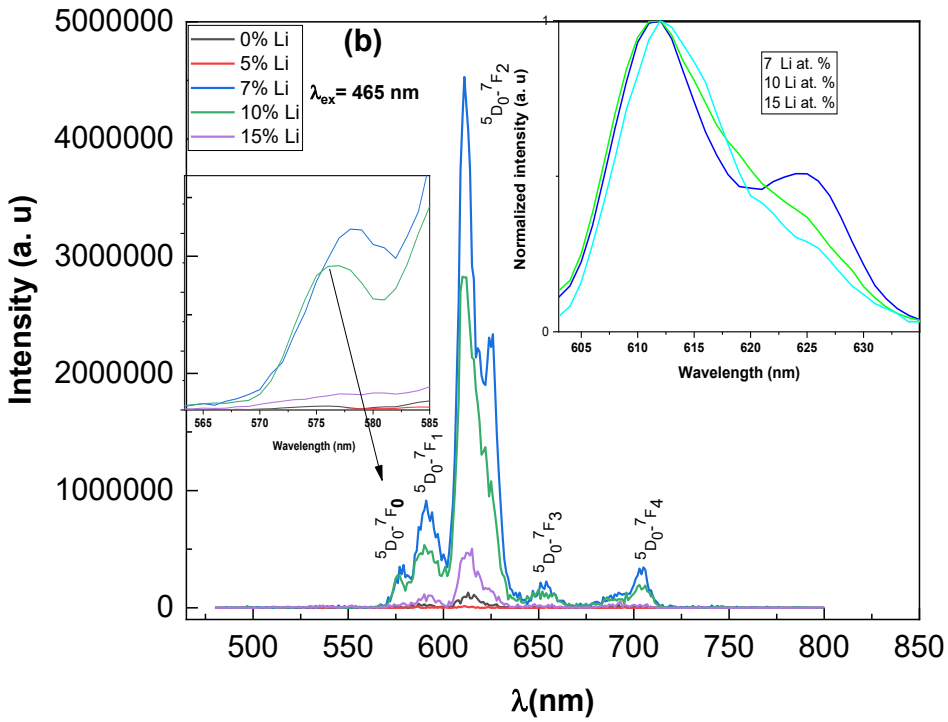

Figure III.12b: Room temperature emission spectra of ZnO: 2% Eu, x %Li (x= 0, 5, 7, 10 and 15 %) under 465 nm wavelength

The room temperature emission spectra of ZnO: Eu and Li co-doped ZnO: Eu were recorded for two excitation wavelengths, namely 258 nm (corresponding to charge transfer band (O-Eu) and 465 nm (corresponding to excitation at $^5D_2$ level of Eu^{3+}) and were shown in Figure 12 a and b. Under UV excitation (258 nm), all samples show two emission regions (Figure 12a). The first region between 370 nm and 570 nm, constitutes a broadband assigned to ZnO centers emissioms (excitonic and structural defects. The second one ranged from 570 nm to 750 nm and was constituted by some sharp peaks attributed to Eu^{3+} emission transitions namely $^5D_0 \rightarrow ^7F_J$ (J= 0, 1, 2, 3 and 4), indicated on the figure, in ZnO host material. In Figure 12 c, we display the ratio of the integrated emission of Eu^{3+} on that of ZnO (IEu3+/IZnO) as function of Li^+ content. In fact, this ratio is considered an indication of the energy transfer between ZnO

emissions centers and Eu^{3+} energy levels and vice versa. From Figure 12c, one can observe three regions depending on the ratio values with respect to $I_{Eu3+}/I_{ZnO} = 1$.

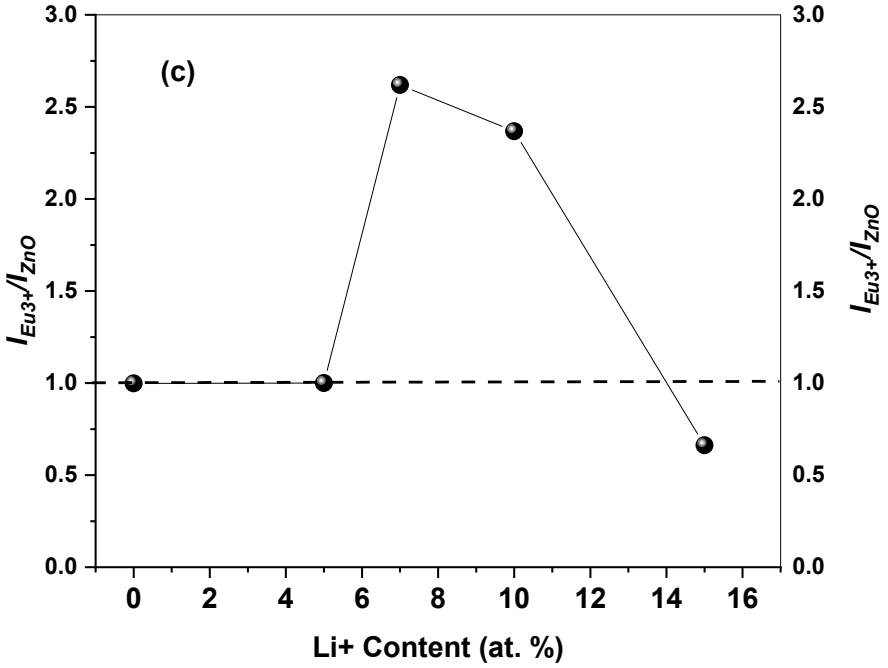

Figure III.12c: the variation of integrated emission of Eu^{3+} on that of ZnO ratio of the (IEu3+/IZnO) as function of Li^{+} content.

The first region between 0 and 5% in the IEu^{3+}= IZnO which we can think that half of the excitation energy is transferred to the Eu^{3+} ion. The second region is between 5 and 10%, in which IEu^{3+}/IZnO >1 indicates that energy is efficiently transferred from ZnO to Eu^{3+} energy levels. For 15% of Li+ content, IEu^{3+}/IZnO < 1 can indicate that Eu^{3+} emission is quenched by surface defects and/or transferred back to ZnO defects levels. One can conclude that the energy transfer can be tuned by codoping ZnO: Eu^{3+} by the Li^{+}. In Figure 12d**,** we show a schematic energy level diagram illustrating ZnO, defects, and Eu^{3+} ion emissions and the energy transfer mechanism between them when excited at wavelengths 258 nm and 465 nm.

Upon 465 nm excitation wavelength, Li co-doping ZnO: Eu^{3+} samples give rise to some number sharp peaks that correspond to the transitions $^5D_0 \rightarrow {}^7F_J$ (J= 0, 1, 2, 3 and 4) of Eu^{3+} ions in ZnO host nanomaterial (17).

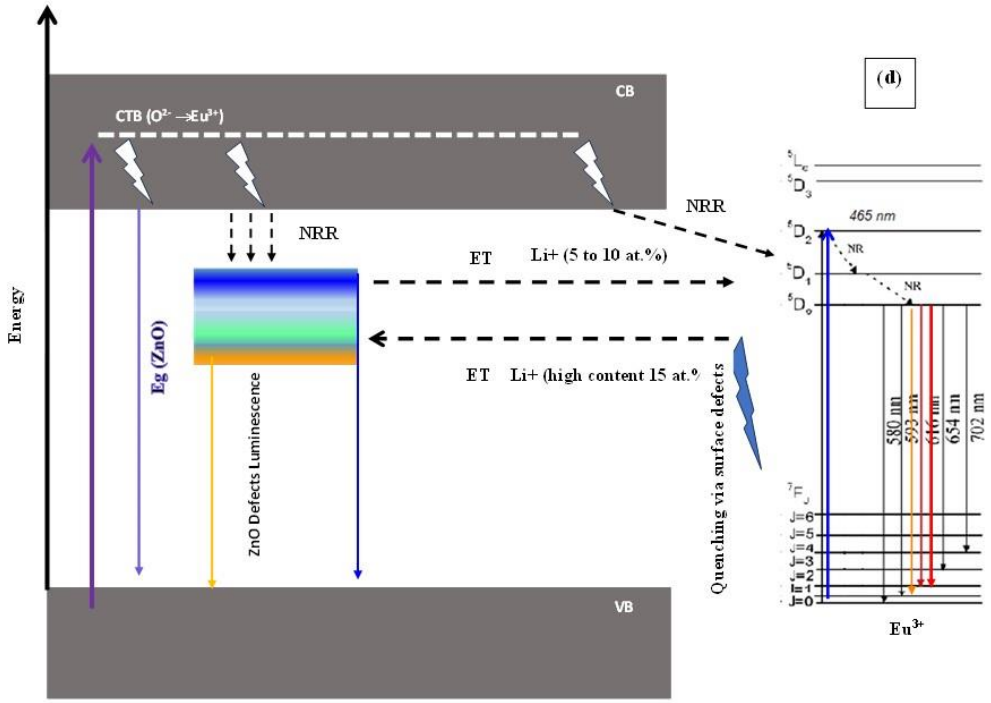

Figure III.12d: Schematic energy level diagram showing a proposal energy transfer mechanism from ZnO defects and Eu^{3+} ion every levels for 258 nm and 465 nm excitation wavelengths.

According to the emission spectra, the red forced Electric Dipole (ED) transition namely $^5D_0 \rightarrow ^7F_2$ centered at 610 nm, with the highest intensity and the orange magnetic dipole (MD) transitions $^5D_0 \rightarrow ^7F_1$ situated at 590 nm. The weak peaks observed at 650 nm are ascribed to $^5D_0 \rightarrow ^7F_3$. The intensity of the $^5D_0 \rightarrow ^7F_2$ transition of Eu^{3+} is much more intense than that of the $^5D_0 \rightarrow ^7F_1$ transition, which indicates that Eu^{3+} ions occupy a low-symmetry site without inversion center. It is worth noting that their emissions intensities and shapes depend on Li concentration and excitation wavelength. These modifications during the increase in co-doping by Li^+ ions can highlight the appearance of structural environment rearrangement around Eu^{3+} centers.

Figure 13 shows that, for Li^+ contents ranging from 0 to 5%, the Eu^{3+} emission intensity remains nearly identical for both excitation wavelengths. However, when the Li^+ concentration increases from 5 to 10%, samples excited via the $^5D_2$ energy level exhibit higher Eu^{3+} luminescence intensity than those excited through the charge transfer band (CTB). In contrast, the sample co-doped with 15% Li^+ displays stronger emission under CTB excitation than under $^5D_0$ level excitation. Furthermore, Figure 13 reveals

that, for each excitation wavelength, the Eu^{3+} emission intensity exhibits a distinct quenching behaviour depending on the Li^{+} content.

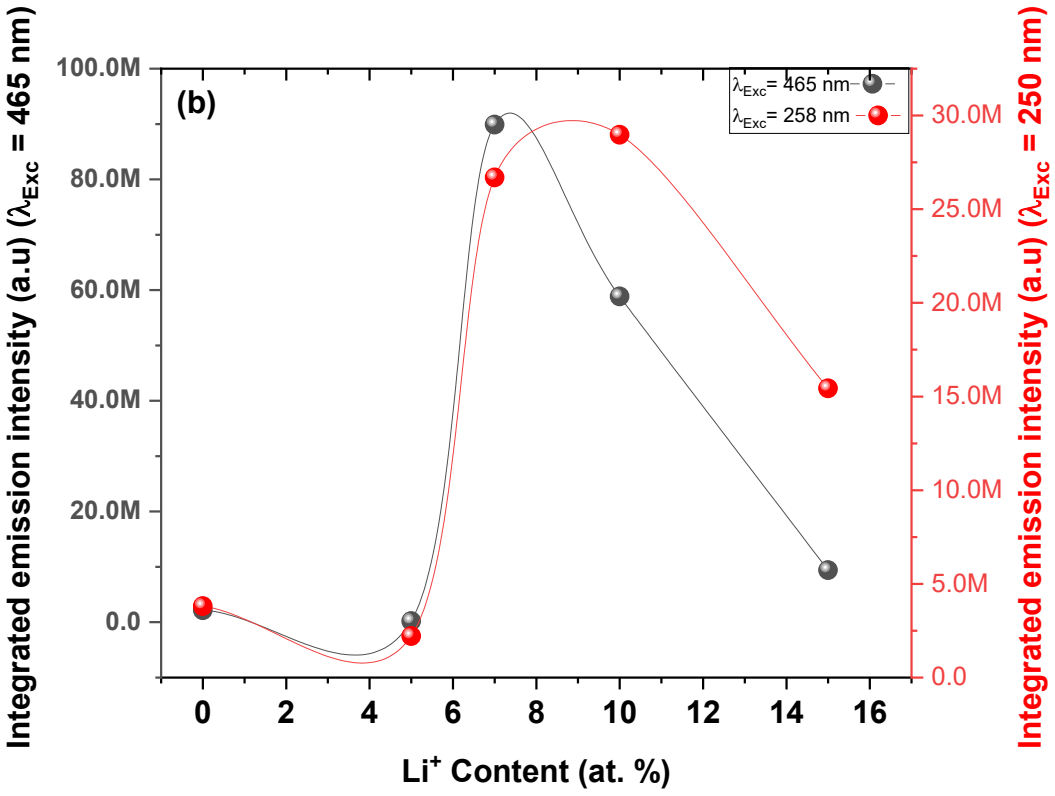

Figure III.13: Variation of integrated emission of Li-codoped ZnO: Eu^{3+} as function of Li content under 464 nm and 258 nm excitation wavelength.

Thereby, the enhancement and the degradation of emission intensity between Li^{+} co-doping can be related to the increasing or decreasing of the radiative relaxation rate as well as to the energy transfer efficiency from ZnO to Eu^{3+} in the case of UV excitation. In fact, there are several possible reasons that may lead to the intensity enhancement, depending on the presence of Li^{+} as a co-dopant, such as the change in the rearrangement of the structural environment around the Eu^{3+} ionic centers in the ZnO nanocrystal, the reduction in the density of surface defects, the charge compensation, and the creation of oxygen vacancies (18)

Furthermore, the magnetic dipole transition $^5D_0 \rightarrow ^7F_0$, theoretically forbidden according to the selection rules, appears in different intensities, especially in the samples co-doped with high Li content namely ZnO: 2%Eu^{3+}, x% Li (x= 7, 10, and 15). Generally, the observation of $^5D_0 \rightarrow ^7F_0$ transition is an indication that the Eu^{3+} ion occupies a site with C_{nv}, C_n, or C_s symmetry (19). In fact, $^5D_0 \rightarrow ^7F_0$ is related to the nephelauxetic effect, which is induced by the ion's first neighbors, thereby depending upon the sites of Eu^{3+} ions occupied at the inner lattice sites of the zinc oxide and its homogenous distribution, Apparently, Eu^{3+} ions are incorporated into zinc oxide and appears that Eu^{3+} ions can also be substituted for Zn. Therefore, in this work, there is a correlation between the emergence and severity of the intensity of the $^5D_0 \rightarrow ^7F_0$ transition with lithium concentration. One can think that adding more Li ions as a co-dopant possibly affected the position of Eu^{3+} ions in ZnO nanomaterial. Parchur et al. (20) found that in Li co-doping YPO_4: Eu^{3+}, $^5D_0 \rightarrow ^7F_0$ transition is observed for a high Li^+ co-doping and assigned to the fact that the crystal field of Eu^{3+} is influenced by the Li^+ ions, which occupy interstitial sites of YPO_4.

Furthermore, it is known that the MD transition $^5D_0 \rightarrow ^7F_1$ is assumed to be independent of the crystal field effects contrariwise, the ED transition $^5D_0 \rightarrow ^7F_2$ is strongly dependent on the local site symmetry and on the nature of the coordinating ligands (hypersensitive transition) of Eu^{3+} (21). On this basis, it is defined the asymmetry ratio parameter *R* as the ratio of the integrated intensities of the luminescence transitions of $^5D_0 \rightarrow ^7F_2$ on that of $^5D_0 \rightarrow ^7F_1$ transitions ($R = I(^5D_0 \rightarrow ^7F_2)/I(^5D_0 \rightarrow ^7F_1)$) obtained from emission spectra. This parameter can give information about the Eu^{3+} ion's local symmetry distortion in the host material. In Figure.14 a, we display the variation of the *R* parameter against Li concentration for the two-excitation wavelength 258 nm and 465 nm.

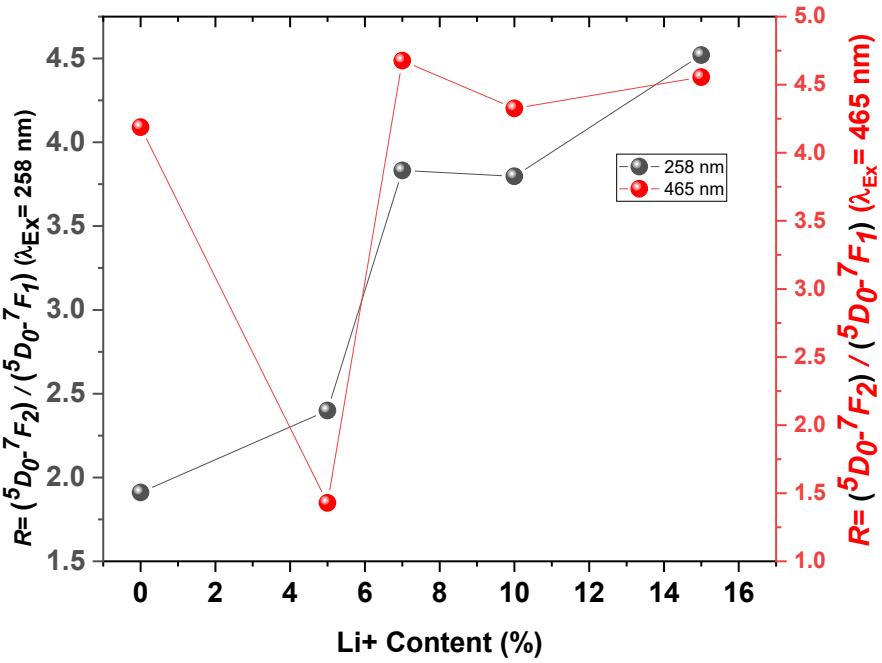

Figure III.14a: Asymmetry rations for Eu^{3+} in ZnO various Li^{+} content for excitation with 258 nm and 465 nm

One can see from the figure that for both excitation wavelengths the *R*-value is larger than one, indicating that the symmetry of the crystal field around Eu^{3+} does not have an inversion center. Likewise, it is observed that the variation of R depends on the excitation wavelength. For UV excitation (258 nm), *R* increases quasi-linear from 1.91 to 4.52 with Li content, on the other hand, for visible excitation (465 nm), *R* is quasi-constant around 4.5, except for 5%, concentration, it presents a minimum of 1.42. It is important to note that the crystallite size influence drastically the value of R for 465 nm excitation which is confirmed by their behaviors with Li^{+} content as shown in Figure 14b.

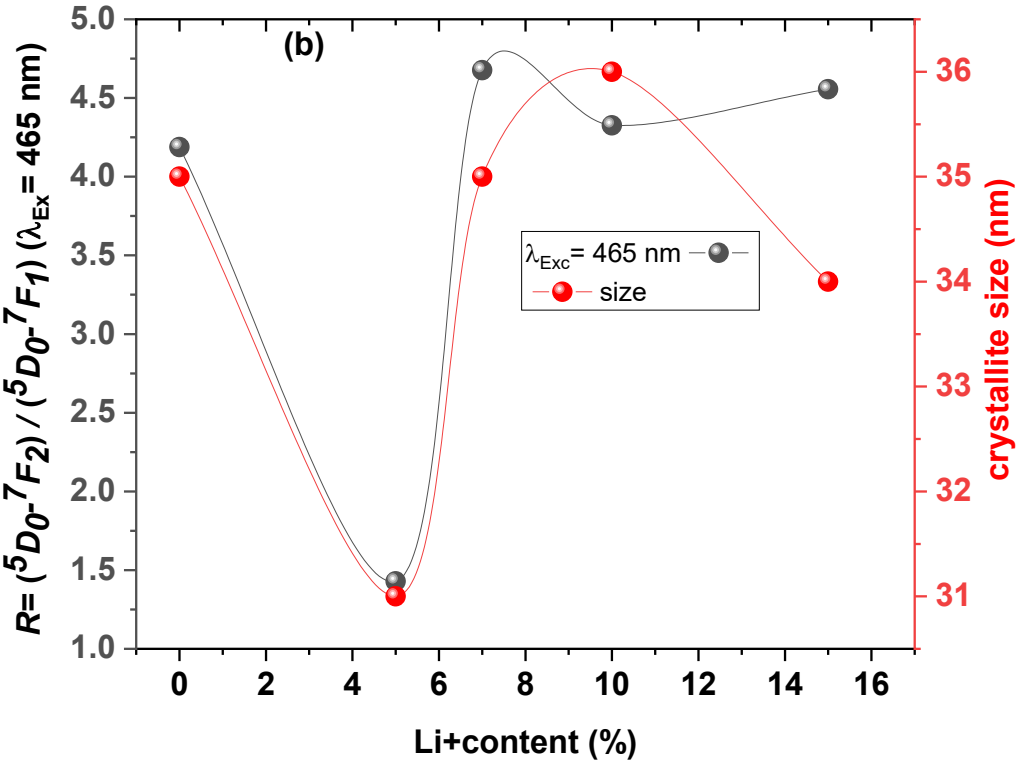

Figure III.14b: Asymmetry ratios of Eu^{3+} in ZnO as a function of Li^{+} content under 465 nm excitation, and their correlation with crystallite size

III.2.4.2. Decay time

The room-temperature emission decay curves were measured under both excitation 258 nm and 465 nm, monitoring the Eu^{3+} emission at a wavelength of 610 nm (Figure 15 a and b). The average or also called observed lifetime (τ_{Av}), (τ_{Ob}) of $^5D_0$ energy level of Eu^{3+} in ZnO was calculated using the following formula (13)

$$\tau_{Av} = \tau_{Ob} = \frac{\int It\, dt}{\int I\, dt} \qquad \text{..... III.12}$$

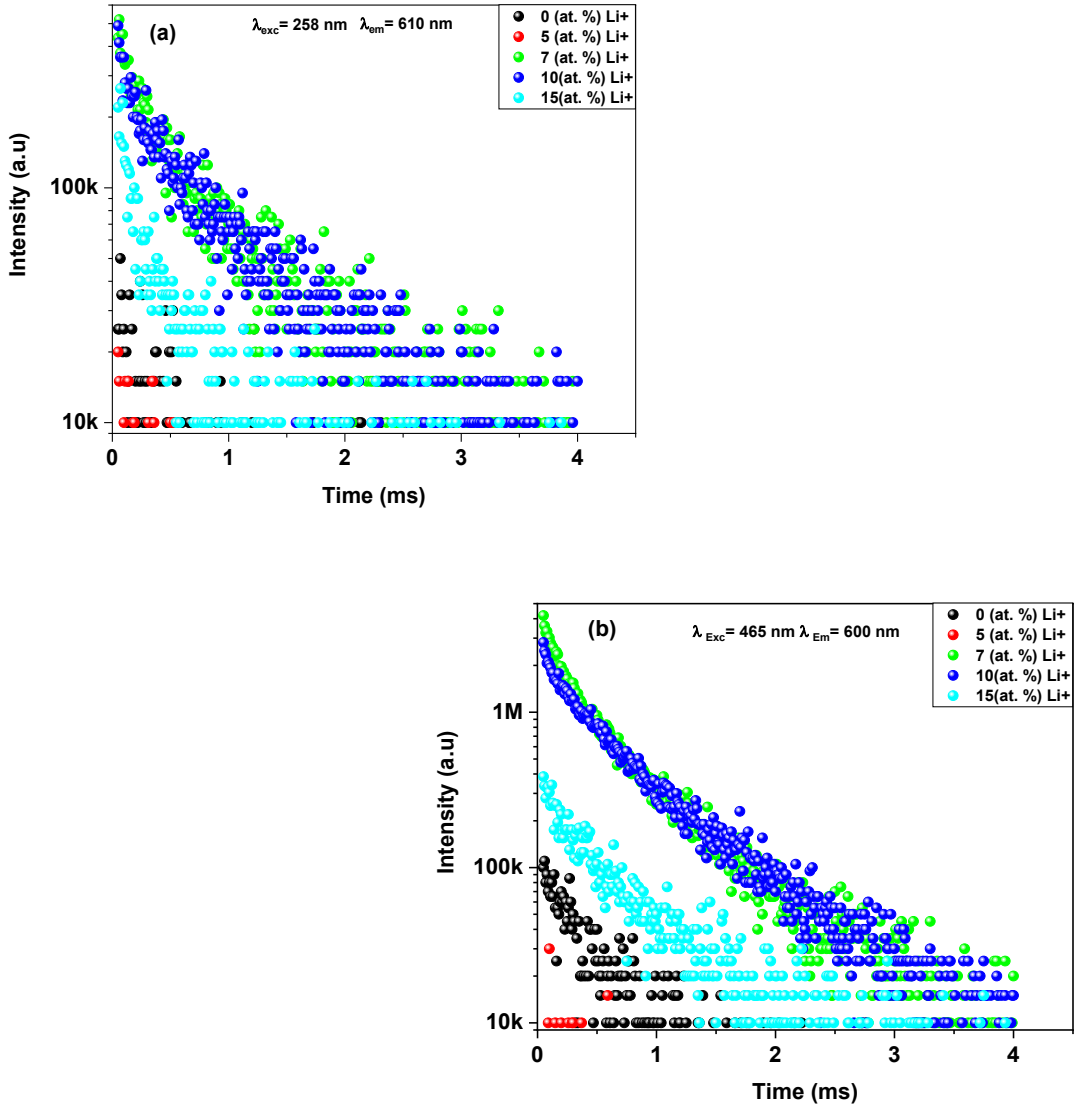

Figure III.15: Luminescence decay curves of $^5D_0 \rightarrow {}^7F_2$ transitions of different Li^+ content co-doped ZnO: Eu^{3+}: (a) under 258 nm excitation wavelength (b) under 465 nm wavelength

With *I* is the intensity of luminescence and *t* represents the time in milliseconds. The variation of $^5D_0$ energy level lifetime for both excitation wavelengths against Li^+ content was displayed in Figure.15c. One can observe that roughly the decay time for 258 nm excitation wavelength evolves in an opposite way to that of 465 nm as function of Li^+ content except from 7 to 10%, where they increase in the same way. For both excitation wavelengths, the $^5D_0$ energy level presents short lifetime values ranging from 0.55 to 0.87 ms. Moreover, the increase in the lifetime of $^5D_0$ between 5% and 10 % under UV excitation wavelength (258 nm) can confirm the energy transfer from ZnO to Eu^{3+},

which is in agreement the above with results. The decrease in the lifetime between 10% and 15% can be attributed to the reverse transfer of Eu^{3+} to ZnO and/or the increase in surface defect concentration as quenchers. Jiu et al (22) found that for Ca^{2+} co-doping YVO_4: Eu^{3+}, the lifetime of Eu^{3+} increases with increasing Ca^{2+} content, thus confirming the energy transfer was successfully transferred from the sensitizer to the activator (Eu^{3+}). It is worthing to note that the found $^5D_0$ lifetime values of Eu^{3+} in ZnO powders in the literature can be very long, long, short, and very short depending on the synthesized route

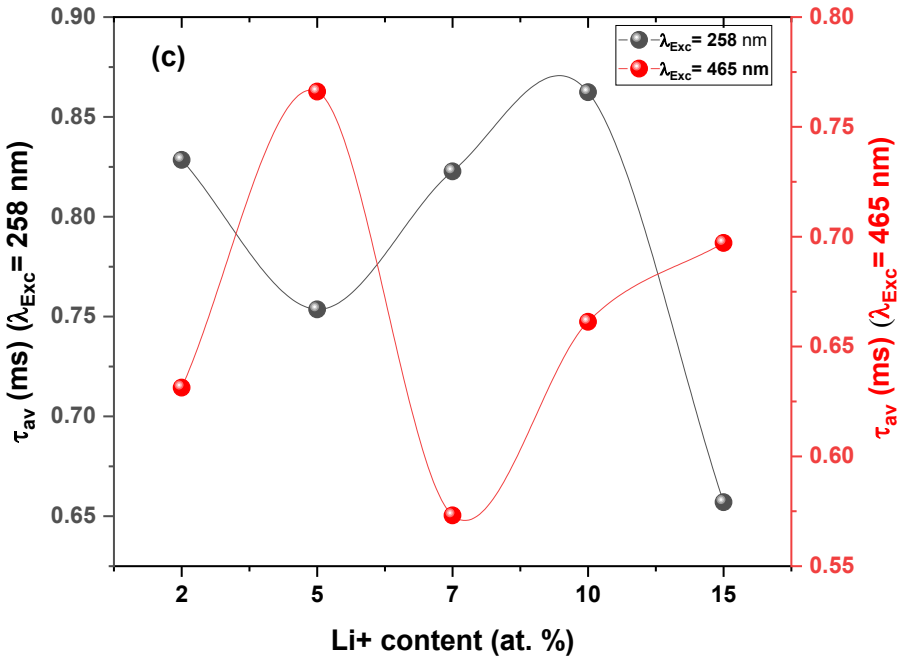

Figure III.16: Luminescence decay curves of $^5D_0 \rightarrow {}^7F_2$ transitions of different Li^+ content co-doped ZnO: Eu^{3+}: (c) variation of average $^5D_0$ lifetime under 258 nm and 465 nm excitation wavelengths

In Figure.15d, we plot the variation of the average $^5D_0$ lifetime as well as I_{Eu3+}/I_{ZnO} ratio, under 258 nm excitation wavelength. One can observe that they exhibit the same behavior, which can Fang et al.(23) found 34 ms in ZnO:1.5 % Eu^{3+} and Stojadinovi´et al ,found 1.20 ms ZnO:1.91% Eu^{3+}. On the other side, Hasabeldaim et al, found a short lifetime of 0.56 ms in ZnO:1% Eu^{3+} and a very short lifetime was found by Bouslama et al , as 0.173 ms ZnO: 1% Eu^{3+}.confirm that for Li content from 5 to 10%, the excited

energy transfer efficiently from ZnO defect centers to the doped Eu^{3+} ions are improved.

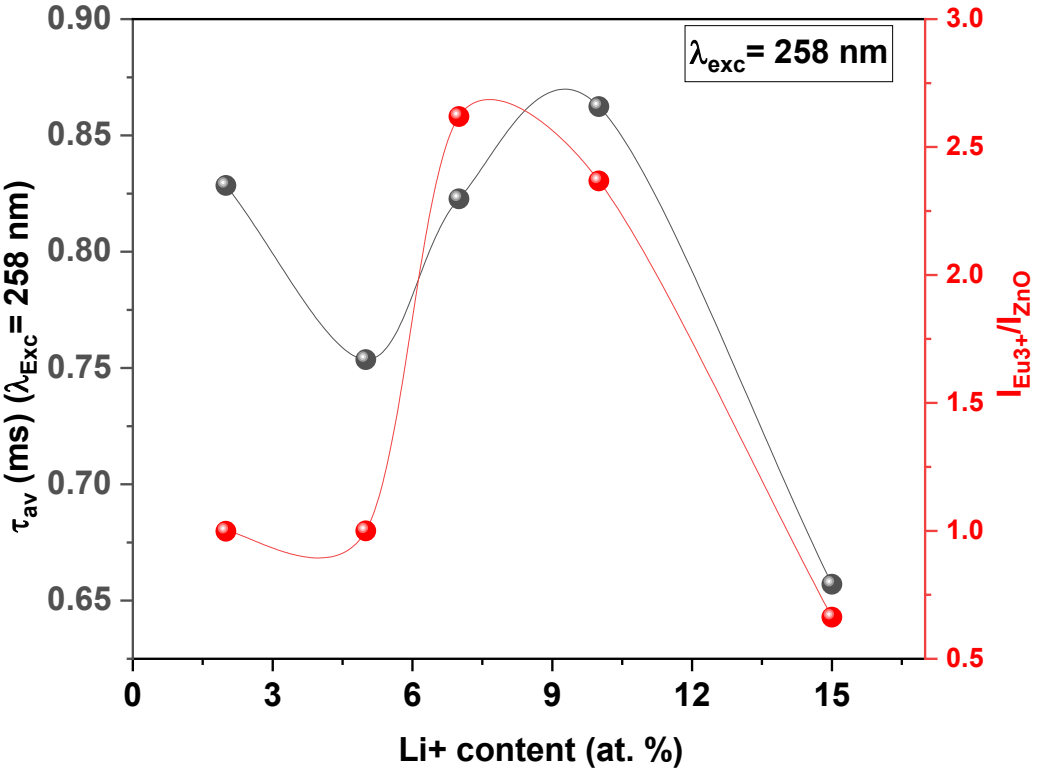

Figure III.17: Luminescence decay curves of $^5D_0 \rightarrow {}^7F_2$ transitions of different Li^+ content co-doped ZnO: Eu^{3+}: (d) variation of average $^5D_0$ lifetime under as well as I_{Eu3+}/I_{ZnO} ratio under 258 nm excitation wavelength

III.2.5. Judd-Ofelt parametrization from Eu^{3+} emission spectra

More investigation and details of the spectroscopic properties of Li^+-co-doped ZnO: Eu^{3+} nanostructures were performed through Judd-Ofelt (JO) analysis. In fact, for compounds activated by trivalent europium ions, the JO parameters can be obtained using the emission spectra.(24). This is because, in the $4f^6$ electronic configuration, many reduced matrix elements of the unitary tensor operators between the J manifolds are zero. JO parameters Ω_λ (λ= 2, 4 and 6), radiative transition probabilities (A (J, J')), branching ratios, radiative lifetime, emission cross-section (σ) of Li-co-doped ZnO: Eu^{3+} were calculated using JOES application software (25). In

fact, generally the determination of the three J-O intensity parameters namely Ω_λ (λ= 2, 4 and 6) supply more information on the structural environment, symmetry, and covalency related to Eu^{3+} ion in Li-co-doped ZnO host lattice (26). It is known that Ω_2 is a sensitive parameter to the activator symmetry, local structure, and covalency of the metal-ligand bond**.** While Ω_4 and Ω_6 are sensitive to some macroscopic parameters such as dielectric constant, matrix stiffness, and viscosity (27). In the following study, the JO parameters and all derived quantities were determined from the emission spectra of europium in Li co-doped ZnO: Eu^{3+}. Knowing that the pure magnetic dipole transition $^5D_0 \rightarrow {}^7F_1$ has dipole strength independent on the host matrix (9.6×10^{-42} $esu^2.cm^2$) and using the calculated reduced matrix elements corresponding to $^5D_0 \rightarrow {}^7F_{2,4,6}$ transitions namely $U_2 = 0.0032$, $U_4 = 0.0023$, $U_6 = 0.0002$, respectively the JO intensity parameters and the derived quantities were obtained. The data from JO calculation of intensity parameters and derived quantities were performed using JOES application software (25) and presented in Table 3.

In the present work, because the $^5D_0 \rightarrow {}^7F_6$ transition was not observed in the emission spectra, the Ω_6 intensity parameter was not determined. The refractive index values were taken as 2.0034 (28). A perusal of table 3, reveals that Li 5% sample presents the lowest Ω_2 and follows the same behavior as that of asymmetry ratio parameter *R* for 465 nm excitation wavelength (see figure). In fact, it has been established that the more the Eu-O chemical bond is covalent, the more $^5D_0 \rightarrow {}^7F_2$ transition intensity is enhanced as observed (29) **.**

One can think that this smaller Ω_2 value is related to the fact that Li^+ ion replaces Zn^{2+} ions and consequently Eu^{3+} ion will be in a more ionic site. Otherwise, a larger Ω_2 value can be obtained if the Eu^{3+} ions are in a more covalent site and this proof that Li^+ ions are situated in an interstitial site (30). Also, the relatively higher Ω_2 values, observed for the sample doped at 7% Li, can be associated with lowest symmetry and stronger polarizability of oxygen ions around Eu^{3+} ions. As $\Omega_2 > \Omega_4$ confirms that Eu^{3+} occupy low site symmetry with higher covalency of the Eu^{3+}– O^{2-} bond (31). One can observe that the sample with 5% presents the highest value of Ω4, which can be related to the high substantial rigidity of the ZnO host lattice and/or to the decreasing of the electron density on the ligand decreases under Li doping (32).

Table III.3: JO parameters and derived quantities calculated for ZnO: Eu^{3+} samples with different Li co-doping contents.

Li Content (at. %)	0	5	7	10	15
$\Omega_2 \times 10^{-20}$ [cm²]	7.47	2.55	8.22	8.11	7.96
$\Omega_4 \times 10^{-20}$ [cm²]	2.37	3.64	1.57	1.61	1.85
β_{exp} ($^5D_0 \rightarrow {}^7F_1$)	0.14	0.30	0.13	0.13	0.13
β_{exp} ($^5D_0 \rightarrow {}^7F_2$)	0.67	0.50	0.72	0.70	0.70
β_{exp} ($^5D_0 \rightarrow {}^7F_4$)	0.09	0.03	0.05	0.06	0.07
β_{th} ($^5D_0 \rightarrow {}^7F_1$)	0.14	0.35	0.14	0.14	0.14
β_{th} ($^5D_0 \rightarrow {}^7F_2$)	0.73	0.60	0.78	0.78	0.76
β_{th} ($^5D_0 \rightarrow {}^7F_4$)	0.11	0.04	0.07	0.07	0.08
A_R [s^{-1}]	788.81	330.95	811.39	807,19	806.65
A_{NR} [s^{-1}]	795.24	974.40	933.31	705.04	627.69
A_{tot} [s^{-1}]	1584.05	1305,35	1744,7	1512,23	1434,34
τ_{th} [ms]	1.189	2.617	1.170	1.150	1.169
τ_{calc} [ms]	1.267	3.021	1.232	1.238	1.239
τ_{obs} [ms]	0.631	0.766	0.573	0.661	0.697
$\sigma \times 10^{-22}$ ($^5D_0 \rightarrow {}^7F_1$) [cm²]	1.744	2.843	0.897	0.843	2.650
$\sigma \times 10^{-22}$ ($^5D_0 \rightarrow {}^7F_2$) [cm²]	8.534	5.588	5.777	5.702	2.650
$\sigma \times 10^{-22}$ ($^5D_0 \rightarrow {}^7F_4$) [cm²]	2.812	2.726	0.783	0.685	15.861
η (%)	53.06	29.26	48.94	57.45	59.58

It was found that Li 5% sample presents the weakest quantum efficiency, with the highest radiative lifetime compared to the others. Also, coping with Li ions reduces the non-radiative transition rates (A_{NR}). The experimental and theoretical branching ratios (β_{exp} and β_{th}, respectively) are found to be very close. Also, the branching ratios of $^5D_0 \rightarrow {}^7F_2$ transition for all phosphors were over 50% indicating a potential laser emission (33). The PL quantum efficiency (η) was found to range from 29.26% to 59.58% with the best efficiency recorded for the sample with a doping concentration of 15% Li.

III.2.5.1. Local field effects on the radiative lifetimes of Eu^{3+} in ZnO: Eu^{3+}, Li^{+} host nanomaterials

The modification of the radiative lifetime *(τ_{Rad})* of Li^{+} co-doped ZnO: Eu^{3+} nanocrystalline powders, as shown in table 3, is caused by local-field effects and was addressed in several theoretical and experimental works in the literature (34). It is wordsworth to note that nanocrystalline materials can exhibit optical properties very different from those of bulk materials. Therefore, given their growing importance in current photonics, a good characterization and understanding of the effect of the local field on their optical properties is required. Local field effect has been considered as an important asset to improve the optical properties of nanocrystalline powders and thus it has attracted great attention. Also, different theoretical models have been performed to predict the dependence of the radiative lifetimes on the refractive index, for rare earth ions notably Eu^{3+}. However, it is established that the differences in the behaviors of radiative lifetimes as a function of the refractive index depend on the chosen model and change according to the situations (35), which are based on the fact that the only contribution to the spontaneous radiative lifetime comes from the electric dipole moment (36). Indeed, since the nano-crystallites (NCs) occupy only a small fraction of the total volume, the effective refractive n_{eff} index considers these nanoparticles surrounded by the medium with refractive index n_{med}. One may evaluate an effective refraction index as $n_{eff}(x) = xn_{bulk} + (1-x)n_{med}$ (37). Where *x* presents the "filling factor", indicating the fraction of space of the medium is occupied by the Nano crystallites *(volume fraction = volume of NCs/volume of medium)* and has physical meaning if $0 < x < 1$.

The spontaneous radiative emission rate A_{if} of electric dipole transition from an initial state *i* to a final state *f* (in our case $^5D_0 \rightarrow {}^7F_2$) can be expressed as (38):

$$A_{if} = \frac{1}{\tau_{rad}} = \frac{64\pi^4}{3h} \times \left[(L_{VC,RC})_{Bulk,\ Nano}\right] \times \nu_{if}^3 \times \left|\vec{\mu}_{if}\right|^2 \qquad \ldots \textbf{III.13}$$

Here, $\vec{\mu}_{if}$ is the electric dipole moment($-e\,\vec{r}_{if}$) between initial state *i* ($^5D_0$) to a final state *f* ($^7F_2$), ν_{if} is the emission wave number and $[L_{VC,\,RC})_{Bulk,\,Nano}]$ is an enhancement factor due to the dielectric medium in bulk (B) and nanomaterials (Nano), which equals

$n[(n^2 + 2)/3]^2$ for the virtual-cavity (VC)- and $n[3n^2/(2n^2 + 1)]^2$ for the real-cavity (RC) models (39). With the following rough assumptions: the final states *f* ($^7F_2$), have the same energy, the total spontaneous emission, the radial integral $\left|\vec{\mu}_{if}\right|^2$ is considered constant for both LuAG bulk and nanomaterial, the relationship between the refractive index for each sample as follows (40):

For virtual-cavity model

$$\left(\frac{\tau_B}{\tau_{nano}}\right)_{Exp} \times ({n_B}^2 + 2)^2 \times n_B = n_{nano}^5 + 4n_{nano}^3 + 4n_{nano} \quad \ldots \textbf{III.14}$$

$$\left(\frac{\tau_B}{\tau_{nano}}\right)_{Exp} \times \frac{(2{n_B}^2+1)^2}{{n_B}^5} = \frac{1}{n_{nano}^5} + \frac{4}{n_{nano}^3} + \frac{4}{n_{nano}} \quad \ldots \textbf{III.15}$$

It is important to point out that to the best of our knowledge the literature there are no reports concerning the radiative decay time (τ_B) of $^5D_0 \rightarrow {}^7F_2$ of Eu^{3+} doped bulk ZnO. One can estimate τ_B by using equations 1 and 2 for virtual-cavity and real-cavity models. One can vary n_{nano} from one to n_{ZnO} value as ($1 = n_{air} < n_{nano} \leq n_{Bulk} = n_B = 2.0034$) and plots the evolution of τ_B for the real-cavity (RC) models as function of n_{nano}. In Figure.16, we present the variation τ_B versus n_{nano}. The interpolation for $n_B = 2.0034$ gives τ_B values for each sample. It can be observed that sample with 5% Li presents larger τ_B values than that of other samples for both models. In addition, for the real cavity model, it was found that that τ_B = 3.00449 ms for 5% and 1.25 ms for the other samples and for virtual model τ_B = 6.042 ms for 5% and 2.53 ms for the other samples.

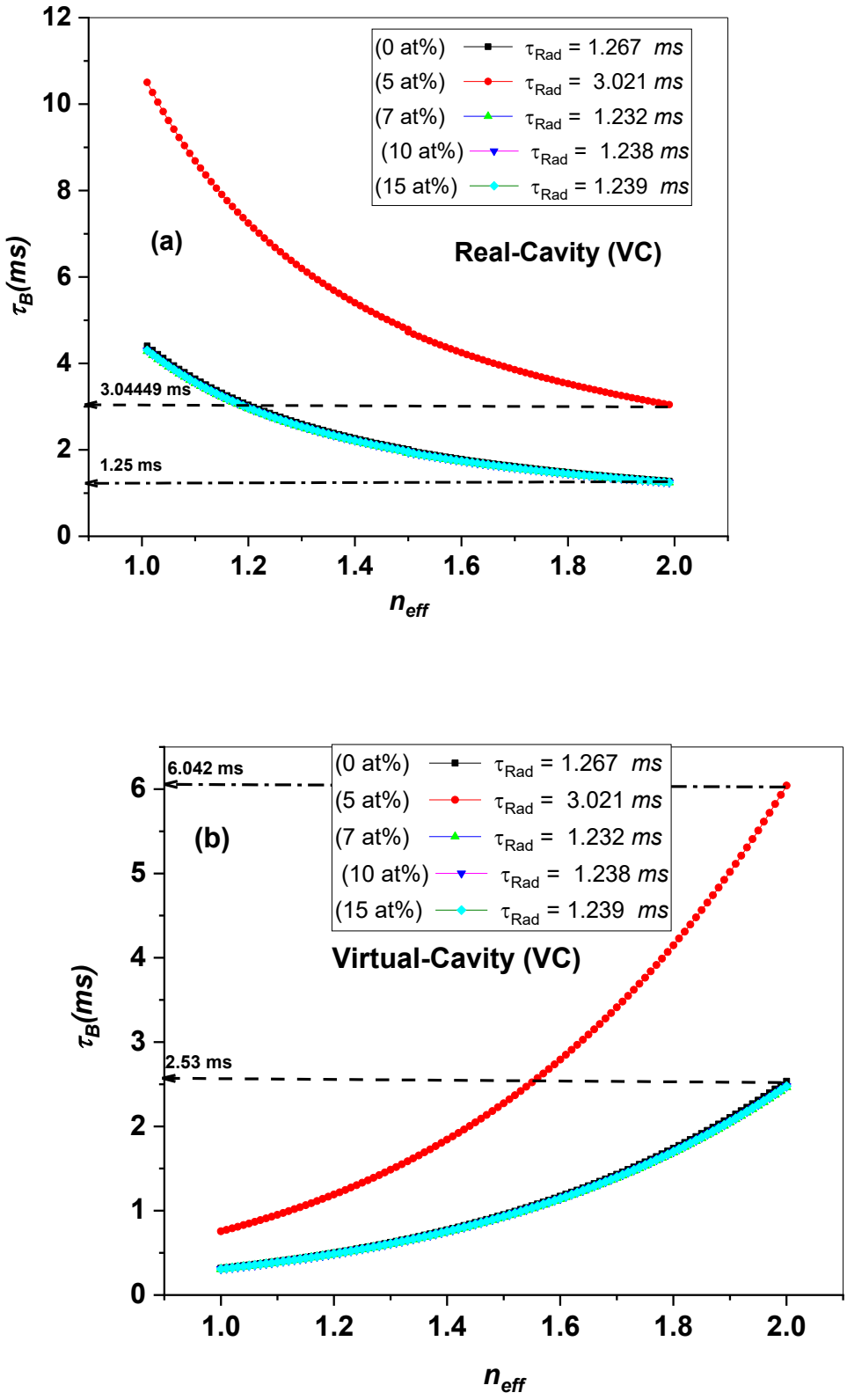

Figure III.18: the variation τ_B versus n_{nano}, (a) for real cavity model (b) virtual cavity model

III.2.5.2. CIE coordinates

To determine the photometric quantities of ZnO:2%Eu^{3+}, x%Li^{+} phosphors, the Commission Internationale de l'Eclairage (CIE) 1931 and 1964 chromaticity diagrams have been employed. The photometric coordinates are computed from PL emission spectra and are represented in table 4. The chromaticity color coordinates for (CIE1931: x, y; CIE1976: u', v') and correlated color temperature (CCT) of different phosphors with different Li content are presented in the color space as depicted in Figure.17a and b, respectively. One can observe that all color coordinate positions are located in the red region of color space. The color coordinates according to CIE1931 (Table 4.) for ZnO: 2%Eu^{3+}, x%Li^{+} with (x = 0 %, and 15%) were found to match with those from Piquette et al.

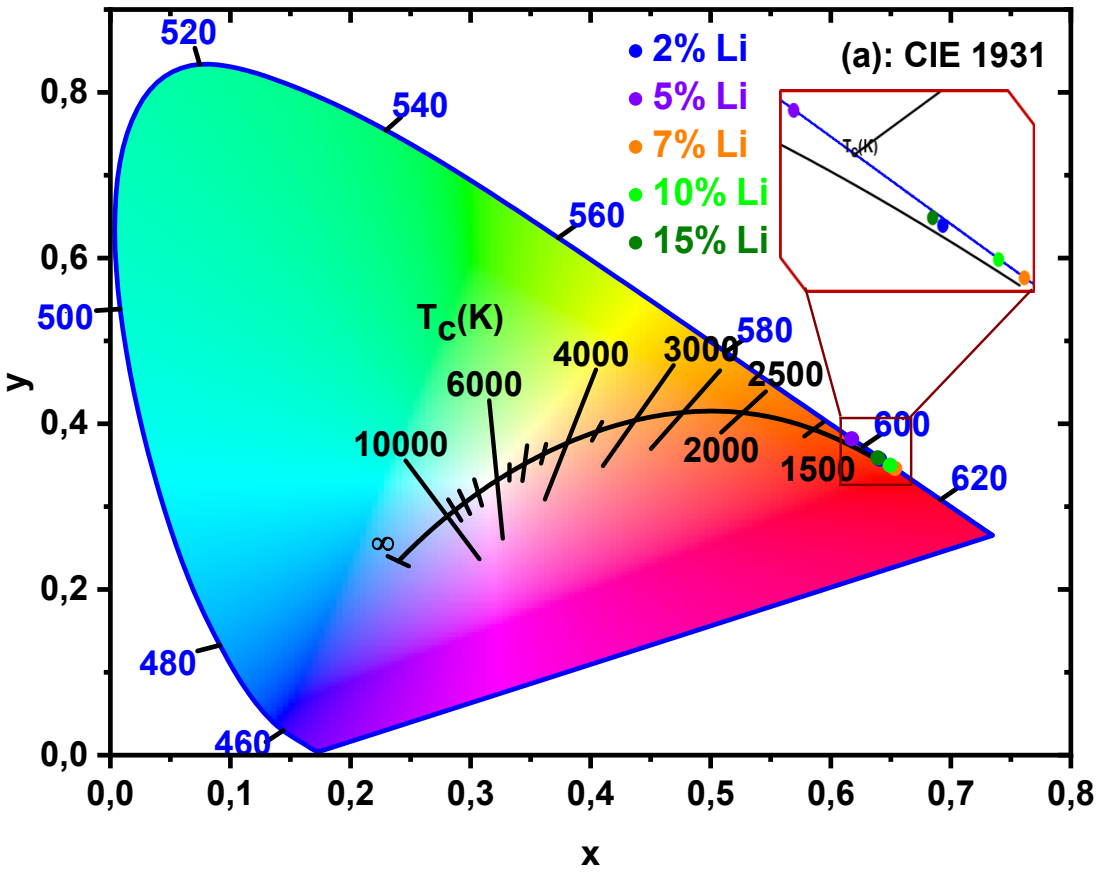

Figure III.19: Chromaticity diagrams according to (a) CIE1931.

(41)for narrowband lamp phosphor (Y_2O_3:Eu^{3+}) and broadband (Sr, Ba, Ca)$_2Si_5N_8$:Eu^{2+} LED phosphor. For samples prepared with (x = 7%, and 10%), CIE1931, color coordinates are close to those of the National Television System Committee (NTSC) standard for red phosphors (0.67, 0.33) . The sample prepared

with (x = 5%) was found to have CIE1931 color coordinates of red phosphorescent LEDs (0.61, 0.38) using the RD61 dopant useful for LCD backlight and display applications

The color coordinates according to CIE1976 for ZnO: 2%Eu^{3+}, x Li^{+} with (x = 0 %, as well as 15%), (x = 5%), and (x = 7%, as well as 10%) samples (table 5) were found to be close to mean chromaticities and 95th percentile limits of the red color for smartphones of iPhone 5, iPhone 4s, and Samsung s4, respectively. These findings offer the promise of usage of the prepared phosphors as red-emitting luminescent materials for display applications. The quality of the light source was investigated in terms of kelvin (K) using correlated color temperature (CCT) evaluated from chromaticity coordinates. The values of CCT were calculated using McCamy's empirical formula. The black body deviation D_{uv} which measures the distance to the Planckian locus, associated with each CCT and the respective color purity (CP) were estimated (table 5).

Table III.4: Photometric parameters of ZnO: Eu^{3+} samples with different Li co-doping contents.

Li content at.%	*CIE 1931*		*CCT (K)*	*D_{uv}*	*Color purity (CP) (%)*	*CIE 1976*	
	x	*y*				*u´*	*v´*
0	*0.644*	*0.355*	*2370*	*0.0779*	*90.94*	*0.431*	*0.535*
5	*0.621*	*0.379*	*1849*	*0.0348*	*86.97*	*0.394*	*0.541*
7	*0.656*	*0.343*	*2359*	*0.1092*	*95.63*	*0.452*	*0.532*
10	*0.652*	*0.347*	*2669*	*0.0981*	*94.57*	*0.445*	*0.533*
15	*0.642*	*0.357*	*2306*	*0.0733*	*89.18*	*0.428*	*0.535*

The calculated CCT values under different Li^{+} contents were found to vary within the range of 1849 K to 2669 K which depicts the warm nature of the emitted light (< 3200 K). Thus, the prepared ZnO:2% Eu, x% Li^{+} phosphors emit a soft light in a range similar to that of a candle (CCT = 1900 K) (42) for (x = 5%), of incandescent sources in between for (x = 2, 7, and 15 %), and close to that of a Halogen bulb (CCT = 2800 K) (43), particularly for (x = 10%). This kind of light source is best suitable for comfortable environments such as residential lighting, restaurants, etc . Calculated D_{uv} values were found to be small and positive for all ZnO co-doped samples (table 5) depicting that

the color points are located in the above vicinity of the Planckian locus (table 4) . The values of color purity (CP) for all ZnO codoped samples exceed 86% (table 4) This can be attributed to the emitted light which is focused on a narrow range of wavelengths in the red region, which made the location of the chromaticity coordinates in the extreme border of the CIE diagrams (Inset of Fig.17) of the red color standard (0.67, 0.33). The calculated photometric properties make of Eu^{3+} and Li^{+} codoped ZnO phosphors potential candidates for optoelectronic applications, particularly in display and lighting.

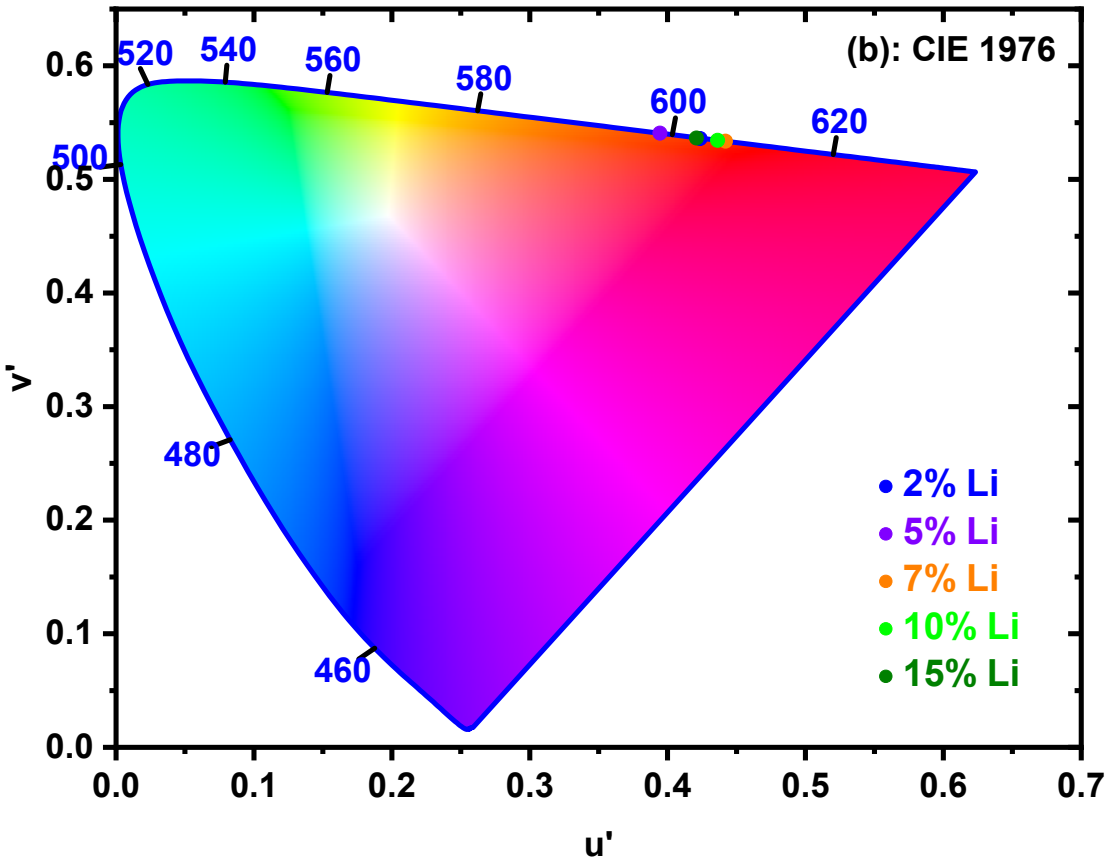

Figure III.20: Chromaticity diagrams according to (b) CIE1976 of ZnO: 2% Eu3+, x% Li+ (x = 0, 5, 7, 10, 15%) phosphors excited by 465 nm.

CHAPITRE IV

Study of the Structural and Optical Properties of ZnO Thin Films Co-Doped with Eu^{3+} and Li^{+}

IV.1. Introduction

ZnO Thin films and their doped derivatives are of great interest due to their wide range of applications in photonic, optoelectronic, and sensing devices [1-5]. Compared to powders, thin films enable customization of structural and optical properties through controlled growth conditions and doping strategies and provide greater flexibility with device architectures. To tune the material's structural and luminous behavior, co-doping ZnO with europium (Eu^{3+}) and lithium (Li^{+}) ions has become a viable method for engineering lattice distortions, defect states, and local crystal field environments.

This chapter presents the experimental results and discusses the structural and Raman properties of ZnO co-doped with (Eu^{3+} and Li^{+}) thin films synthesised via the dip-coating process. We investigated the incorporation effects of europium (Eu^{3+}) and lithium (Li^{+}) ions on the crystallinity, microstructure, and vibrational modes of ZnO thin films, as well as the effect of the number of deposited layers on the structural and functional characteristics of pure ZnO, ZnO:2%Eu, and ZnO:2% Eu 7%Li compositions.

The results are presented in two parts: Part (1) focuses on the effect of Eu^{3+} and Li^{+} co-doping on ZnO thin films, while Part (2) illustrates the influence of the number of layers on the structural and optical properties of the films.

IV.2. Effect of Eu^{3+} and Li^{+} Doping on ZnO Thin Films

IV.2.1. Structural Study by X-ray Diffraction (XRD)

X-ray diffraction (XRD) analysis was performed to investigate the structural transformations in pure ZnO, ZnO:2%Eu, and ZnO:2%Eu 7%Li thin films deposited on glass substrates via the sol-gel spin-coating method. The refinement of the XRD diffractograms using HighScore Plus for films with varying numbers of deposited layers (10, 15, and 20) is presented in Figure 1(a-b-c). All diffraction peaks were identified and assigned to their respective crystal planes

Thin film with 10 layers

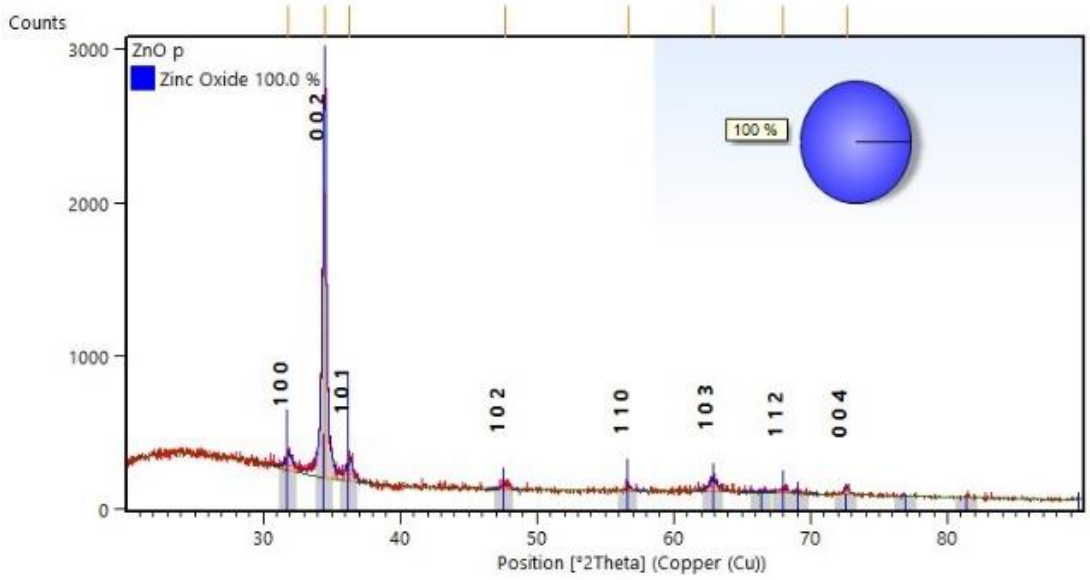

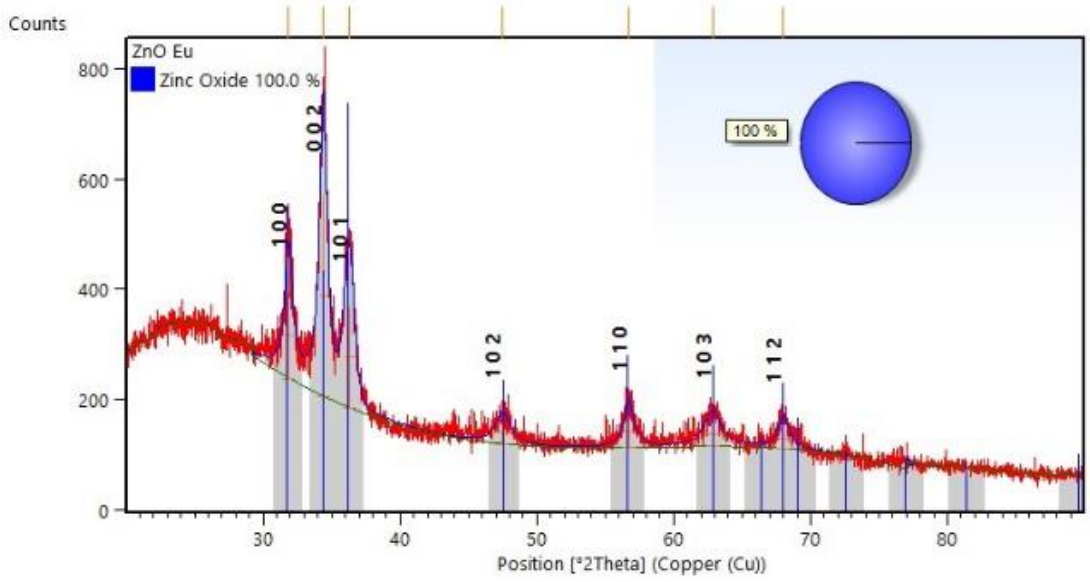

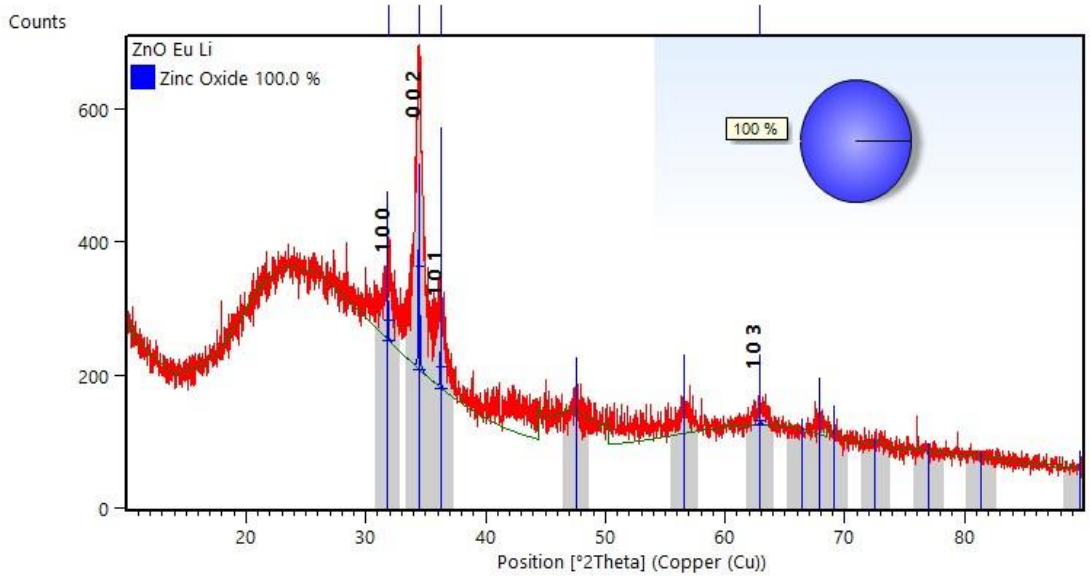

Figure IV.1a: Refinement of X-ray diffraction patterns of pure ZnO, ZnO:2%Eu, and ZnO:2%Eu 7%Li 10 thin films using Philips HighScore Plus.

- **Thin film with 15 layers**

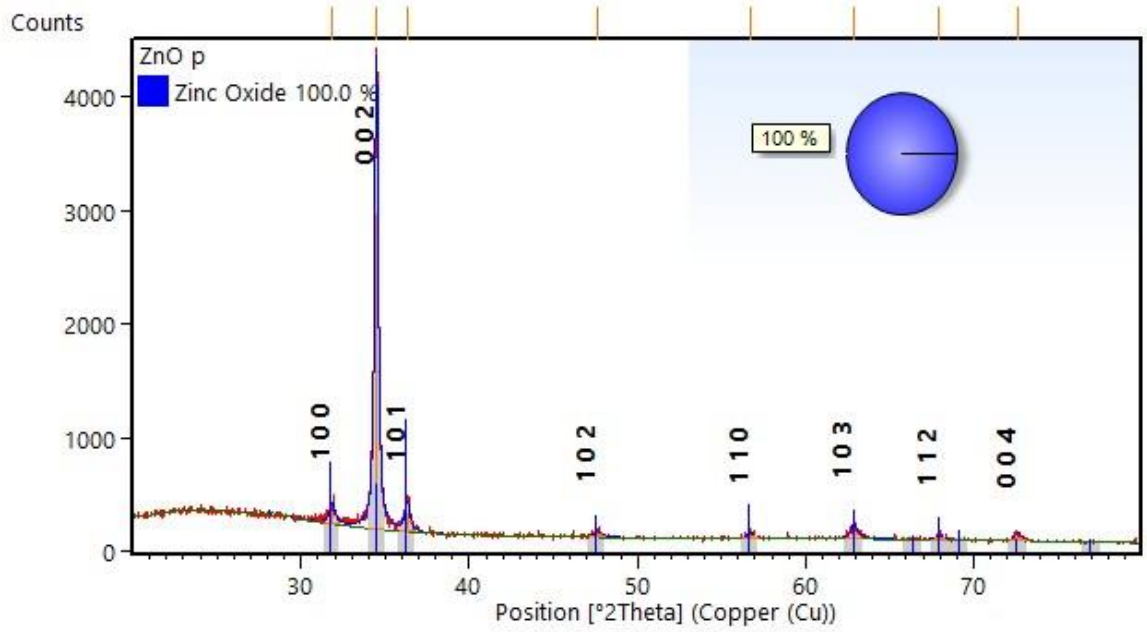

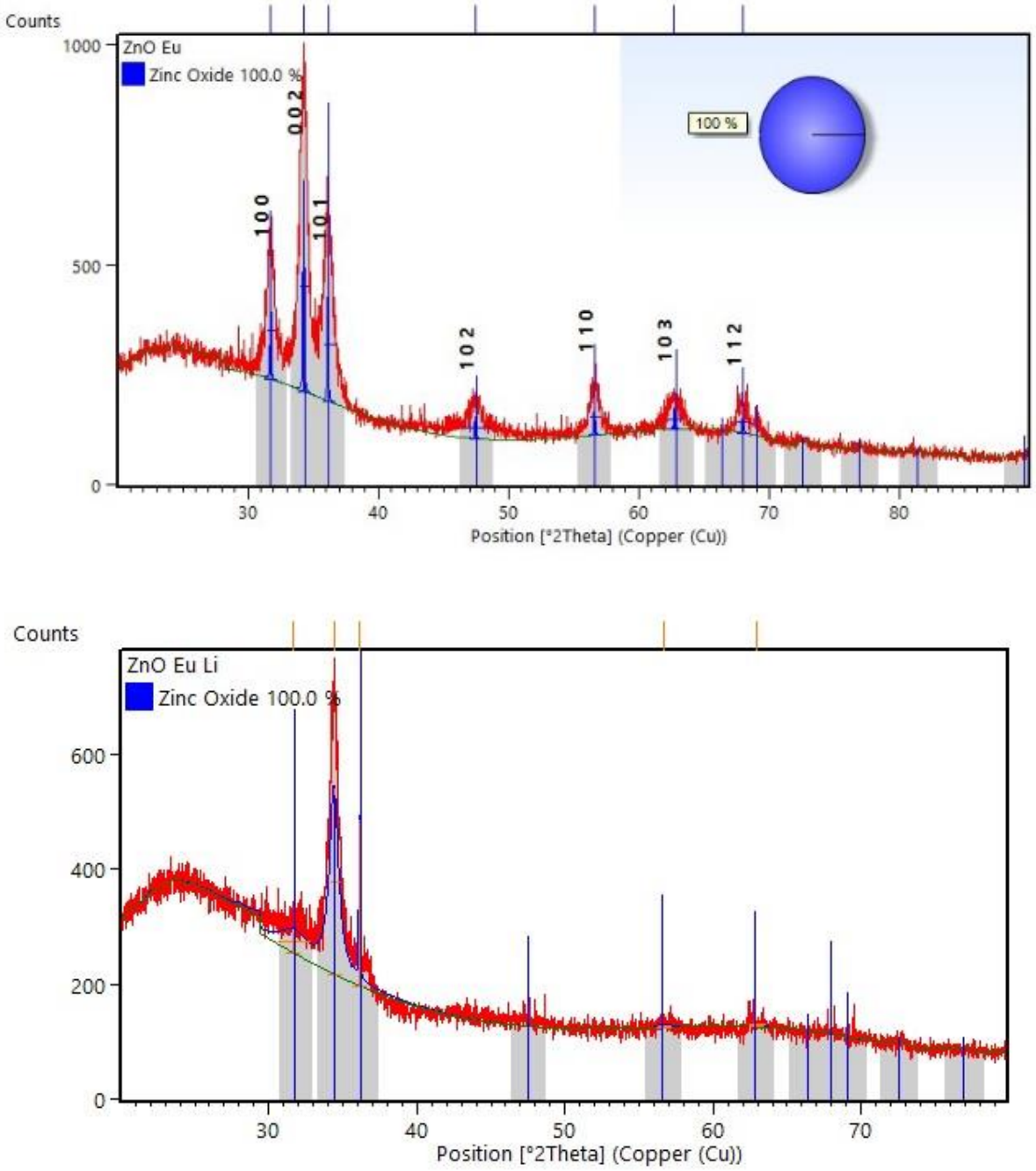

Figure IV.1b: Refinement of X-ray diffraction patterns of pure ZnO, ZnO:2%Eu, and ZnO:2%Eu 7%Li 15 thin films using Philips HighScore Plus.

- **Thin film with 20 layers**

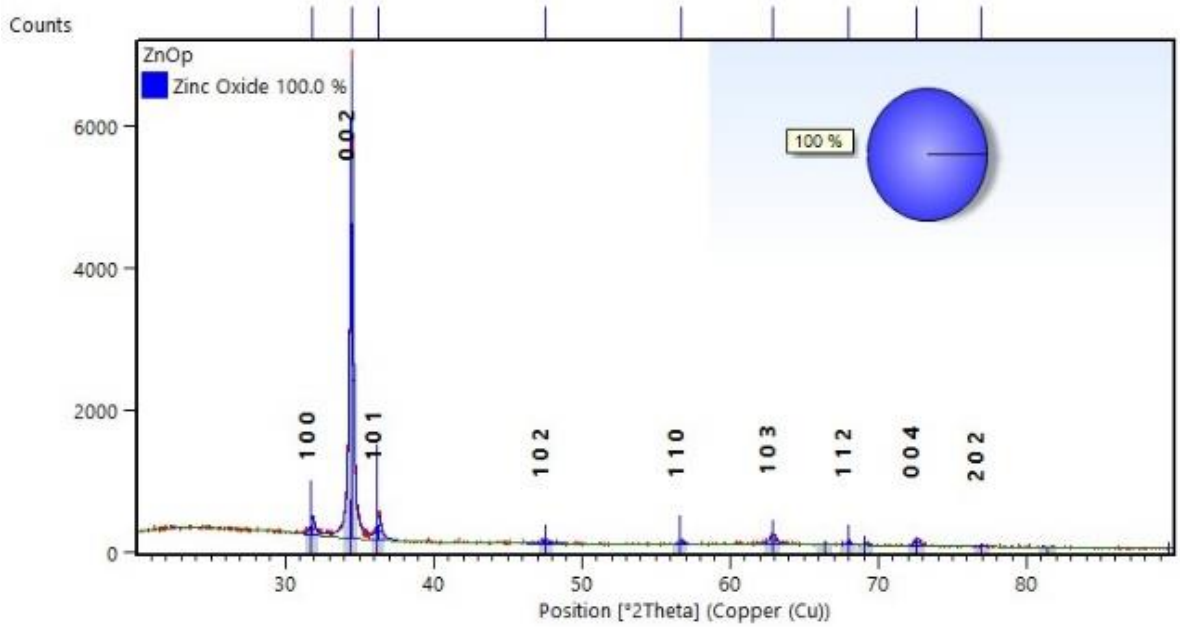

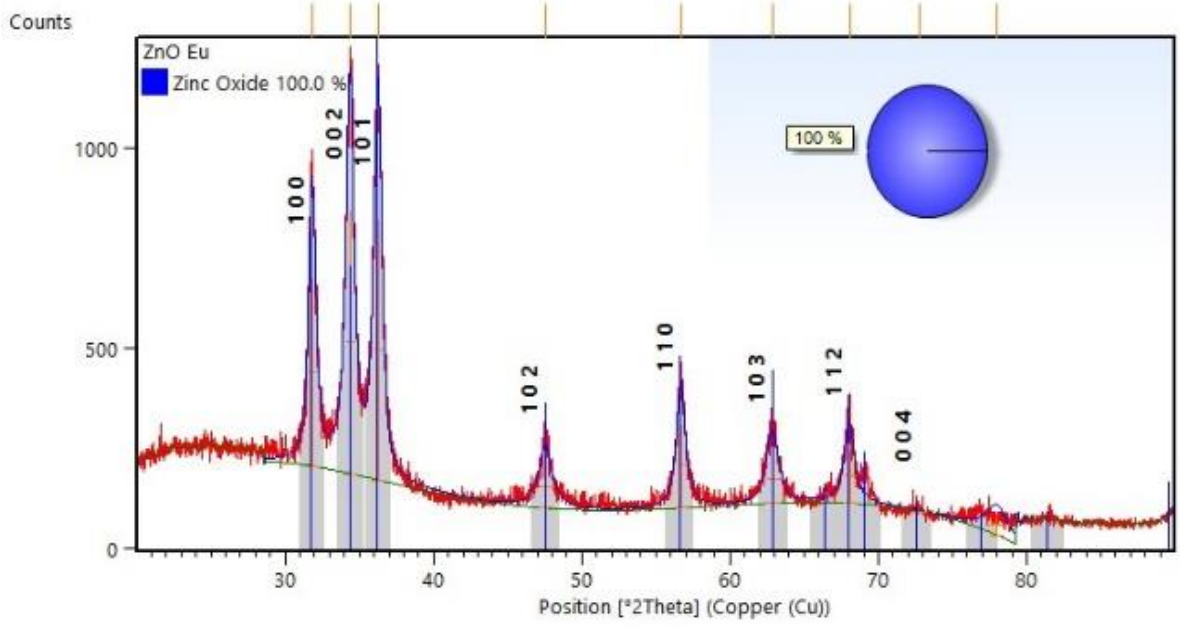

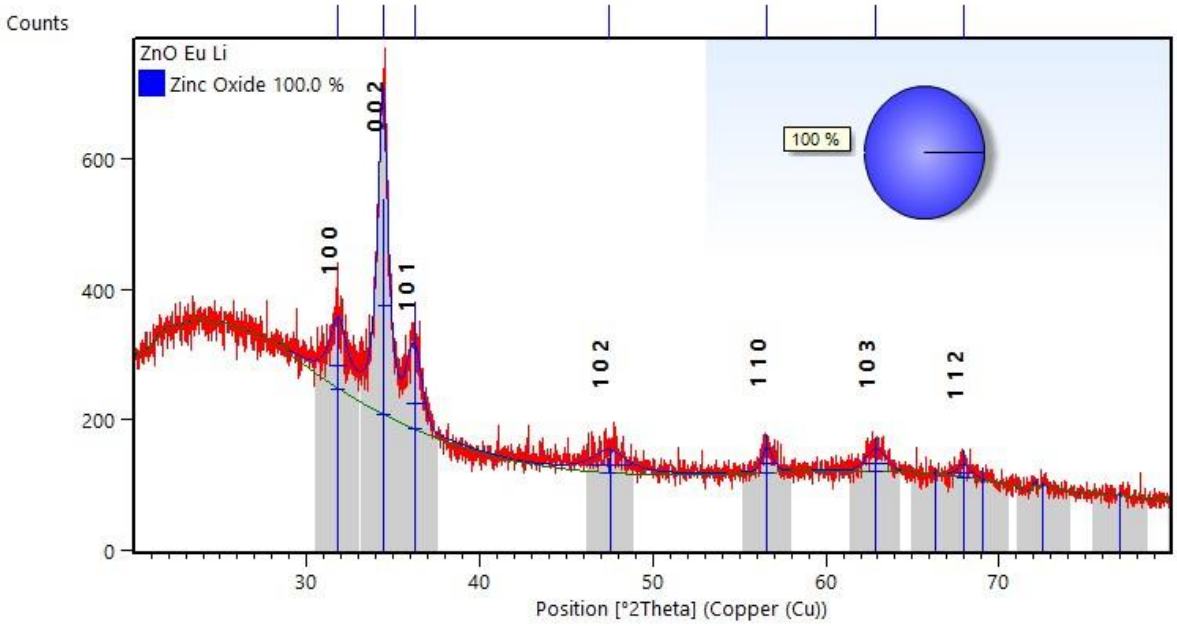

Figure IV.1c: Refinement of X-ray diffraction patterns of pure ZnO, ZnO:2%Eu, and ZnO:2%Eu 7%Li thin films 20 layers using Philips HighScore Plus.

All samples crystallise in the hexagonal wurtzite structure (space group $P6_3mc$, JCPDS No. 01-079-2205) with a strong preferential orientation along the (002) plane, This result is consistent with the literature [6-7]. No secondary phases, such as europium oxide or lithium compounds, were detected, confirming the successful incorporation of Eu^{3+} and Li^{+} into the ZnO lattice

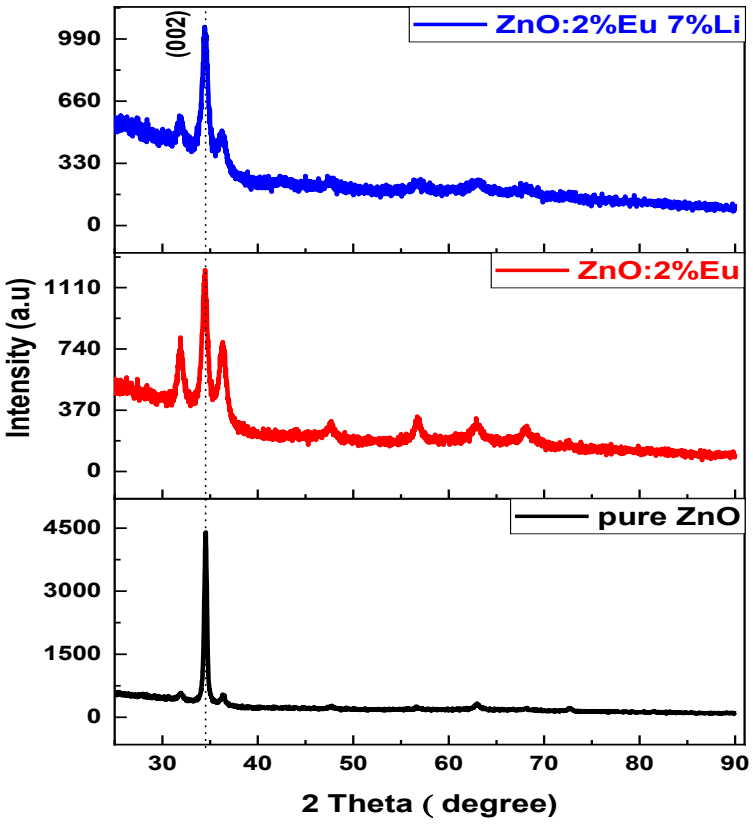

Figure IV.2: XRD patterns of pure ZnO, ZnO:2%Eu, and ZnO:2%Eu 7%Li thin films with 10 layers.

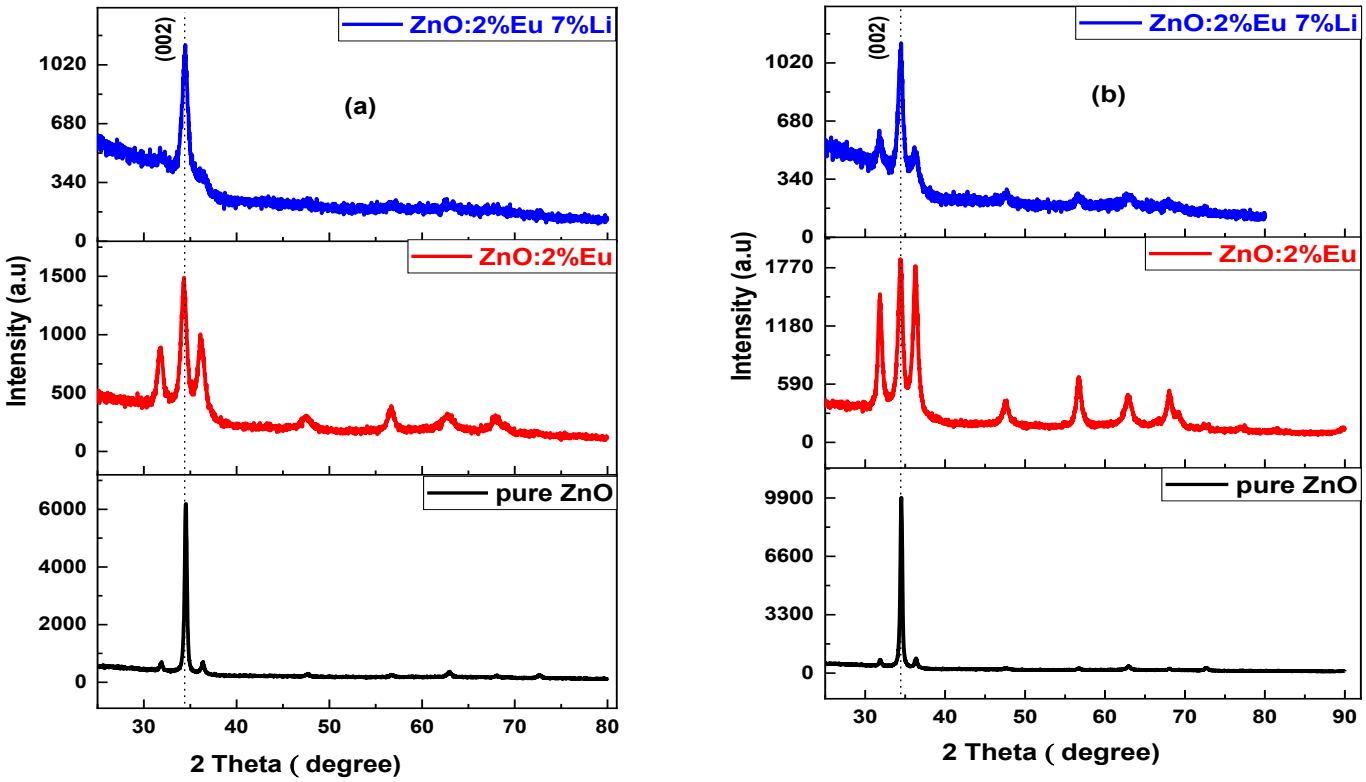

Figure IV.3: XRD patterns of pure ZnO, ZnO:2%Eu, and ZnO:2%Eu 7%Li thin films with : (a) 15 layers and (b) 20 layers.

Upon doping, the (002) peak intensity decreases and its full width at half maximum (FWHM) increases, indicating lattice disorder and strain induced by dopant incorporation. crystallite size, calculated from Scherrer's equation, varies from 19–27 nm in pure ZnO, increases to about 37 nm for ZnO:2%Eu, and further to 59 nm for ZnO:2%Eu 7%Li (Table 1). This crystallite size increase suggests that Li^{+} promotes grain growth, when combined with Eu^{3+}, possibly by reducing lattice strain [8] most likely through a reduction of lattice strain.

Table IV.1: The various results were obtained using the HighScore Plus Program.

Samples	Phases	FWHM	2θ(deg) more intense peaks	hkl	d_{hkl}	$D_{Scherrer}$ (nm)	D_{moy} (nm)
10 films							
Pure ZnO	ZnO	0.61	31.90	(100)	2.80	14	19
	ZnO	**0.30**	**34.50**	**(002)**	**2.60**	**28**	
	ZnO	0.54	36.33	(101)	2.47	16	
ZnO:2%Eu	ZnO	0.74	31.87	(100)	2.81	11	37
	ZnO	**0.68**	**34.42**	**(002)**	**2.60**	**12**	
	ZnO	0.94	36.29	(101)	2.47	89	
ZnO:2%Eu7%Li	ZnO	1.07	31.86	(100)	2.81	77	59
	ZnO	**0.71**	**34.44**	**(002)**	**2.60**	**12**	
	ZnO	1.02	36.24	(101)	2.48	89	
15 films							
Pure ZnO	ZnO	0.40	31.84	(100)	2.81	21	25
	ZnO	**0.27**	**34.49**	**(002)**	**2.60**	**31**	
	ZnO	0.35	36.32	(101)	2.47	24	
ZnO:2%Eu	ZnO	0.68	31.75	(100)	2.81	12	37
	ZnO	**0.73**	**34.29**	**(002)**	**2.61**	**11**	
	ZnO	0.95	36.15	(101)	2.48	88	
ZnO:2%Eu7%Li	ZnO	2	31.7	(100)	2.82	41	46
	ZnO	**0.73**	**34.41**	**(002)**	**2.60**	**11**	
	ZnO	0.09	36.12	(101)	2.49	88	
20 films							
Pure ZnO	ZnO	0.33	31.86	(100)	2.81	25	27
	ZnO	**0.27**	**34.49**	**(002)**	**2.60**	**31**	
	ZnO	0.35	36.33	(101)	2.47	24	
ZnO:2%Eu	ZnO	0.60	31.83	(100)	2.81	14	13
	ZnO	**0.68**	**34.38**	**(002)**	**2.61**	**12**	
	ZnO	0.70	36.26	(101)	2.48	12	
ZnO:2%Eu7%Li	ZnO	1.17	31.81	(100)	2.81	71	55
	ZnO	**0.71**	**34.40**	**(002)**	**2.60**	**12**	
	ZnO	1.01	36.22	(101)	2.48	83	

The lattice parameters and unit cell volume (Table 2) also show slight variations with doping. It is noticed that, the incorporation of Eu^{3+} ions, despite their larger ionic radius (0.95 Å) compared to Zn^{2+}, leads to a decrease in lattice volume, which may indicate a limited solubility of Eu^{3+} and its incorporation in the ZnO lattice. The c/a ratios remain close to the ideal wurtzite value (1.60) , confirming that the hexagonal symmetry is preserved across all samples.

Table IV.2: Lattice parameters and stresses exerted on pure and Eu-doped ZnO and (Eu, Li) co-doped ZnO thin films

Samples	Structure	a (A°)	c (A°)	c / a	V (A° ^{3})	ε %
10 films						
Pure ZnO	hexagonal wurtzite	3.246	5.203	1.60	47.48	0.69
ZnO :2%Eu	hexagonal wurtzite	3.244	5.212	1.60	47.51	1.11
ZnO :2%Eu7%Li	hexagonal wurtzite	3.246	5.204	1.60	47.48	1.33
15 films						
Pure ZnO	hexagonal wurtzite	3.247	5.205	1.60	47.51	0.49
ZnO :2%Eu	hexagonal wurtzite	3.246	5.222	1.60	47.50	1.12
ZnO :2%Eu7%Li	hexagonal wurtzite	3.247	5.202	1.60	47.49	1.65
20 films						
Pure ZnO	hexagonal wurtzite	3.249	5.204	1.60	47.58	0.45
ZnO :2%Eu	hexagonal wurtzite	3.247	5.198	1.60	47.46	0.80
ZnO :2%Eu7%Li	hexagonal wurtzite	3.249	5.210	1.60	47.63	1.348

Film thickness also plays a role: thicker films (20 layers) exhibit sharper and more intense diffraction peaks compared to thinner films (10 layers), consistent with improved crystallinity due to the larger amount of deposited material. Thus, both doping and the number of layers strongly affect the structural characteristics of ZnO thin films.

IV.2.2. Raman Spectroscopy:

Raman spectroscopy was employed to investigate the vibrational properties and lattice dynamics of pure and doped ZnO thin films. Measurements were performed at room temperature using two excitation wavelengths, 514.7 nm (visible) and 325 nm (UV), providing complementary information on bulk and near-surface phonon behaviour. The Raman spectra were recorded using [9]:

- A He–Cd laser with a wavelength of 325 nm (UV excitation).
- A diode-pumped solid-state laser with a wavelength of 514.7 nm (green excitation).

All measurements were conducted at room temperature in a backscattering geometry to ensure accurate probing of the phonon modes.

IV.2.2.1. Raman Spectra with 325 nm Excitation:

When ZnO is excited with a 325 nm ultraviolet laser, the photon energy is close to its bandgap (~3.37 eV), which induces a resonance Raman effect. This excitation primarily probes the surface and near-surface regions, making it especially effective for detecting local distortions and dopant-induced modification.

The Raman spectrum of pure ZnO, ZnO:2%Eu, and ZnO:2%Eu 7%Li thin films with 10 deposited layers (Figure 4) is dominated by the longitudinal optical phonon modes. A strong peak is observed near ~574 cm^{-1}, corresponding to the A_1(LO) mode, while its second order overtone, $2A_1$(LO), appears around ~1148 cm^{-1}. In pure ZnO, these modes are sharp and intense, confirming the wurtzite crystal structure and good crystallinity. With Eu doping, the A_1(LO) peak becomes broader and slightly weaker, reflecting lattice strain and structural disorder introduced by the substitution of Zn^{2+} with larger Eu^{3+} ions. The $2A_1$(LO) mode is still visible but reduced in definition, consistent with enhanced phonon scattering due to defects. In the co-doped

ZnO:2%Eu-7%Li sample, the A_1(LO) peak regains intensity and appears sharper compared to the Eu-only case, while the $2A_1$(LO) mode is also more distinct, The Raman spectra reveal that the E_2(high) mode, which is characteristic of the oxygen vibrations in the ZnO lattice (~437 cm^{-1}), is still present but with lower intensity compared to the A_1(LO) and $2A_1$ modes. The reduced intensity of the E_2(high) mode relative to the strong A_1(LO) response suggests poor surface crystallinity, associated with the presence of structural defects such as oxygen vacancies and zinc interstitials. This effect is particularly pronounced in ZnO doped with 2% Eu and in ZnO co-doped with 2% Eu 7% Li, where the A_1(LO) mode becomes dominant. Such behavior indicates that while Eu doping introduces significant lattice disorder, Li co-doping partly compensates for Eu-induced strain, stabilizing the ZnO wurtzite phase. Nevertheless, the enhanced A_1(LO) intensity compared to the E_2(high) mode confirms that lattice defects remain active, reflecting a degradation of surface crystallinity despite the partial structural recovery promoted by Li incorporation.

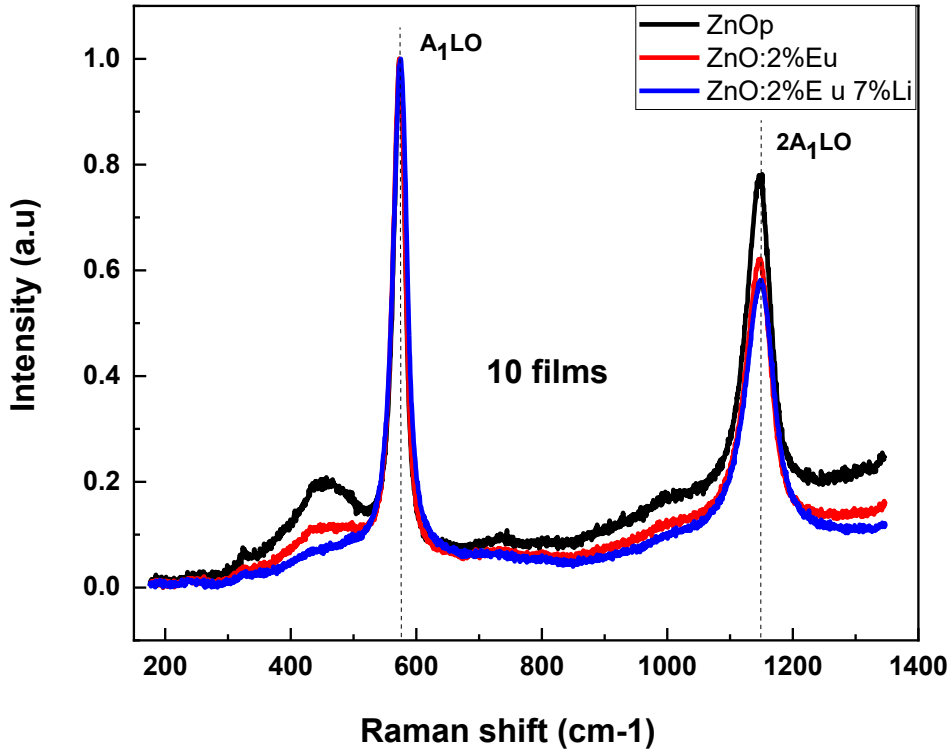

Figure IV.4: Raman spectra of pure ZnO, ZnO:2%Eu, and ZnO:2%Eu 7%Li thin films (10 layers) under 325 nm excitation.

The Raman spectrum of the 20-layer films (Figure 5) shows, for pure ZnO, a strong and well-defined A_1(LO) mode at ~574 cm^{-1} together with its overtone $2A_1$(LO) at ~1148 cm^{-1}, consistent with the wurtzite structure. Compared with the 15-layer films, these peaks appear sharper and slightly more intense, indicating that increasing thickness reduces disorder and improves the overall structural arrangement. In ZnO:2%Eu, however, the A_1(LO) peak becomes broadened and less intense, and the $2A_1$(LO) mode remains weak, reflecting lattice distortions introduced by Eu^{3+} incorporation. A similar phenomenon is observed in the co-doped ZnO:2%Eu 7%Li films, where only a slight increase in the E_2(high) vibration at ~437 cm^{-1} can be detected. Nevertheless, the E_2(high) mode remains of very low intensity compared to the A_1(LO) and $2A_1$(LO) features, pointing to a degradation of surface crystallinity. This clearly suggests that Li does not effectively restore the lattice quality, as the enhancement of defect-related vibrational modes dominates the spectra.

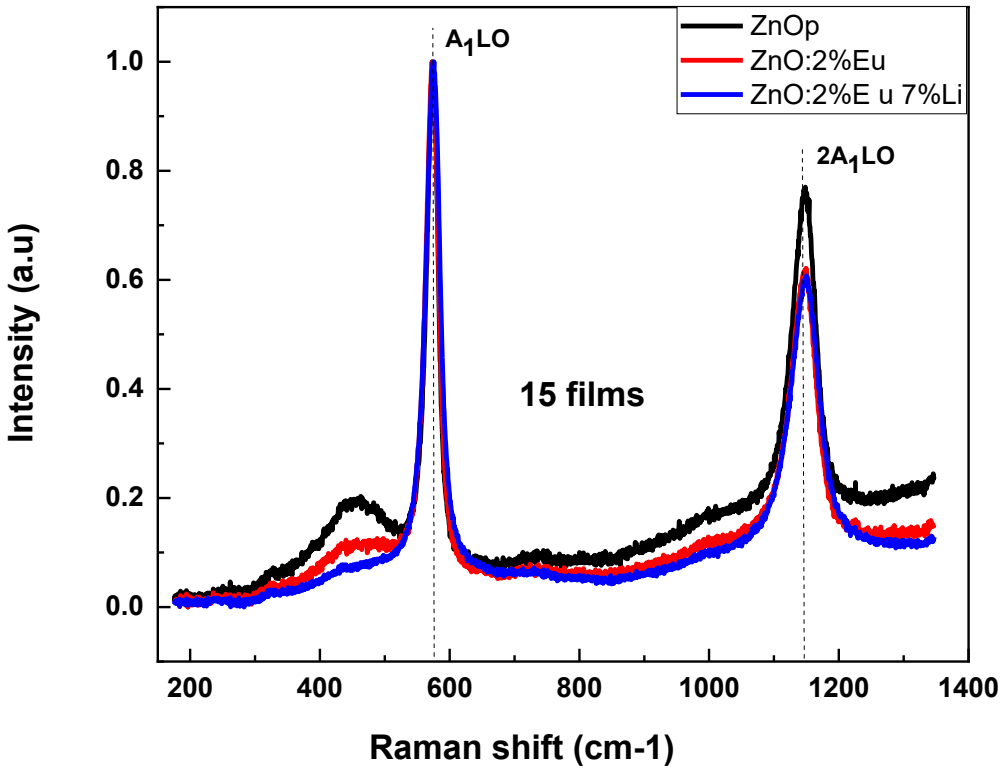

Figure IV.5: Raman spectra of pure ZnO, ZnO:2%Eu, and ZnO:2%Eu 7%Li thin films (20 layers) under 325 nm excitation.

The Raman spectrum of the 25-layer films (Figure 6) further illustrates this trend. Pure ZnO displays sharper and more intense A_1(LO) and $2A_1$(LO) peaks compared to thinner films, reflecting the expected improvement in crystallinity with increasing thickness. For ZnO:2%Eu, the A_1(LO) peak remains broadened and of lower intensity relative to pure ZnO, consistent with persistent lattice strain, though phonon definition slightly improves compared to thinner films. In the co-doped ZnO:2%Eu 7%Li sample, however, the E_2(high) mode is almost absent, while the A_1(LO) and $2A_1$(LO) modes are dominant. This imbalance confirms poor surface crystallinity and the presence of numerous lattice defects such as oxygen vacancies or zinc interstitials. Therefore, contrary to initial expectations, Li co-doping does not effectively stabilise the lattice or enhance crystallinity; instead, it appears to promote the persistence of defect-related vibrational activity [10]

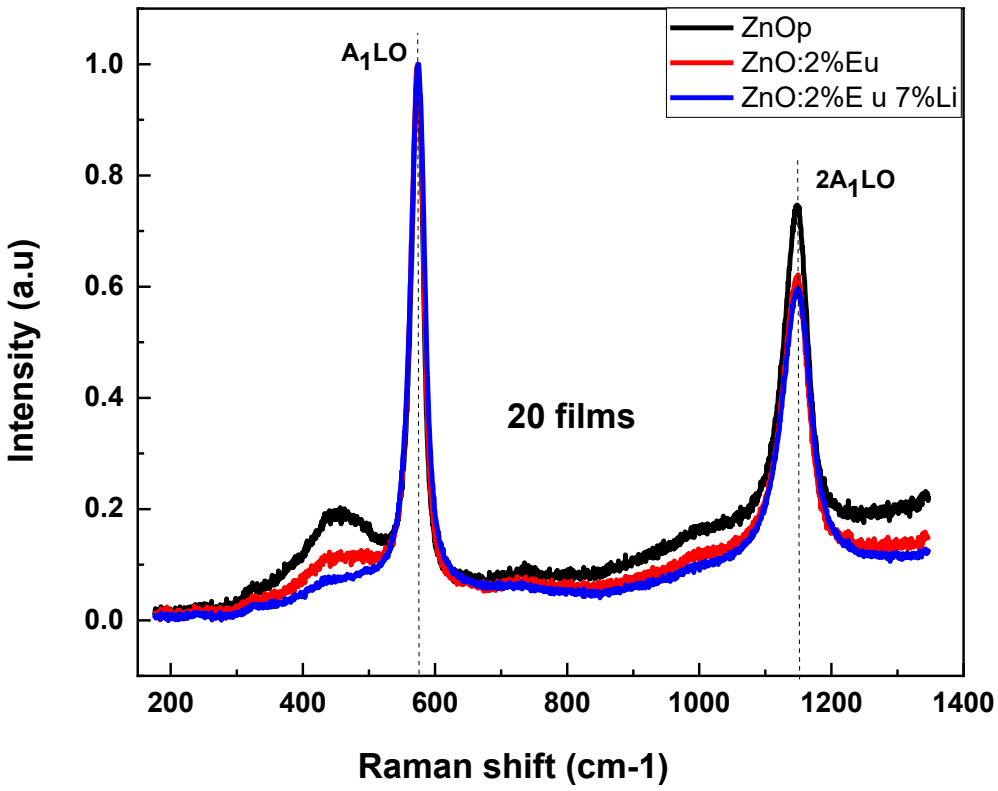

Figure IV.6: Raman spectra of pure ZnO, ZnO:2%Eu, and ZnO:2%Eu 7%Li thin films

IV.3. Influence of Film Thickness on the Raman Spectra of Pure, Eu-Doped, and Eu–Li Co-Doped ZnO with 325 nm excitation:

Raman analysis across the three film thicknesses reveals a clear trend in the evolution of the A_1(LO) phonon mode. As the number of deposited layers increases from 10 to 20, the A_1(LO) peak becomes progressively sharper and more intense, indicating an increase in surface structural disorder. This trend is consistent with XRD results, which also showed enhanced peak intensity and reduced broadening for thicker films. The sharpening of the A_1(LO) mode suggests that thicker layers exhibit fewer lattice imperfections, such as oxygen vacancies and zinc interstitials, which commonly broaden and weaken phonon features in thinner or more defective films [11-12].

The dominance of the A_1(LO) mode under 325 nm excitation arises from resonance effects close to the ZnO bandgap, which amplify defect- and carrier-related scattering processes. As the structural quality improves with thickness, the resonance coupling between lattice vibrations and defect states becomes more pronounced, giving rise to the stronger A_1(LO) feature. In this context, the systematic enhancement of the A_1(LO) phonon mode can be regarded as a reliable indicator of improved crystallinity.

IV.3.1. Raman Spectra with 514.7 nm Excitation:

When ZnO is excited with a 514.7 nm visible laser, the photon energy lies below its bandgap, resulting in a non-resonant Raman effect. This excitation penetrates deeper into the material and primarily probes the bulk lattice vibrations, making it suitable for evaluating the overall crystallinity and long-range structural order of ZnO.

The Raman spectra of pure ZnO, ZnO:2%Eu, and ZnO:2%Eu 7%Li thin films deposited with 10 layers show the characteristic phonon modes of ZnO. The E_2(low) mode at ~98 cm^{-1} arises from vibrations of the Zn sublattice, while the strong E_2(high) mode near ~437 cm^{-1} corresponds to oxygen sublattice vibrations. This latter peak is a reliable indicator of the ZnO hexagonal wurtzite structure and reflects the good crystallinity of the films.. The mode observed around 580–590 cm^{-1} corresponds to the E_1(LO) vibration, which is particularly sensitive to oxygen vacancies, lattice defects, and dopant incorporation.

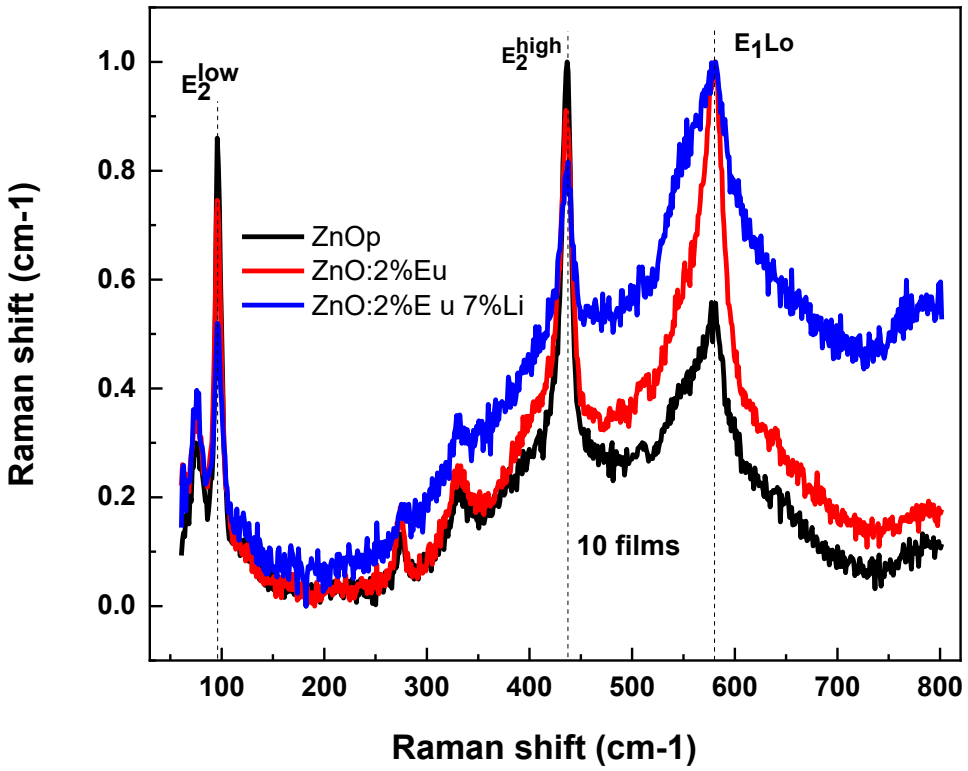

Figure IV.7: Raman spectra of pure ZnO, ZnO:2%Eu, and ZnO:2%Eu 7%Li thin films (10 layers) under 514.7 nm excitation.

When Eu is introduced, the E_2(high) peak broadens and reduces slightly in intensity, signalling lattice distortion caused by the larger Eu^{3+} ions substituting for Zn^{2+}. With Li co-doping, this broadening persists, but the intensity of the E_1(LO) defect-related mode increases strongly, indicating that Li incorporation modifies the defect landscape, likely enhancing oxygen vacancies and electron phonon interactions. Slight shifts in peak positions between pure and doped samples confirm the presence of local strain and structural distortions. Overall, the results demonstrate that while doping introduces disorder, the wurtzite ZnO structure remains intact, with Li co-doping enhancing defect-related modes that can significantly affect the optical and luminescent behaviour of the films [13], which is consistent with Raman analysis on the surface.

The Raman spectra of pure ZnO, ZnO:2%Eu, and ZnO:2%Eu 7%Li thin films with 15 deposited layers are shown in Figure 10, and compared with the 10 ayer

samples, the 15 layer films display sharper and more intense peaks, reflecting improved crystallinity with increased thickness. In the ZnO:2%Eu doped films, the E_2(high) peak broadens and weakens relative to pure ZnO, due to lattice strain and disorder introduced by Eu^{3+} substitution.

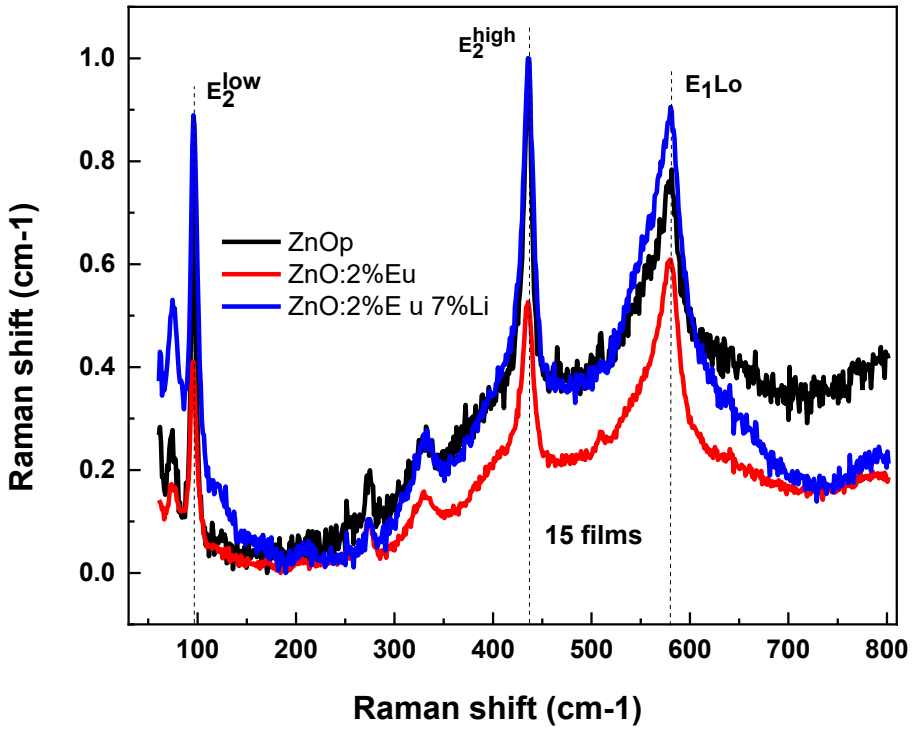

Figure IV.8: Raman spectra of pure ZnO, ZnO:2%Eu, and ZnO:2%Eu 7%Li thin films (15 layers) under 514.7 nm excitation.

In the co-doped ZnO:2%Eu 7%Li sample, the Raman peaks show higher intensity than the Eu-only films, and the E2 high mode intensity had increased more than the intensity of pure ZnO, showing a better crystallisation with the incorporation of lithium. However, the E_1(LO) defect-related mode becomes more prominent, suggesting that Li enhances the defects rate while simultaneously improving crystalline structure. These results confirm that with increasing thickness, Raman signals strengthen, and the co-doping with Li helps mitigate the disorder caused by Eu incorporation.

The Raman spectra of the 20 layer films in Figure 11 reveal the clearest phonon features among the three thicknesses. Pure ZnO shows sharp and intense

E_2(high) and E_1(LO) peaks, confirming excellent crystallinity. In the ZnO:2%Eu sample, the E_2(high) peak remains broadened compared to pure ZnO, but the adverse effect of Eu doping is reduced in thicker films, as greater thickness allows the lattice to relax and partially restore order.

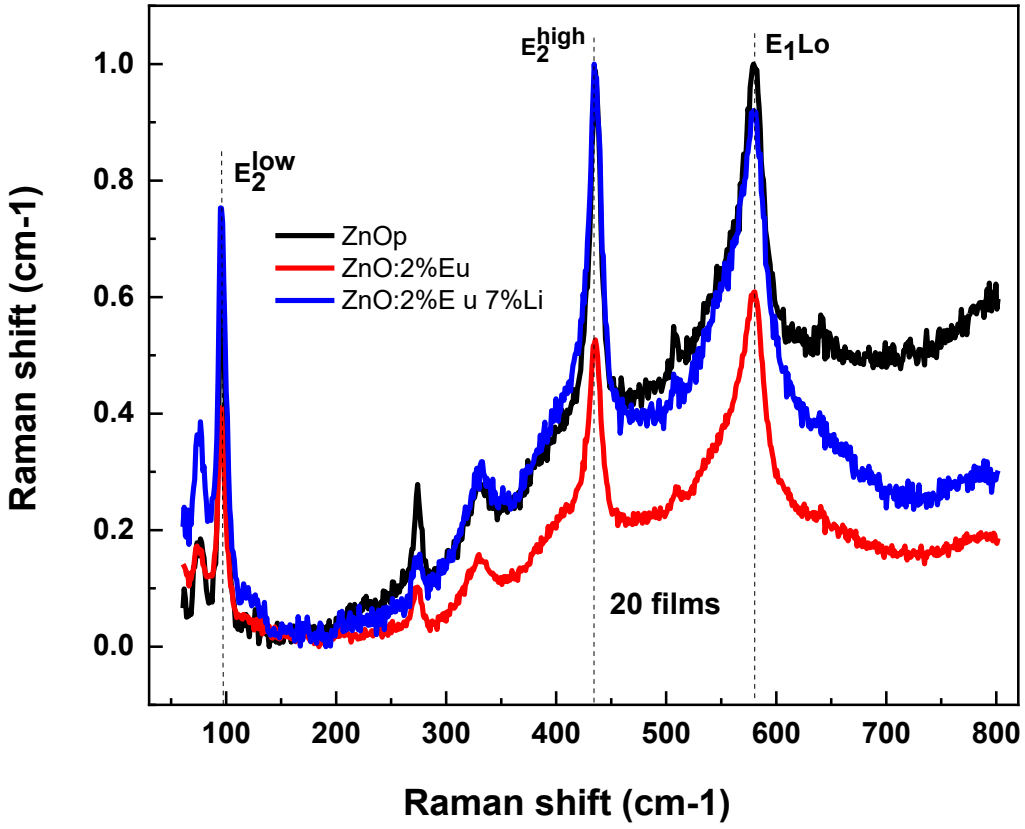

Figure IV.9: Raman spectra of pure ZnO, ZnO:2%Eu, and ZnO:2%Eu 7%Li thin films (20 layers) under 514.7 nm excitation.

For the ZnO:2%Eu 7%Li co-doped sample, the Raman peaks are stronger and sharper than in the Eu-only sample, closely resembling those of pure ZnO. At the same time, the intensity of the E_1(LO) mode is notably higher, indicating that Li co-doping enhances defect related vibrations, likely through modification of oxygen vacancies and electron phonon interactions. Overall, the 20 layer spectra demonstrate that increased film thickness leads to improved crystallinity and signal quality, while Li co-doping effectively counteracts Eu-induced disorder and enriches defect-related vibrational modes.

IV.4. Influence of Film Thickness on the Raman Spectra of Pure, Eu-Doped, and Eu,Li Co-Doped ZnO with 514.7 nm excitation:

Raman analysis across the three film thicknesses reveals two clear trends: the influence of thickness on crystallinity and the impact of Eu and Li doping on lattice dynamics.

As the number of deposited layers increases from 10 to 20, the E_2(high) phonon mode becomes sharper and more intense, demonstrating a progressive improvement in crystallinity and long-range order. Pure ZnO consistently shows the strongest and most well-defined Raman features, serving as a structural reference. Eu doping alone introduces noticeable broadening and weakening of the E_2(high) mode across all thicknesses, reflecting lattice strain and disorder from the substitution of Zn^{2+} with larger Eu^{3+} ions.

In contrast, Li co-doping in ZnO:2%Eu 7%Li partially compensates this distortion: the E_2(high) peak sharpens relative to Eu-only films, while the E_1(LO) defect-related mode becomes increasingly intense, particularly in thicker samples. This indicates that Li incorporation modifies oxygen vacancies and enhances defect-related vibrations, while at the same time stabilising the lattice against Eu-induced strain. All results shows that increasing thickness enhances crystallinity, Eu doping disrupts the lattice, and Li co-doping improves structural quality while enriching defect-related phonon activity that may strongly influence the optical and luminescent behaviour of the films.

IV.4.1. Optical Properties (Photoluminescence)

The photoluminescence (PL) spectra presented in this section were recorded using the Raman spectrometer with a 488 nm excitation laser [14].

The photoluminescence (PL) spectra of pure ZnO, ZnO:2%Eu, and ZnO:2%Eu 7%Li thin films with 10 layers are presented in Figure 14. Pure ZnO exhibits a broad emission band in the visible range, extending from 500 to 700 nm, associated with intrinsic defects such as oxygen vacancies (V_0) and zinc interstitials (Zn_i). The emission intensity is relatively weak, indicating limited crystallinity and a higher defect density in thinner films (which is in agreement with Raman spectra recorded at 325 nm). Upon Eu^{3+} doping, additional emission features emerge in the orange red region, particularly around 591 nm ($^5D_0 \rightarrow {}^7F_1$ transition) and 613 nm

($^5D_0 \rightarrow {}^7F_2$ transition), which are characteristic intra 4f transitions of Eu^{3+} ions. The strong peak near 613 nm is known as the hypersensitive transition, which is highly influenced by the local symmetry of the Eu^{3+} site in the ZnO host lattice. Its increased intensity compared to the orange $^5D_0 \rightarrow {}^7F_1$ line indicates that Eu^{3+} ions occupy sites lacking inversion symmetry, consistent with substitutional or interstitial incorporation in the ZnO lattice. However, the emission remains modest due to inefficient energy transfer from the ZnO host. With Li co-doping , these Eu^{3+} emissions are noticeably enhanced. This enhancement is attributed to the role of Li^+ ions, which modify the defects rate of ZnO, particularly by influencing oxygen vacancies, showing that Li^+ plays a role in charge compensation and in facilitating energy transfer to Eu^{3+} ions.

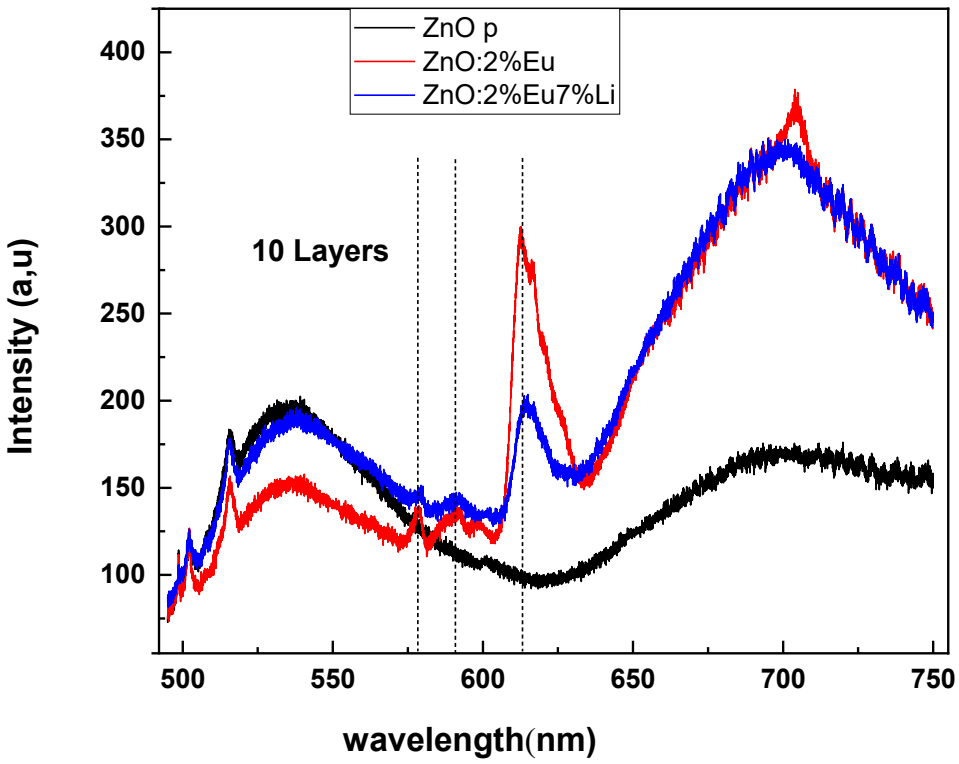

Figure IV.10: Photoluminescence spectra of pure ZnO, ZnO:2%Eu, and ZnO:2%Eu 7%Li thin films with 10 layers, recorded at room temperature under 488 nm excitation

For the 15 layer films schow in Figure 15, the PL emission intensities increase compared to the 10 layer samples. Pure ZnO still shows broad visible luminescence dominated by defect related recombination, but the band intensity is higher, reflecting improved crystallinity and larger active volume. In ZnO:2%Eu, the Eu^{3+} emission lines, especially the $^5D_0 \rightarrow {}^7F_2$ transition at 613 nm, become more distinct, indicating more efficient incorporation of Eu^{3+} ions into the ZnO matrix. Co-doping with Li^+ leads to a further enhancement of the Eu^{3+} red emission, with a noticeable increase in peak sharpness and intensity. This confirms that Li^+ modifies the defects rate in a way that favours host to dopant energy transfer and reduces non radiative recombination pathways.

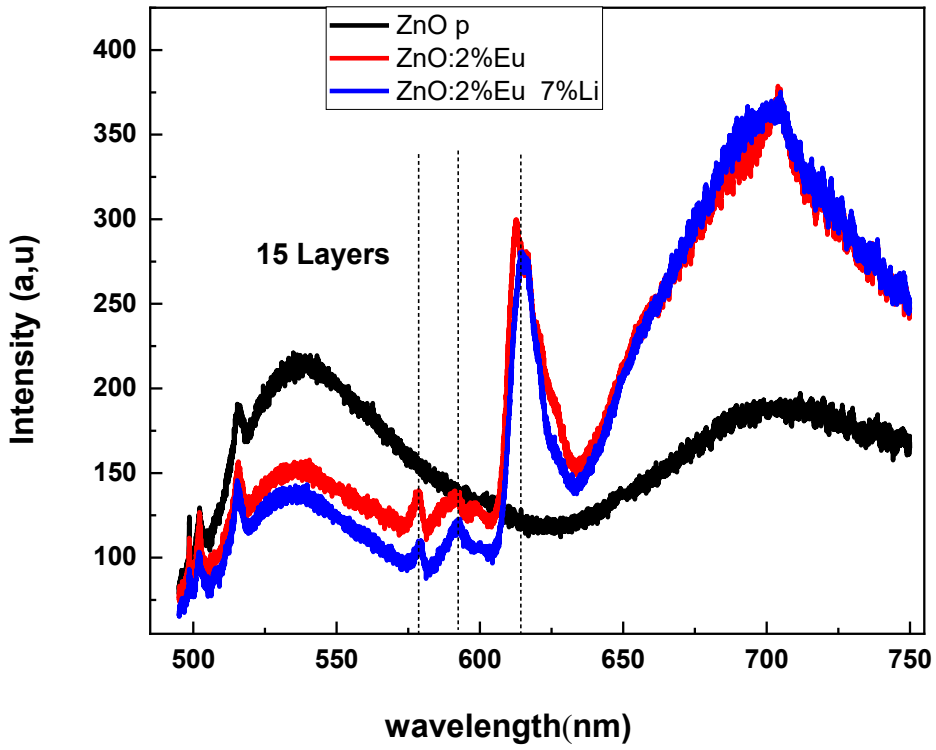

Figure IV.11:. Photoluminescence spectra of pure ZnO, ZnO:2%Eu, and ZnO:2%Eu 7%Li thin films with 15 layers, recorded at room temperature under 488 nm excitation

In the case of the 20 layer films, which are shown in Figure 16, the PL emission intensities reach their maximum. Pure ZnO displays a strong but still broad defect-related band, consistent with the larger thickness and higher excitation volume. The Eu^{3+}-doped films show very intense and sharp red emission lines, dominated by the $^5D_0 \rightarrow {}^7F_2$ transition at 615 nm, which becomes the main feature of the spectrum. Co-doping with Li^+ significantly amplifies this effect, producing the strongest red luminescence among the three thicknesses. The hypersensitive $^5D_0 \rightarrow {}^7F_2$ transition exhibits marked intensity enhancement compared to the $^5D_0 \rightarrow {}^7F_1$ line, indicating that Eu^{3+} ions occupy non-centrosymmetric sites. This behaviour demonstrates that increasing thickness improves crystallinity and defect control, while Li^+ co-doping provides additional excitation, resulting in efficient Eu^{3+} red emission.

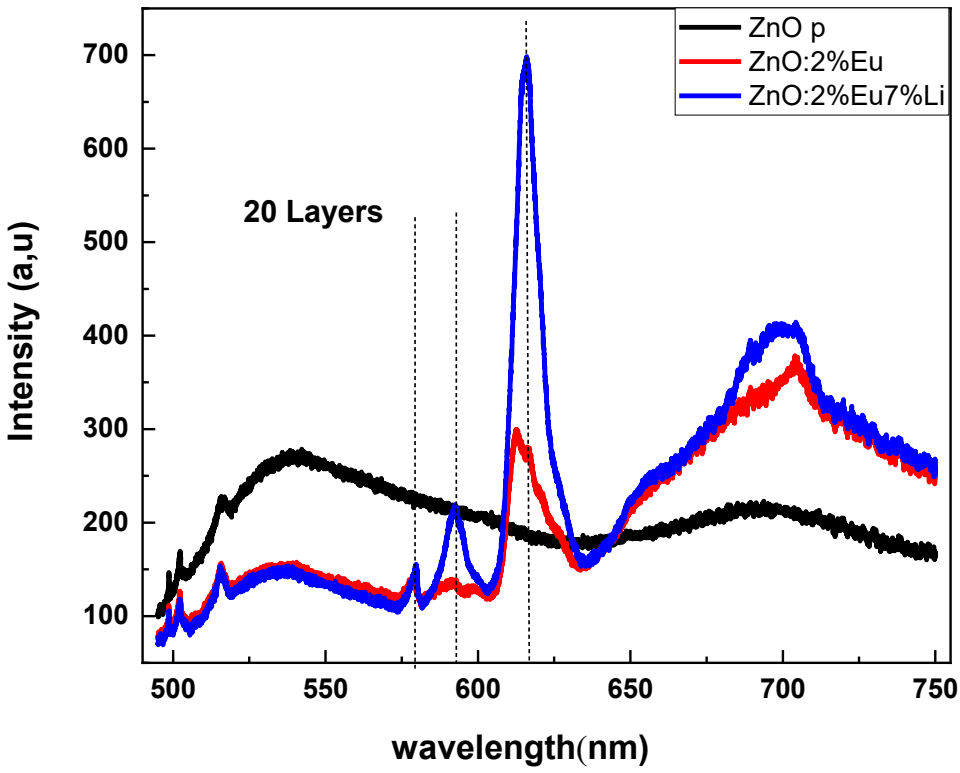

Figure IV.12: Photoluminescence spectra of pure ZnO, ZnO:2%Eu, and ZnO:2%Eu 7%Li thin films for 15 layers, recorded at room temperature under 488 nm excitation

IV.5. Influence of Layer Number on Photoluminescence Properties of Thin Films:

The evolution of the PL spectra with increasing film thickness (10, 15, and 20 layers), show in Figure17,18 and 19, provides important insights into the optical behaviour of pure ZnO, Eu^{3+}-doped ZnO, and ZnO:Eu,Li co-doped thin films. For pure ZnO, all samples exhibit a broad visible emission band extending from ~500 to 700 nm, which is attributed to intrinsic point defects such as oxygen vacancies (V_0) and zinc interstitials (Zn_i) [15-16]. The intensity of this defect-related emission systematically increases with film thickness, reflecting the combined effect of a larger excitation volume and improved crystallinity in thicker films.

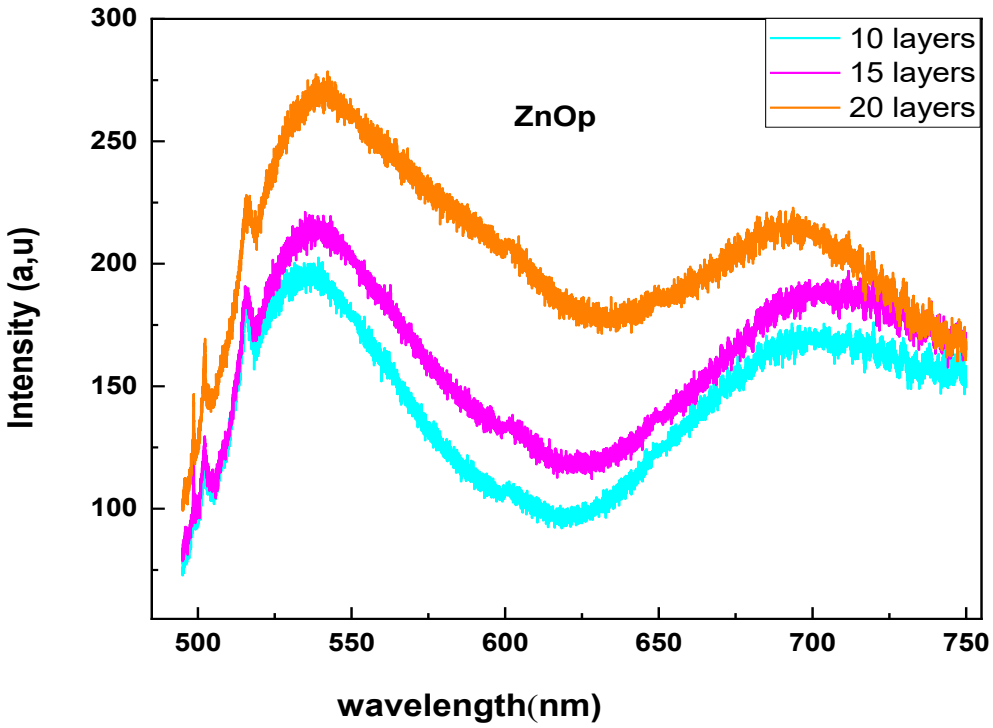

Figure IV.13: Photoluminescence spectra of pure ZnO thin films with different numbers of layers (10, 15, and 20) under 488 nm excitation.

In Eu^{3+}doped ZnO films, the characteristic intra-4f transitions of Eu^{3+} ions emerge, particularly the $^5D_0 \rightarrow {}^7F_1$ transition and the hypersensitive $^5D_0 \rightarrow {}^7F_2$ transition. These emissions become more distinct and intense as the number of layers increases,

demonstrating that thicker films favour more efficient incorporation of Eu^{3+} ions into the ZnO lattice and enhance energy transfer from the host matrix to the dopant centres.

The effect of Li^{+} co-doping is evident across all thicknesses, but it becomes most pronounced in the 20 layer films. Lithium incorporation not only assists in charge compensation of Eu^{3+} ions but also alters the defect chemistry of ZnO, reducing non-radiative recombination and creating favourable energy transfer pathways. Consequently, the Eu^{3+} emission, especially the hypersensitive $5D_0 \rightarrow 7F_2$ line, is significantly amplified in ZnO: Eu, Li films compared to Eu only doped samples.

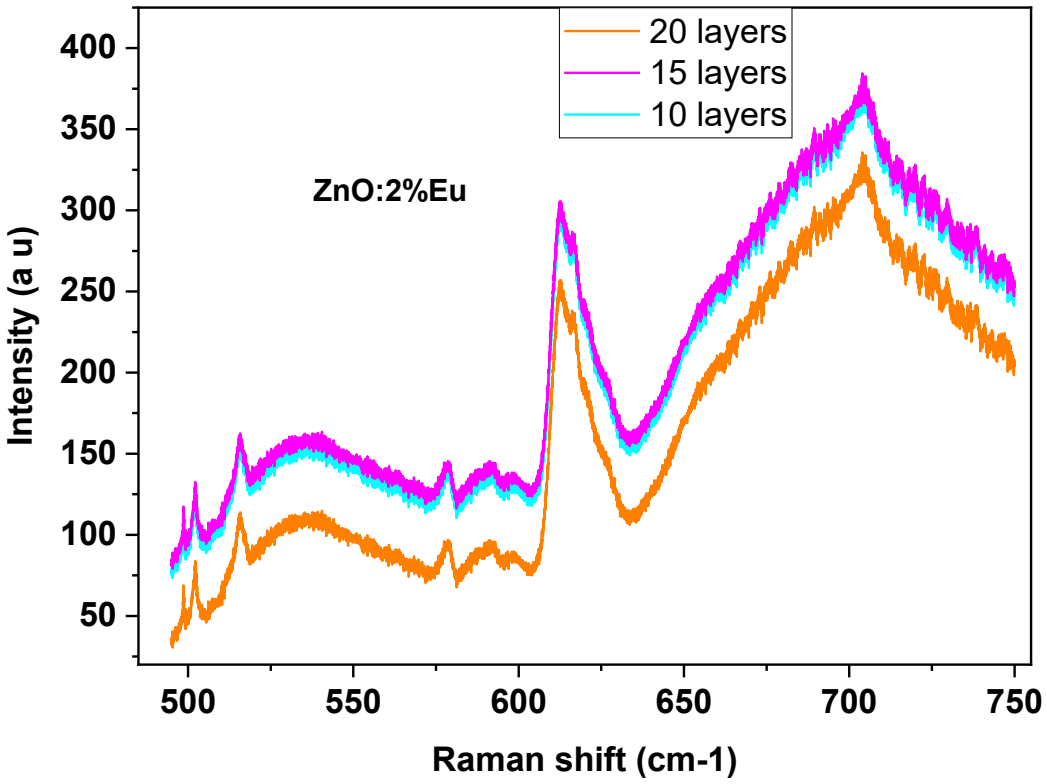

Figure IV.14: Photoluminescence spectra of ZnO:2%Eu thin films with different numbers of layers (10, 15, and 20) under 488 nm excitation.

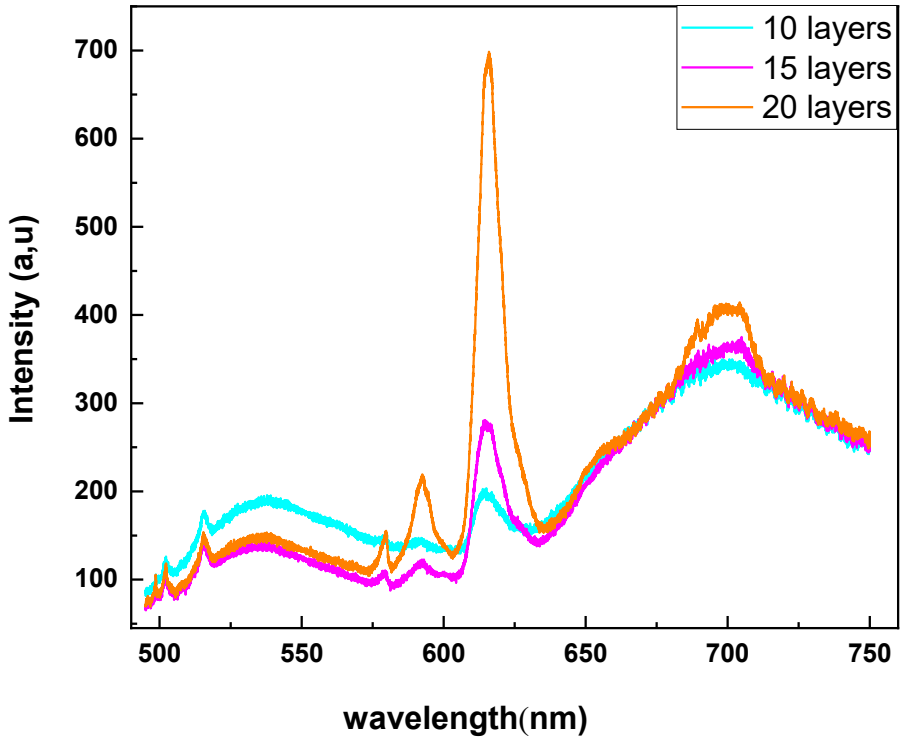

Figure IV.15: Photoluminescence spectra of ZnO :2%Eu 7%Li thin films with different numbers of layers (10, 15, and 20) under 488 nm excitation.

From our results, we noticed that the increasing film thickness enhances both defect related ZnO emission and Eu^{3+} luminescence, while Li^{+} co doping provides an additional enhance to Eu^{3+} red emission through defect modulation and charge compensation. The combined effects of thickness and Li^{+} incorporation thus play a crucial role in optimising the luminescence efficiency of ZnO based thin films for potential optoelectronic and photonic applications.

General conclusions

GENERAL CONCLUSION

This thesis presents a detailed investigation of ZnO based materials doped with Eu^{3+} and co doped with Li^{+}, synthesised in both powder and thin-film forms using the sol-gel method. The work systematically explores the influence of dopant type, concentration, and film thickness on the structural, morphological, and optical properties of the materials, providing a comprehensive understanding of their luminescent behaviour.

X-ray diffraction (XRD) analysis confirmed the retention of the hexagonal wurtzite structure in all powders and thin films, with no secondary phases detected, indicating successful incorporation of Eu^{3+} and Li^{+} ions into the ZnO lattice. Doping and co-doping affected lattice parameters, crystallite size, and microstrain. Specifically, Eu^{3+} doping slightly increased lattice distortion due to the larger ionic radius of Eu^{3+} compared to Zn^{2+}, whereas Li^{+} co-doping partially compensated lattice strain, improving overall crystallinity.

Raman spectroscopy further confirmed structural integrity and provided insight into defect evolution. The characteristic A_1(LO) phonon mode and its overtones were observed in both powders and thin films. In thin films, the intensity and sharpness of these modes increased with the number of deposited layers, indicating reduced structural disorder and enhanced long-range ordering along the c-axis. Li^{+} co-doping further sharpened the Raman peaks, reflecting a decrease in oxygen vacancies and other defects, which is consistent with XRD results.

Morphological analysis of the ZnO: Eu and ZnO: Eu, Li powders revealed that the nanoparticles are predominantly uniform and nearly spherical, with sizes ranging from 27 to 31 nm depending on doping levels. Moderate aggregation was observed, forming small clusters, but the overall distribution remained homogeneous. Li^{+} co-doping

helped control particle growth, reducing large aggregates and producing a more uniform powder. The surface of the particles appeared smooth and well-defined, minimising structural defects that could act as non-radiative recombination centres. This well-ordered morphology directly supports efficient energy transfer from the ZnO host lattice to the Eu^{3+} ions, resulting in enhanced red luminescence intensity. Powders with smaller, more uniform particles consistently exhibited stronger emission, demonstrating a clear correlation between particle morphology and luminescent performance.

Photoluminescence (PL) measurements demonstrated that Eu^{3+} ions act as effective luminescent centres, producing strong red emission. Li^{+} co-doping enhanced the PL intensity in both powders and thin films, attributed to improved crystallinity, reduced defect related non radiative recombination, and more efficient energy transfer mechanisms. In powders, the PL enhancement is largely governed by reduced aggregation and defect density, whereas in thin films, increased thickness and improved layer uniformity contribute significantly to emission intensity. This demonstrates the critical role of both chemical composition and physical form on optical properties.

Overall, this research establishes clear links between synthesis conditions, structural and morphological quality, and luminescent performance. ZnO: Eu and ZnO: Eu,Li materials show tunable optical features, making them promising options for optoelectronic and photonic applications, such as red-emitting phosphors in LEDs, luminescent detectors, and other devices that require controlled emission.

References introduction general

[1] W. Zermane *et al.*, 'Effect of Li^{+} co-doping on structural, morphological and photoluminescence spectroscopy of ZnO: Eu^{3+} nanocrystal powders', *Ceram. Int.*, 2025, Accessed: Jun. 21, 2025. [Online]. Available: https://www.sciencedirect.com/science/article/pii/S0272884225009162

[2] W. Ouyang, J. Chen, Z. Shi, and X. Fang, 'Self-powered UV photodetectors based on ZnO nanomaterials', *Appl. Phys. Rev.*, vol. 8, no. 3, 2021, Accessed: Jun. 21, 2025. [Online]. Available: https://pubs.aip.org/aip/apr/article/8/3/031315/124788

[3] A. Tahir, M. A. Bujran, M. S. Soherverdy, and B. Want, 'Synthesis and optimization of Eu^{3+}: ZnO and pristine ZnO based thin film through sol-gel technique for an improved visible light photodetection', *Mater. Sci. Eng. B*, vol. 308, p. 117585, 2024.

[4] M. Banari, N. Memarian, P. Kumar, S. You, A. Vomiero, and I. Concina, 'CeO_2: ZnO hybrid nanorods for self-powered UV-photodetectors', *Ceram. Int.*, vol. 51, no. 1, pp. 9–16, 2025.

[5] K. Liu, M. Sakurai, and M. Aono, 'ZnO-based ultraviolet photodetectors', *Sensors*, vol. 10, no. 9, pp. 8604–8634, 2010.

[6] Y. Larbah, M. Adnane, and T. Sahraoui, 'Effect of substrate temperature on structural and optical properties of spray deposited ZnO thin films', *Mater. Sci.-Pol.*, vol. 33, no. 3, pp. 491–496, Sep. 2015, doi: 10.1515/msp-2015-0062.

[7] C. Xia, T. Zhao, R. Ji, D. Yang, and X. Ma, 'Electroluminescence from silicon-based light-emitting devices with erbium-doped ZnO films: enhancement effect of lithium codoping', *J. Mater. Sci. Mater. Electron.*, vol. 36, no. 5, p. 342, Feb. 2025, doi: 10.1007/s10854-025-14427-5.

[8] J. Deenadayalan, S.-S. Chen, B. Das, and M. Pasawan, 'Mineralization and toxicity reduction of chlortetracycline using an environmentally friendly ZnO photocatalyst prepared from Camellia sinensis leaf extract', *J. Environ. Chem. Eng.*, vol. 13, no. 1, p. 115345, 2025.

[9] Ü. Özgür *et al.*, 'A comprehensive review of ZnO materials and devices', *J. Appl. Phys.*, vol. 98, no. 4, 2005, Accessed: Jun. 21, 2025. [Online]. Available: https://pubs.aip.org/aip/jap/article/98/4/041301/151856

[10] B. Rahal *et al.*, 'Sol-gel synthesis and nanostructured semiconductor analysis of undoped and Cd-doped ZnO thin films', *Optik*, vol. 169, pp. 303–313, 2018.

[11] W. Bekhti, M. Ghamnia, and L. Guerbous, 'Effect of some amines, dodecylamine (DDA) and hexadecyldimethylamine (DMHA), on the formation of ZnO nanorods

synthesized by hydrothermal route', *Philos. Mag.*, vol. 94, no. 25, pp. 2886–2899, Sep. 2014, doi: 10.1080/14786435.2014.937785.

[12] Y. Terai, K. Yamaoka, K. Yoshida, T. Tsuji, and Y. Fujiwara, 'Photoluminescence properties of Eu-doped ZnO films grown by sputtering-assisted metalorganic chemical vapor deposition', *Phys. E Low-Dimens. Syst. Nanostructures*, vol. 42, no. 10, pp. 2834–2836, 2010.

[13] D. K. Sharma, S. Shukla, K. K. Sharma, and V. Kumar, 'A review on ZnO: Fundamental properties and applications', *Mater. Today Proc.*, vol. 49, pp. 3028–3035, 2022, doi: 10.1016/j.matpr.2020.10.238.

[14] W.-L. Wei *et al.*, 'Structural and optical properties of Eu-doped ZnO epitaxial thin films grown by pulsed-laser deposition', *APL Mater.*, vol. 12, no. 11, 2024, Accessed: Jun. 21, 2025. [Online]. Available: https://pubs.aip.org/aip/apm/article/12/11/111112/3320647

[15] T. T. T. Huong *et al.*, 'Eu^{3+} -doped ZnO quantum dots: structure, vibration characteristics, optical properties, and energy transfer process', *Nanoscale Adv.*, vol. 7, no. 3, pp. 909–921, 2025, doi: 10.1039/D4NA00858H.

[16] T. Ivanova, A. Harizanova, T. Koutzarova, B. Vertruyen, and R. Closset, 'Sol–Gel Synthesis of ZnO: Li Thin Films: Impact of Annealing on Structural and Optical Properties', *Crystals*, vol. 14, no. 1, p. 6, 2023.

References chapiter I

[1] C. F. Klingshirn, A. Waag, A. Hoffmann, and J. Geurts, *Zinc Oxide: From Fundamental Properties Towards Novel Applications*. Springer Science & Business Media, 2010.

[2] S. Nandi, S. Kumar, and A. Misra, 'Zinc oxide heterostructures: Advances in devices from self-powered photodetectors to self-charging supercapacitors', *Mater. Adv.*, vol. 2, no. 21, pp. 6768–6799, 2021.

[3] Larbah, Y. (2011). Elaboration et caractérisation des couches minces conductrices et transparentes pour les cellules solaires de type TCO/ZnS/CIS. *Mémoire Magister, Univ. USTO, Oran*.

[4] A. N. Baranov *et al.*, 'Nanocrystallinity as a Route to Metastable Phases: Rock Salt ZnO', *Chem. Mater.*, vol. 25, no. 9, pp. 1775–1782, May 2013, doi: 10.1021/cm400293j.

[5] Z. Xin-Yu *et al.*, 'Ab initio comparative study of zincblende and wurtzite ZnO', *Chin. Phys. Lett.*, vol. 24, no. 4, p. 1032, 2007.

[6] H. Morkoç and Ü. Özgür, *Zinc oxide: fundamentals, materials and device technology*. John Wiley & Sons, 2008. Accessed: Jun. 25, 2025.

[7] D. G. Thomas, 'The exciton spectrum of zinc oxide', *J. Phys. Chem. Solids*, vol. 15, no. 1–2, pp. 86–96, 1960.

[8] S. Repp and E. Erdem, 'Controlling the exciton energy of zinc oxide (ZnO) quantum dots by changing the confinement conditions', *Spectrochim. Acta. A. Mol. Biomol. Spectrosc.*, vol. 152, pp. 637–644, 2016.

[9] T. H. Flemban, 'High quality zinc oxide thin films and nanostructures prepared by pulsed laser deposition for photodetectors', 2017, Accessed: Jun. 28, 2025. [Online]. Available: https://repository.kaust.edu.sa/handle/10754/626351

[10] 'Strain effects on band structure of wurtzite ZnO: a GGA + U study', *J. Semicond.*, vol. 35, no. 7, p. 073004, Jul. 2014, doi: 10.1088/1674-4926/35/7/073004.

[11] H. Y. H. Yoshikawa and S. A. S. Adachi, 'Optical constants of ZnO', *Jpn. J. Appl. Phys.*, vol. 36, no. 10R, p. 6237, 1997.

[12] A. Galdámez-Martinez, G. Santana, F. Güell, P. R. Martínez-Alanis, and A. Dutt, 'Photoluminescence of ZnO nanowires: a review', *Nanomaterials*, vol. 10, no. 5, p. 857, 2020.

[13] D. C. Look, 'Recent advances in ZnO materials and devices', *Mater. Sci. Eng. B*, vol. 80, no. 1–3, pp. 383–387, 2001.

[14] Z. L. Wang and J. Song, 'Piezoelectric Nanogenerators Based on Zinc Oxide Nanowire Arrays', *Science*, vol. 312, no. 5771, pp. 242–246, Apr. 2006, doi: 10.1126/science.1124005.

[15] Z. L. Wang, 'Zinc oxide nanostructures: growth, properties and applications', *J. Phys. Condens. Matter*, vol. 16, no. 25, p. R829, 2004.

[16] Ü. Özgür *et al.*, 'A comprehensive review of ZnO materials and devices', *J. Appl. Phys.*, vol. 98, no. 4, 2005, Accessed: Jun. 28, 2025. [Online]. Available: https://pubs.aip.org/aip/jap/article/98/4/041301/151856

[17] S. B. Zhang, 'Microscopic origin of the phenomenological doping limit rule in semiconductors', in *APS March Meeting Abstracts*, 2001, pp. C5-002. Accessed: Jun. 28, 2025. [Online]. Available: https://ui.adsabs.harvard.edu/abs/2001APS..MAR.C5002Z/abstract

[18] A. Janotti and C. G. Van de Walle, 'Fundamentals of zinc oxide as a semiconductor', *Rep. Prog. Phys.*, vol. 72, no. 12, p. 126501, 2009.

[19] C. Klingshirn, 'ZnO: From basics towards applications', *Phys. Status Solidi B*, vol. 244, no. 9, pp. 3027–3073, Sep. 2007, doi: 10.1002/pssb.200743072.

[20] A. S. H. Hameed, C. Karthikeyan, S. Sasikumar, V. S. Kumar, S. Kumaresan, and G. Ravi, 'Impact of alkaline metal ions Mg^{2+}, Ca^{2+}, Sr^{2+} and Ba^{2+} on the structural, optical, thermal and antibacterial properties of ZnO nanoparticles prepared by the co-precipitation method', *J. Mater. Chem. B*, vol. 1, no. 43, pp. 5950–5962, 2013.

[21] C. Rauch *et al.*, 'Lithium related deep and shallow acceptors in Li-doped ZnO nanocrystals', *J. Appl. Phys.*, vol. 107, no. 2, 2010, Accessed: Jun. 28, 2025. [Online]. Available: https://pubs.aip.org/aip/jap/article/107/2/024311/399530

[22] M. Khuili, N. Fazouan, H. A. El Makarim, G. El Halani, and E. H. Atmani, 'Comparative first principles study of ZnO doped with group III elements', *J. Alloys Compd.*, vol. 688, pp. 368–375, Dec. 2016, doi: 10.1016/j.jallcom.2016.06.294.

[23] S. J. Pearton *et al.*, 'Advances in wide bandgap materials for semiconductor spintronics', *Mater. Sci. Eng. R Rep.*, vol. 40, no. 4, pp. 137–168, 2003.

[24] A. Layek, S. Banerjee, B. Manna, and A. Chowdhury, 'Synthesis of rare-earth doped ZnO nanorods and their defect–dopant correlated enhanced visible-orange luminescence', *RSC Adv.*, vol. 6, no. 42, pp. 35892–35900, Apr. 2016, doi: 10.1039/C6RA02278B.

[25] M. Baira, A. Bekhti-Siad, K. Hebali, H. Bouhani-Benziane, and M. Sahnoun, 'Charge compensation mechanisms in favor of the incorporation of the Eu^{3+} ion into the ZnO host lattice', *Phys. B Condens. Matter*, vol. 537, pp. 296–300, 2018.

[26] R. C. Ropp, *Encyclopedia of the alkaline earth compounds*. Newnes, 2012. Accessed: Jun. 29, 2025. [Online]. Available: https://books.google.com/books?hl=fr&lr=&id=yZ786vEild0C&oi=fnd&pg=PP1&dq=Ropp,+R.+C.+(2013).&ots=WwF2cDTDZ1&sig=e4TPVzvRkiLWIFagzBLP4MPLKNM

[27] X. Yuan, H. Yu, Z. Chen, and Q. Wei, 'Preparation and luminescent properties of rare earth Eu-doped nano-ZnO composite films on textiles', *J. Ind. Text.*, vol. 54, p. 15280837241306350, Jan. 2024, doi: 10.1177/15280837241306350.

[28] N. Zhang, C. Guo, J. Zheng, X. Su, and J. Zhao, 'Synthesis, electronic structures and luminescent properties of Eu^{3+} doped $KGdTiO_4$', *J. Mater. Chem. C*, vol. 2, no. 20, pp. 3988–3994, 2014.

[29] S. Shionoya, W. M. Yen, and H. Yamamoto, *Phosphor handbook*. CRC press, 2018. Accessed: Jul. 02, 2025.

[30] S. V. Eliseeva and J.-C. G. Bünzli, 'Lanthanide luminescence for functional materials and bio-sciences', *Chem. Soc. Rev.*, vol. 39, no. 1, pp. 189–227, 2010, doi: 10.1039/B905604C.

[31] S. Stojadinović and A. Ćirić, 'Photoluminescence of ZnO: Eu^{3+} and ZnO: Tb^{3+} coatings formed by plasma electrolytic oxidation of pure zinc substrate', *J. Lumin.*, vol. 235, p. 118022, 2021.

[32] J. Kaszewski *et al.*, 'Tuning the luminescence of ZnO: Eu nanoparticles for applications in biology and medicine', *Opt. Mater.*, vol. 80, pp. 77–86, 2018.

[33] C. Görller-Walrand and K. Binnemans, 'Chapter 167 Spectral intensities of f-f transitions', in *Handbook on the Physics and Chemistry of Rare Earths*, vol. 25, Elsevier, 1998, pp. 101–264. doi: 10.1016/S0168-1273(98)25006-9.

[34] I. Choudhary, R. Shukla, A. Sharma, and K. K. Raina, 'Effect of excitation wavelength and europium doping on the optical properties of nanoscale zinc oxide', *J. Mater. Sci. Mater. Electron.*, vol. 31, no. 22, pp. 20033–20042, Nov. 2020, doi: 10.1007/s10854-020-04525-x.

[35] M. E. Jouad, E. M. Bouabdalli, S. Touhtouh, M. Addou, N. Ollier, and B. Sahraoui, 'Red luminescence and UV light generation of europium doped zinc oxide thin films for optoelectronic applications', *Eur. Phys. J. Appl. Phys.*, vol. 91, no. 1, Art. no. 1, Jul. 2020, doi: 10.1051/epjap/2020200133.

References chapiter II

[1] J. Vasudevan, S. Johnson Jeyakumar, B. Arunkumar, M. Jothibas, A. Muthuvel, and S. Vijayalakshmi, 'Optical and magnetic investigation of Cu doped ZnO nanoparticles synthesized by solid state method', *Materials Today: Proceedings*, vol. 48, pp. 438–442, Jan. 2022, doi: 10.1016/j.matpr.2020.12.429.

[2] S. Yuvaraj, A. C. Fernandez, M. Sundararajan, C. S. Dash, and P. Sakthivel, 'Hydrothermal synthesis of ZnO–CdS nanocomposites: Structural, optical and electrical behavior', *Ceramics International*, vol. 46, no. 1, pp. 391–402, Jan. 2020, doi: 10.1016/j.ceramint.2019.08.274.

[3] V. Parthasaradi, M. Kavitha, A. Sridevi, and J. J. Rubia, 'Novel rare-earth Eu and La co-doped ZnO nanoparticles synthesized via co-precipitation method: optical, electrical, and magnetic properties', *J Mater Sci: Mater Electron*, vol. 33, no. 34, pp. 25805–25819, Dec. 2022, doi: 10.1007/s10854-022-09272-9.

[4] F. Hussain *et al.*, 'Enhancement in combustion, performance, and emission characteristics of a diesel engine fueled with Ce-ZnO nanoparticle additive added to soybean biodiesel blends', *Energies*, vol. 13, no. 17, p. 4578, 2020.

[5] A. N. Ech-Chergui *et al.*, 'Spray pyrolysis-assisted fabrication of Eu-doped ZnO thin films for antibacterial activities under visible light irradiation', *Chem. Pap.*, vol. 77, no. 2, pp. 1047–1058, Feb. 2023, doi: 10.1007/s11696-022-02543-z.

[6] Larbah Youssef (2017). L'optimisation des couches minces TCO : SnO_2, ZnO et TiO_2 par la méthode spray pyrolyse en vue de la formation des jonctions photovoltaïques sur le silicium de type « n ». Thèse, Univ. USTO, Oran

[7] M. N. Murthy, M. G. Krishna, and G. Chandrakala, 'Self-protective Antibacterial and Hydrophobic ZnO Thin Film Coatings', *Indian Journal of Pure & Applied Physics (IJPAP)*, vol. 63, no. 1, pp. 82–88, 2025.

[8] A. Kumawat, S. Chattopadhyay, K. P. Misra, R. D. K. Misra, and P. Kumari, 'Micro-strain governed photoluminescence emission intensity of sol-gel spin coated Eu doped ZnO thin films', *Thin Solid Films*, vol. 761, p. 139521, 2022.

[9] P. Innocenzi, *The Sol-to-Gel Transition*. in SpringerBriefs in Materials. Cham: Springer International Publishing, 2019. doi: 10.1007/978-3-030-20030-5.

[10] S. Sakka, *Handbook of sol-gel science and technology. 1. Sol-gel processing*, vol. 1. Springer Science & Business Media, 2005. Accessed: Jul. 15, 2025.

[11] C. J. Brinker and G. W. Scherer, *Sol-Gel Science: The Physics and Chemistry of Sol-Gel Processing*. Academic Press, 2013.

[12] D. Frederichi, M. H. N. O. Scaliante, and R. Bergamasco, 'Structured photocatalytic systems: photocatalytic coatings on low-cost structures for treatment of water contaminated with micropollutants—a short review', *Environ Sci Pollut Res*, vol. 28, no. 19, pp. 23610–23633, May 2021, doi: 10.1007/s11356-020-10022-9.

References chapiter III

[1] K. Liu *et al.*, 'Influence of Eu_2O_3 on microstructure and electrical properties of ZnO-Pr_6O_{11} based varistors', *Ceramics International*, vol. 50, no. 2, pp. 3990–3996, 2024.

[2] L. Armelao *et al.*, 'Structure−Luminescence Correlations in Europium-Doped Sol−Gel ZnO Nanopowders', *J. Phys. Chem. C*, vol. 112, no. 11, pp. 4049–4054, Mar. 2008, doi: 10.1021/jp710207r.

[3] Q. Shi *et al.*, 'Enhancing blue luminescence from Ce-doped ZnO nanophosphor by Li doping', *Nanoscale Res Lett*, vol. 9, no. 1, p. 480, Dec. 2014, doi: 10.1186/1556-276X-9-480.

[4] U. Seetawan *et al.*, 'Effect of calcinations temperature on crystallography and nanoparticles in ZnO disk', *Materials Sciences and Applications*, vol. 2, no. 9, pp. 1302–1306, 2011.

[5] K. Badreddine, I. Kazah, M. Rekaby, and R. Awad, 'Structural, Morphological, Optical, and Room Temperature Magnetic Characterization on Pure and Sm-Doped ZnO Nanoparticles', *Journal of Nanomaterials*, vol. 2018, pp. 1–11, Jul. 2018, doi: 10.1155/2018/7096195.

[6] R. Yogamalar, R. Srinivasan, A. Vinu, K. Ariga, and A. C. Bose, 'X-ray peak broadening analysis in ZnO nanoparticles', *Solid State Communications*, vol. 149, no. 43–44, pp. 1919–1923, 2009.

[7] D. Balzar and H. Ledbetter, 'Voigt-function modeling in Fourier analysis of size-and strain-broadened X-ray diffraction peaks', *Applied Crystallography*, vol. 26, no. 1, pp. 97–103, 1993.

[8] F. I. H. Rhouma *et al.*, 'The structure and photoluminescence of a ZnO phosphor synthesized by the sol gel method under praseodymium doping', *RSC advances*, vol. 9, no. 9, pp. 5206–5217, 2019.

[9] P. Bindu and S. Thomas, 'Estimation of lattice strain in ZnO nanoparticles: X-ray peak profile analysis', *J Theor Appl Phys*, vol. 8, no. 4, pp. 123–134, Dec. 2014, doi: 10.1007/s40094-014-0141-9.

[10] R. Cuscó *et al.*, 'Temperature dependence of Raman scattering in ZnO', *Phys. Rev. B*, vol. 75, no. 16, p. 165202, Apr. 2007, doi: 10.1103/PhysRevB.75.165202.

[11] S. Monticone, R. Tufeu, and A. V. Kanaev, 'Complex Nature of the UV and Visible Fluorescence of Colloidal ZnO Nanoparticles', *J. Phys. Chem. B*, vol. 102, no. 16, pp. 2854–2862, Apr. 1998, doi: 10.1021/jp973425p.

[12] M. Baira, A. Bekhti-Siad, K. Hebali, H. Bouhani-Benziane, and M. Sahnoun, 'Charge compensation mechanisms in favor of the incorporation of the Eu3+ ion into the ZnO host lattice', *Physica B: Condensed Matter*, vol. 537, pp. 296–300, 2018.

[13] H. D. Lutz, C. Jung, R. Mörtel, H. Jacobs, and R. Stahl, 'Hydrogen bonding in solid hydroxides with strongly polarising metal ions, β-Be $(OH)_2$ and ε-Zn $(OH)_2$', *Spectrochimica Acta Part A: Molecular and Biomolecular Spectroscopy*, vol. 54, no. 7, pp. 893–901, 1998.

[14] P. P. Pal and J. Manam, 'Structural and photoluminescence studies of Eu^{3+} doped zinc oxide nanorods prepared by precipitation method', *Journal of Rare Earths*, vol. 31, no. 1, pp. 37–43, 2013.

[15] S. Stojadinović and A. Ćirić, 'Photoluminescence of ZnO: Eu^{3+} and ZnO: Tb^{3+} coatings formed by plasma electrolytic oxidation of pure zinc substrate', *Journal of Luminescence*, vol. 235, p. 118022, 2021.

[16] E. H. H. Hasabeldaim, O. M. Ntwaeaborwa, R. E. Kroon, E. Coetsee, and H. C. Swart, 'Photoluminescence and cathodoluminescence of spin coated ZnO films with different concentration of Eu^{3+} ions', *Vacuum*, vol. 169, p. 108889, 2019.

[17] E. H. H. Hasabeldaim, H. C. Swart, and R. E. Kroon, 'Web-based application software for Judd-Ofelt analysis of Eu^{3+} ion luminescence', *Results in Optics*, vol. 16, p. 100688, 2024.

[18] O. M. Ntwaeaborwa, S. J. Mofokeng, V. Kumar, and R. E. Kroon, 'Structural, optical and photoluminescence properties of Eu^{3+} doped ZnO nanoparticles', *Spectrochimica Acta Part A: Molecular and Biomolecular Spectroscopy*, vol. 182, pp. 42–49, 2017.

[19] S. Bayan and D. Mohanta, 'Directed growth characteristics and optoelectronic properties of Eu-doped ZnO nanorods and urchins', *Journal of Applied Physics*, vol. 108, no. 2, 2010, Accessed: Aug. 14, 2025. [Online]. Available: https://pubs.aip.org/aip/jap/article/108/2/023512/946165

[20] A. Mahesh, I. N. Jawahar, and V. Biju, 'Photoluminescence, photocurrent response and photocatalytic activity of hydrothermally derived nanocrystalline ZnO with native point defects', *Journal of Crystal Growth*, vol. 648, p. 127894, 2024.

[21] G. Blasse and B. C. Grabmaier, 'A General Introduction to Luminescent Materials', in *Luminescent Materials*, G. Blasse and B. C. Grabmaier, Eds., Berlin, Heidelberg: Springer, 1994, pp. 1–9. doi: 10.1007/978-3-642-79017-1_1.

[22] N. Jain *et al.*, 'Synthesis and rational design of europium and lithium doped sodium zinc molybdate with red emission for optical imaging', *Scientific reports*, vol. 9, no. 1, p. 2472, 2019.

[23] P. Chen, X. Ma, and D. Yang, 'ZnO: Eu thin-films: Sol–gel derivation and strong photoluminescence from $^5D_0 \rightarrow {}^7F_0$ transition of Eu^{3+} ions', *Journal of alloys and compounds*, vol. 431, no. 1–2, pp. 317–320, 2007.

[24] A. K. Parchur and R. S. Ningthoujam, 'Behaviour of electric and magnetic dipole transitions of Eu^{3+}, $^5D_0 \rightarrow {}^7F_0$ and Eu–O charge transfer band in Li^+ co-doped YPO_4: Eu^{3+}', *RSC advances*, vol. 2, no. 29, pp. 10859–10868, 2012.

[25] A. M. Srivastava, M. G. Brik, W. W. Beers, and W. Cohen, 'The influence of nd0 transition metal cations on the Eu^{3+} asymmetry ratio R= I ($^5D_0$- ^{7}F2) I ($^5D_0$- $^7F_1$) and crystal field splitting of $^7F_1$ manifold in pyrochlore and zircon compounds', *Optical Materials*, vol. 114, p. 110931, 2021.

[26] R. Raji, R. G. A. Kumar, and K. G. Gopchandran, 'Influence of local structure on luminescence dynamics of red emitting ZnO:Eu^{3+} nanostructures and its Judd-Ofelt analysis', *Journal of Luminescence*, vol. 205, pp. 179–189, Jan. 2019, doi: 10.1016/j.jlumin.2018.09.002.

[27] S. Stojadinović and A. Ćirić, 'Photoluminescence of ZnO:Eu^{3+} and ZnO:Tb^{3+} coatings formed by plasma electrolytic oxidation of pure zinc substrate', *Journal of Luminescence*, vol. 235, p. 118022, Jul. 2021, doi: 10.1016/j.jlumin.2021.118022.

[28] T.-H. Fang *et al.*, 'Photoluminescence characteristics of ZnO doped with Eu^{3+} powders', *Journal of Physics and Chemistry of Solids*, vol. 70, no. 6, pp. 1015–1018, 2009.

[29] A. Ćirić, S. Stojadinović, M. G. Brik, and M. D. Dramićanin, 'Judd-Ofelt parametrization from emission spectra: The case study of the Eu^{3+} $^5D_1$ emitting level', *Chemical Physics*, vol. 528, p. 110513, 2020.

[30] W. T. Carnall, P. R. Fields, and K. Rajnak, 'Electronic energy levels of the trivalent lanthanide aquo ions. IV. Eu3+', *The Journal of Chemical Physics*, vol. 49, no. 10, pp. 4450–4455, 1968.

[31] N. Raskar, D. Dake, H. Khawal, U. Deshpande, K. Asokan, and B. Dole, 'Development of oxygen vacancies and surface defects in Mn-doped ZnO nanoflowers for enhancing visible light photocatalytic activity', *SN Appl. Sci.*, vol. 2, no. 8, p. 1403, Aug. 2020, doi: 10.1007/s42452-020-3053-0.

[32] A. V. Egorysheva, V. D. Volodin, A. A. Chistyakov, Yu. A. Kuzishchin, V. M. Skorikov, and T. D. Dudkina, 'Luminescence of europium-doped BaO-Bi_2O_3-B_2O_3 glasses', *Inorg Mater*, vol. 46, no. 12, pp. 1384–1390, Dec. 2010, doi: 10.1134/S0020168510120204.

[33] S. A. Saleem, B. C. Jamalaiah, A. M. Babu, K. Pavani, and L. R. Moorthy, 'A study on fluorescence properties of Eu^{3+} ions in alkali lead tellurofluoroborate glasses', *Journal of Rare Earths*, vol. 28, no. 2, pp. 189–193, 2010.

[34] D. Prakashbabu *et al.*, 'Charge compensation assisted enhancement of photoluminescence in combustion derived Li^+ co-doped cubic ZrO_2: Eu^{3+} nanophosphors', *Physical Chemistry Chemical Physics*, vol. 18, no. 42, pp. 29447–29457, 2016.

[35] D. Toptygin, 'Effects of the Solvent Refractive Index and Its Dispersion on the Radiative Decay Rate and Extinction Coefficient of a Fluorescent Solute'.

[36] C.-K. Duan and M. F. Reid, 'Local field effects on the radiative lifetimes of Ce^{3+} in different hosts', *Current Applied Physics*, vol. 6, no. 3, pp. 348–350, Jun. 2006, doi: 10.1016/j.cap.2005.11.016.

[37] R. S. Meltzer, S. P. Feofilov, B. Tissue, and H. B. Yuan, 'Dependence of fluorescence lifetimes of Y 2 O 3 : E u^{3+} nanoparticles on the surrounding medium', *Phys. Rev. B*, vol. 60, no. 20, pp. R14012–R14015, Nov. 1999, doi: 10.1103/PhysRevB.60.R14012.

[38] G. M. Kumar, D. N. Rao, and G. S. Agarwal, 'Experimental studies of spontaneous emission from dopants in an absorbing dielectric', *Optics letters*, vol. 30, no. 7, pp. 732–734, 2005.

[39] K. Dolgaleva, R. W. Boyd, and P. W. Milonni, 'Influence of local-field effects on the radiative lifetime of liquid suspensions of Nd: YAG nanoparticles', *Journal of the Optical Society of America B*, vol. 24, no. 3, pp. 516–521, 2007.

[40] D. Toptygin, 'Effects of the Solvent Refractive Index and Its Dispersion on the Radiative Decay Rate and Extinction Coefficient of a Fluorescent Solute', *Journal of Fluorescence*, vol. 13, no. 3, pp. 201–219, May 2003, doi: 10.1023/A:1025033731377.

[41] A. Piquette, W. Bergbauer, B. Galler, and K. C. Mishra, 'On choosing phosphors for near-UV and blue LEDs for white light', *ECS Journal of Solid State Science and Technology*, vol. 5, no. 1, p. R3146, 2015.

[42] J. Jou *et al.*, 'OLEDs with Candle-Like Emission', *Information Display*, vol. 31, no. 6, pp. 23–27, Nov. 2015, doi: 10.1002/j.2637-496X.2015.tb00857.x.

[43] D. Brown, 'Investigation of the spectral properties of LED-based MR16 bulbs for general illumination', *Opt. Eng*, vol. 44, no. 11, p. 111310, Nov. 2005, doi: 10.1117/1.2130314.

References chapiter IV

[1] Ji, J., Colosimo, A. M., Anwand, W., Boatner, L. A., Wagner, A., Stepanov, P. S., ... & Selim, F. A. (2016). ZnO Luminescence and scintillation studied via photoexcitation, X-ray excitation and gamma-induced positron spectroscopy. Scientific reports, 6(1), 31238.

[2] Larbah, Y., Adnane, M., & Sahraoui, T. (2015). Effect of substrate temperature on structural and optical properties of spray deposited ZnO thin films. Materials Science Poland, 33(3), 491-496.

[3] Chen, J., Yang, X., Ning, Y., Yang, X., Huang, Y., Zhang, Z., ... & Li, Q. (2024). Preparation and application of nanostructured ZnO in radiation detection. Materials, 17(14), 3549.

[4] Bouacheria, M. A., Djelloul, A., Adnane, M., Larbah, Y., & Benharrat, L. (2022). Characterization of pure and Al doped ZnO thin films prepared by sol gel method for solar cell applications. Journal of Inorganic and Organometallic Polymers and Materials, 32(7), 2737-2747.

[5] Larbah, Y. (2011). Elaboration et caractérisation des couches minces conductrices et transparentes pour les cellules solaire de type TCO/ZnS/CIS. Mémoire Magister, Univ. USTO, Oran.

[6]Gorokhova, E. I., Anan'Eva, G. V., Demidenko, V. A., Rodnyĭ, P. A., Khodyuk, I. V., & Bourret-Courchesne, E. D. (2008). Optical, luminescence, and scintillation properties of ZnO and ZnO: Ga ceramics. Journal of Optical Technology, 75(11), 741-746.

[7]Kunikata, T., Kato, T., Shiratori, D., Nakauchi, D., Kawaguchi, N., & Yanagida, T. (2022). Scintillation Properties of Li-doped ZnO Translucent Ceramic. Sensors & Materials, 34.

[8]Chen, X., Xie, Q., & Li, J. (2020). Significantly improved photoluminescence properties of ZnO thin films by lithium doping. Ceramics International, 46(2), 2309-2316.

[9] Krishna, R., Haranath, D., Singh, S. P., Chander, H., Pandey, A. C., & Kanjilal, D. (2007). Synthesis and improved photoluminescence of Eu: ZnO phosphor. Journal of materials science, 42(24), 10047-10051.

[10] Pavón, F., Urbieta, A., & Fernández, P. (2022). Characterization, luminescence and optical resonant modes of Eu-Li Co-doped ZnO nano-and microstructures. Applied Sciences, 12(14), 6948.

[11] Armelao, L., Heigl, F., Jürgensen, A., Blyth, R. I. R., Regier, T., Zhou, X. T., & Sham, T. K. (2007). X-ray excited optical luminescence studies of ZnO and Eu-doped ZnO nanostructures. The Journal of Physical Chemistry C, 111(28), 10194-10200.

[12] Zhong, M., Shan, G., Li, Y., Wang, G., & Liu, Y. (2007). Synthesis and luminescence properties of Eu^{3+} doped ZnO nanocrystals by a hydrothermal process. Materials Chemistry and Physics, 106(2-3), 305-309.

[13] Pal, P. P., & Manam, J. (2014). Enhanced luminescence of ZnO: RE^{3+} (RE= Eu, Tb) nanorods by Li^{+} doping and calculations of kinetic parameters. Journal of luminescence, 145, 340-350.

[14] Liu, Z., & Li, Y. (2008). Sol–gel synthesis and luminescence property of ZnO:(La, Eu) Cl nanocomposite thin films. Thin Solid Films, 516(16), 5557-5561.

[15] Pavón, F., Urbieta, A., & Fernández, P. (2022). Characterization, luminescence and optical resonant modes of Eu-Li Co-doped ZnO nano-and microstructures. Applied Sciences, 12(14), 6948.

[16] Shi, Q., Wang, C., Li, S., Wang, Q., Zhang, B., Wang, W., ... & Zhu, H. (2014). Enhancing blue luminescence from Ce-doped ZnO nanophosphor by Li doping. Nanoscale Research Letters, 9(1), 480.